The Dissertation Committee for Abhimanyu Bhat certifies that this is the approved version of the following dissertation:

ELECTROCHEMICAL INFILTRATION INTO LASER SINTERED POROUS GRAPHITE AND SILICON CARBIDE

Committee:

David Bourell, Supervisor

Desiderio Kovar

Harovel Wheat

Joseph Beaman

Maria Juenger

ELECTROCHEMICAL INFILTRATION INTO LASER SINTERED POROUS GRAPHITE AND SILICON CARBIDE

by

Abhimanyu Bhat, B.Tech, M.S.

Dissertation

Presented to the Faculty of the Graduate School of

The University of Texas at Austin

in Partial Fulfillment

of the Requirements

for the Degree of

Doctor of Philosophy

The University of Texas at Austin

May, 2015

Dedication

To my parents

Acknowledgements

Through the course of this Ph.D., I have realized that I could never have done any of this, particularly the research and writing that went into this dissertation, without the support and encouragement of a lot of people.

First and foremost I would like to thank my advisor, Dr. David L. Bourell without whom none of this work would have been possible. I could not have hoped for a better advisor to support and guide me through this Ph.D. I would also like to express my gratitude to Dr. Desiderio Kovar for all the input that have helped in this research. I would also like to thank Dr. Harovel Wheat, Dr. Maria Juenger and Dr. Joseph Beaman for their invaluable comments and suggestions.

I sincerely thank Dr. Thomas Moffat, Dr. Jeremy Meyers and Dr. John Goodenough for providing me with the right direction to pursue in the course of this work. I would like to thank Dr. Allan Bard for allowing me to use facilities at the Center for Electrochemistry and also for invaluable discussions. I would also like to thank Netz Arroyo and Brent Bennet for training me on these facilities. I would like to thank Mark Phillips, Fred Rotthauser, Rosalie Foster and all the other staff members who, in the course of my research, have provided incredible assistance and spent hours helping me with my work.

I gratefully acknowledge the funding sources that made my Ph.D. work possible. My work was supported by the NSF under grant no. CMMI-0926316. I would like to express my thanks to everyone involved with the experimentation process, especially Dr. David Sing and Dr. Vikram Deverajan for all the hours spent on designing the experiments. I would also like to express my thanks Dr. Li Shi, Dr. Xi Chen and Dr.

Mourad Krifa for providing thermal conductivity measurement facilities for performing measurements on my samples. The work on tribological properties presented here was accomplished at the Washington State University by Dr. Amit Bandyopadyay and Himanshu Shehastrabuddhe. I would also like to thank Dr. Micheal Bryant for helping design the same.

I would also like to acknowledge my group members Maggie Yuan, Kaushik Alayavalli, Kumaran Chakravarthy and Phani Vallabhajosyula for all the stimulating conversations. I sincerely thank Dr. Preetam Singh for being a great mentor, sounding board and for helping me carryout electrochemical characterization experiments such as EIS in Dr. Goodenough's research group. This work would not have been possible without the moral support of my friends Tushar Sharma, Akshay Singh and Nishant Verma. I would also like to thank Parimal Saraf and Ankur Kanthwal for being there to listen to my problems and for providing a calm influence when things weren't going right for me. I hope they are both doing good in their respective spheres of life. I would especially like to thank Bethany Hamilton who took care of everything else while I was writing my dissertation.

Finally, I dedicate this work to my parents whose undying love and support has helped me achieve everything in my life. I would especially like to thank them for taking care of me and creating an environment where I could share everything in my life with them. I would also like to thank them for the countless occasions where they motivated me to not be afraid of failure.

ELECTROCHEMICAL INFILTRATION INTO LASER SINTERED POROUS GRAPHITE AND SILICON CARBIDE

Abhimanyu Bhat, Ph.D.

The University of Texas at Austin, 2015

Supervisor: David Bourell

Indirect laser sintering is a technique used for direct manufacturing of high melting materials such as graphite and silicon carbide. This technique produces parts with high pore volume fraction and poor structural stability. Such parts are post processed using melt infiltration techniques with metals or alloys such as copper and brass. These processes require high temperature and are not environmentally sustainable and may also encounter restrictions because of infiltration atmosphere. Electrodeposition of a metal into the porous parts produced via laser sintering is an alternate route for filling these parts. Such a route required infiltration of the porous parts with a suitable electrolyte and subsequent electrodeposition of the metal ions into the pore network. Electrodeposition provides a versatile and convenient route to the realization of bulk structures and coatings of metal matrix composites.

In the present study, electrodeposition of copper into the pore network of laser sintered graphite and silicon carbide was studied. A theoretical model based on Butler-Volmer equation was made to predict electrodeposition rates across the porous preforms by simulating the current density distribution across the porous part in an electrodeposition cell. The theoretical model was used to determine most favorable

conditions required to complete electrolytic infiltration. Electrolytic infiltration of copper was carried out into laser sintered graphite and silicon carbide parts and commercially available porous preforms such as Nomex felt, graphite felt and a stainless steel mesh, using flow electrolysis methods.

This study shows that electrochemical deposition of metals in the pore network of a highly porous material is possible under certain conditions. It was realized that the most favorable conditions for electrolytic infiltration exist when the porous preform being infiltrated is thin, and is a poor conductor of electricity. Hence, it is possible to fabricate highly dense metal matrix composite coatings via electrochemical infiltration. In this study Nomex fibers, Stainless Steel 316 mesh, graphite and silicon carbide were used to reinforce electrodeposited copper coatings on copper-110 alloy, and their thermal and tribological properties were measured.

Table of Contents

List of Tables

List of Figures

Chapter 1: Introduction

1.1. Selective laser sintering®

Additive manufacturing processes are a robust collection of freeformed part techniques that can build service parts with a myriad of desirable microstructures and properties [1, 2]. Selective laser sintering® (SLS®) is one of the several powder-based layer-additive manufacturing process used to make models for design testing, patterns for investment casting and small lots of functional parts [3]. Selective laser sintering is a solid freeform fabrication process, the production of freeform solid objects directly from a computer model without part-specific tooling or human intervention [4].

A schematic of the SLS process is shown in figure 1.1. A typical SLS machine consists of two feed bins in which the powders to be processed are stored. A roller is used to add powder to a part bed in a layer by layer fashion. Powder is spread as a thin layer approximately 125 microns thick. A computer-controlled laser selectively fuses the powdered material in the part bed by scanning cross-sections generated from a 3D digital description of the part (e.g. CAD model). After each cross-section is scanned, the powder bed is lowered by one layer thickness, a new layer of material is applied on the top, and the process is repeated until the solid part represented by the CAD file is produced.

Figure 1.2 shows a surface tessellation file which is created by a CAD software to represent the solid part in the form of several planes, with each plane representing a cross-section of the solid

part. A surface tessellation file describes a given 3 dimensional object in the form of triangles using a 3 dimensional Cartesian coordinate system. A laser sintered part created using the surface tessellation file is also shown.

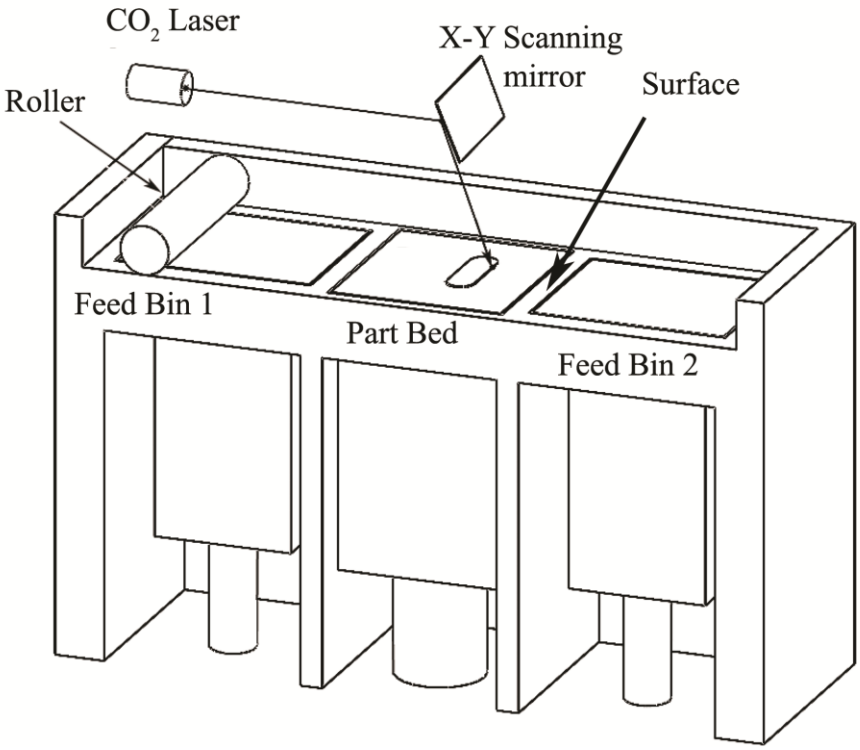

Figure 1.1: A schematic of a Selective Laser Sintering machine

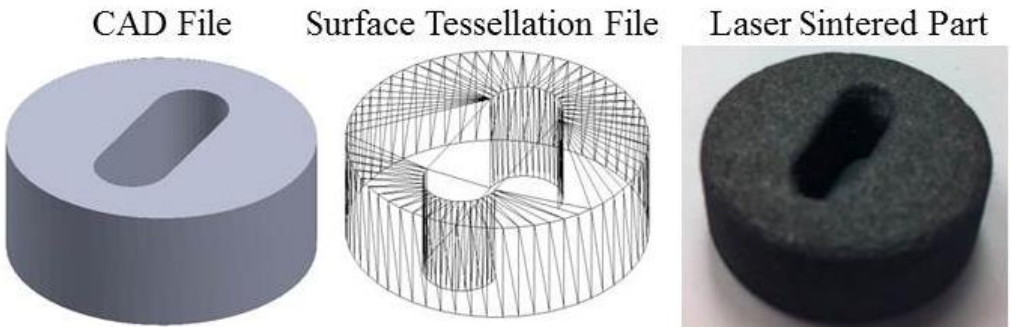

Figure 1.2: A surface tessellation file and the corresponding laser sintered part

Indirect laser sintering is particularly amenable to creation of porous nonmetallic preforms [5, 6]. The term “indirect” here refers to the use of a transient binder during part creation which is removed or transformed in a post-processing thermal treatment. One application area for these preforms is in fabrication of metal matrix composites, assuming that the continuous porosity can be filled with a suitable material, preferably a metal.

1.2. Metal matrix composite coatings

Powder metallurgy and melt infiltration are the most common techniques for producing metallic matrix composites (MMCs). There are many studies on metal/ceramic composites prepared by infiltration of molten metals into spaces of porous ceramic compact [7-16]. The aim of producing ceramic/metal composites is to achieve high fracture toughness and electrical conductivity in ceramic materials. Similarly, high strength hardness, high corrosion resistance and high hardness can be imparted to metals by the addition of ceramics. These processes require high temperature and are not environmentally sustainable. Such a process may also encounter restrictions because of infiltration atmosphere, owing to chemical reaction between metal and introduced gas which can lead to poor mechanical properties in metals [17].

The technology for producing metal matrix composites has also been extended to production of metal matrix composite coatings [18, 19]. Metal matrix composite coatings have several advantages such as better wear resistance and corrosion resistance over pure metals and alloys [20]. Various methods such as laser engineered net shaping [18], laser cladding [21], plasma spray [22, 23], cold spray [24] etc. have been used in deposition of coatings of such metal matrix composites on metallic substrates. Such coatings are used for applications where low wear rate is required along with good electrical or thermal properties [25].

1.3. Electrochemical co-deposition of composite coatings

Electrolytic co-deposition of reinforcement particles with metals has also been widely used to produce composite coatings. Electrolytic co-deposition is attractive for producing the metal matrix composite coatings because of its low cost and possibility of making large area thin films. It also allows ease of controlling the growth rate via the current density and applied potential. This method has been used to fabricate numerous composite coatings containing inert, semi-conductive and conductive particles such as Cu-graphite, Cu-Al_2O_3, Cu-SiC, Ni-PTFE, Ni-TiO_2, Ni-Al_2O_3, Ni-CdS and Ni- ZrO_2 [20, 26]. Ceramic particles with size ranging from tens of nanometers to a few micrometers have been used as reinforcements in these composite coatings. Apart from ceramic particles, polymers and hybrid particles have also been reportedly used as reinforcements in these coatings. Such metal matrix composite coatings can help in reducing wear rate of movable engineering components [27].

Electrochemical co-deposition of ceramic-reinforced composite coating on a substrate is carried out through several routes, such as physically transporting ceramic particles towards the cathode surface using convection in the electrolyte, mechanical entrapment of particles into a growing metal matrix, and by electrophoretically migrating ceramic particles to the coating surface as the electrodeposition of the metal matrix is carried out [28]. The processes involving the transportation or migration of particles towards the cathode require loading of the aqueous electrolyte with ceramic particles. Ceramic particles are dispersed uniformly in the electrolyte by use of a dispersant or surfactant or by agitating the electrolyte bath. Electrodeposition of composite coatings thus requires control of several parameters such as electrolyte conductivity, pH, agitation rate/mode, loading of particles in the electrolyte, type and amount of dispersant used, etc. All of these parameters are essential to production of good coatings [28].

1.4. Electrochemical deposition of pure metals inside porous preforms

One approach to metal filling is to use an electrolytic deposition method in which an electrolyte is infiltrated into the porous preform, followed by electrodeposition of a metallic species internally within the preform [29]. Electrodeposition provides a versatile and convenient route to the realization of controlled coatings of metal matrix composites. Electrochemical deposition is a technique that is most commonly used to deposit a thin film coating on various types of material substrates. Electrochemical methods, involving the deposition of just the metal matrix, have been used to deposit metals on and into porous materials for various applications such as producing nanowires and catalytic electrodes [30]. Hassanin and co-workers have electrodeposited nickel into porous alumina to fabricate composite coatings [31]. They used a colloidal powder processing method to prepare the porous alumina matrix. Deposition of transition metals into porous silicon and silica has also been reported in the literature [32]. Most of these studies report electrodeposition of metal into porous thin films with a thickness of the order a few nanometers to a few hundred nanometers. It was not possible to find any studies in the literature on the topic of electrolytic infiltration into porous preforms, where a functional application of the coatings was suggested.

In general, the electrodeposition of any metal into a porous material is very challenging [33, 34]. The distribution of electrodeposited metal in a porous material (or porous electrode) depends on the distribution of current density in the porous matrix. This depends on several parameters such as electrolyte and matrix conductivity, pore size, applied current and mode of mass transport. The equations developed by Newman and Tobias have been used to predict current density distributions in porous electrodes under conditions of diffusional and convective mass transport. [34]. Electrochemical reactions can be carried inside porous electrodes under conditions in which

mass transfer is carried out by flowing the electrolyte through them. Electrolyte can be flowed through the porous electrode in two ways: in a direction parallel to the applied current and in a direction perpendicular to the applied current. The former is used in recovery of metals from waste and the latter has been used in redox flow batteries [35, 36]. In systems with electrolyte flow in the same direction as applied current density, a higher local current density is found to be present at the face of the electrode due to favorable mass transfer and kinetics conditions [34, 37, 38]. You et al. and Shah et al. have used the equations developed by Newman to describe vanadium redox flow batteries in which the flow of electrolyte is perpendicular to the applied current [39, 40]. They have shown that the current density in the porous matrix is higher close to the current collector. Alkire [41] has shown mathematically and experimentally that the local current density close to the current collector is higher in a porous electrode bed when the electrolyte is flowed perpendicular to the direction of current.

This provides hope for complete filling of a porous matrix via electrolytic deposition of metal ions.

1.5. Objectives of the Current Work

The following points summarize the objectives of this work:

1) Development of a theoretical model to understand the effect of various properties of the electrolyte and porous preforms on electrochemical deposition of a metal into a porous preform.
2) To determine the effect of laser sintering processing parameters on the pore volume fraction and electrical conductivity of the porous preforms fabricated from silicon carbide and graphite powders.

3) To develop a route for electrolytic infiltration of laser sintered porous preforms by electrodepositing a metal into the pore network. Extending the application of electrolytic infiltration to produce bulk structures and coatings using porous media apart from the laser sintered graphite and silicon carbide.
4) Measuring physical properties of the metal matrix composites produced by this method. In this study, the tribological and thermal properties of the metal matrix composite coatings were measured.

Chapter 2: Literature Review

2.1. Selective laser sintering® equipment

Figure 2.1 shows a photograph of a DTM Corporation's Sinterstation® 2000. This machine was used to perform selective laser sintering in the present study. It uses radiant heaters mounted on a heater tray which can heat the powder in the top layer of the feed bins to temperatures up to 145°C and the part bed to temperatures up to 185°C. The part bed in this particular model is cylindrical with a diameter of 12 inches and allows for a maximum build height of 14 inches.

Figure 2.1: A photograph of DTM Sinterstation® 2000 and its various components

This machine uses a CO_2 laser with a maximum laser power of 60W with a fill scan speed of 400 in/s and outline scan speed of 70 in/s. This machine was originally designed to process

Duraform® Polyamide powder. The advantages of SLS are best utilized in the manufacturing of parts with complex geometry in low production runs.

2.2. Indirect laser sintering

In direct laser sintering, the materials to be processed are directly melted using the laser scanner system employed by the selective laser sintering process. In this case, powder bed, feed bin, pistons and cylinder walls are heated to minimize thermal gradients in the part bed to minimize thermal distortion in the sintered parts [42, 43]. Several commercial machines for direct metal processing have been developed and marketed by corporations such as DTM, 3D Systems and EOS in the last two years. The machines and associated metal powders are extremely expensive and build times can be as much as 5 times higher compared to the polymers [29].

Alternatively, for selective laser sintering of metallic and ceramic parts, the associated powders may be mixed with a transient binder which melts under the scanning laser beam and is removed or converted to a non-volatile entity in a post-processing step known as binder burnout [44]. The low melting point of the binder permits the formation of green parts at temperatures close to room temperature [45-47]. This process is called indirect laser sintering. In indirect laser sintering, material systems with high melting points can be processed using a relatively cheap SLS machine like the DTM Sinterstation® 2000 [29, 44, 46].

In this study silicon carbide and graphite were used for creating selective laser sintered parts using a DTM Sinterstation® 2000. The melting points of silicon carbide and graphite is around 2700°C and 3000°C, respectively. Therefore, very high laser power is required to fuse these particles together. This cannot be directly achieved in the SLS machine used in this study because the maximum power achievable by this machine is 50W. Hence, it becomes imperative

to carry out laser sintering using the indirect method. Several different binders such as Nylon-12, PMMA and Novolac Phenolic resin have been used for indirect laser sintering [44-47]. It is required that the binder has a low melting and is able to provide enough strength to the green part to retain its shape [48]. Thus, the binder serves as the connecting media in the green part to maintain its geometric integrity for subsequent post-processing. Among the binders used for indirect laser sintering, phenolic resins have been most widely used for producing laser sintered silicon carbide and graphite [16, 49-52]. Phenolic resins are usually made from condensation polymerization of phenol and formaldehyde and are also known as phenol formaldehyde resins. Under inert atmosphere with high temperature treatment, phenolic resin can provide high vitreous carbon yield which contributes to the structural integrity and electrical conductivity of the preform [49].

2.3. Infiltration into SLS brown parts

The metallic or ceramic parts produced via indirect laser sintering are highly porous which reduces the strength of these parts. Following the production of indirect laser sintered parts, a post processing step is required to make these parts fit for structural applications. Various researchers have developed infiltration systems including infiltrants of silicon into a silicon carbide SLS part and alloy white cast iron into a tool steel SLS [16, 46]. There are also several examples of infiltration steps involving polymer infiltrants such as epoxy resin and cyanoacrylate [5, 51]. These infiltration approaches require high temperature to melt the infiltrant and rely on wetting kinetics to draw the infiltrant into the part [53-55]. Several commercial methods are available for melt infiltration of metals into ceramic preforms. Some of these are described in the following section.

2.3.1. State of the art infiltration methods

Melt infiltration is a method in which a molten liquid, generally a metal, is infiltrated into porous ceramic or metallic preforms. The porous preforms to be infiltrated are soaked in a molten metal which fills the pores [11, 53-57]. The driving force of the melt infiltration process is either spontaneous due to the capillary force of the porous preform, or an external pressure (such as gaseous, mechanical, etc.) is applied to the liquid metal matrix.

1) Gas pressure infiltration

Figure 2.2 shows a schematic of a gas pressure infiltration process. Gas pressure infiltration employs separate chambers for molten metal and the ceramic preform to be infiltrated. Initially both the chambers are kept under vacuum and preheated to achieve complete melting of the metal and outgassing of volatile components in the ceramic preform or woven fibers. The molten metal is then introduced into the chamber containing the porous preform.

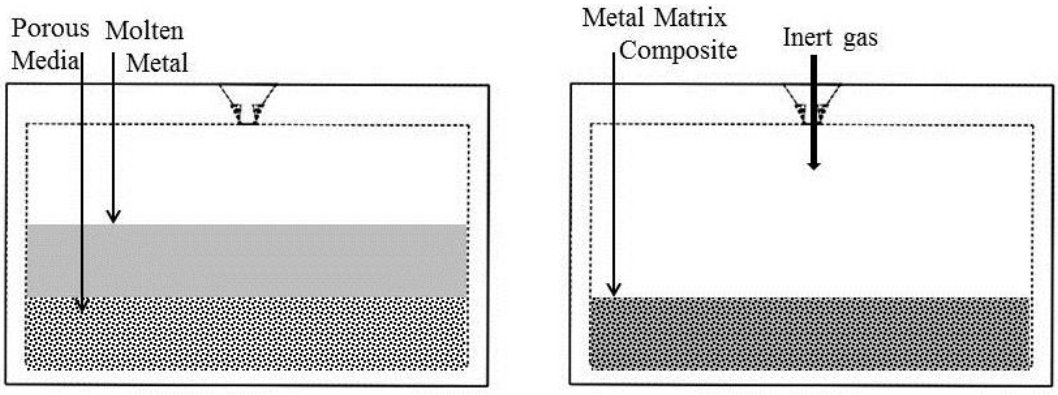

Figure 2.2: Schematic of gas pressure infiltration process

An inert gas such as argon is introduced into the chamber to apply a pressure suitable to push the molten metal through the porous preform until complete filling of open porosity is achieved. Finally excess argon is removed and the metal matrix composite is allowed to cool [58]. This

method is used for carrying out infiltration of aluminum into porous SiC [14], Al_2O_3 [14], graphite [15] and carbon fibers [59].

2) Squeeze casting

Figure 2.3 shows a schematic of squeeze casting infiltration process. Squeeze casting infiltration employs use of movable metal dies mounted on a ram and a chamber in which the infiltration process is carried out. The porous preform is placed in the infiltration chamber, and molten metal is poured in the chamber. The metal dies are then moved at a constant speed for a given time to push the metal through the porous preform. This process also requires preheating of the preform as well as the molten metal [60].

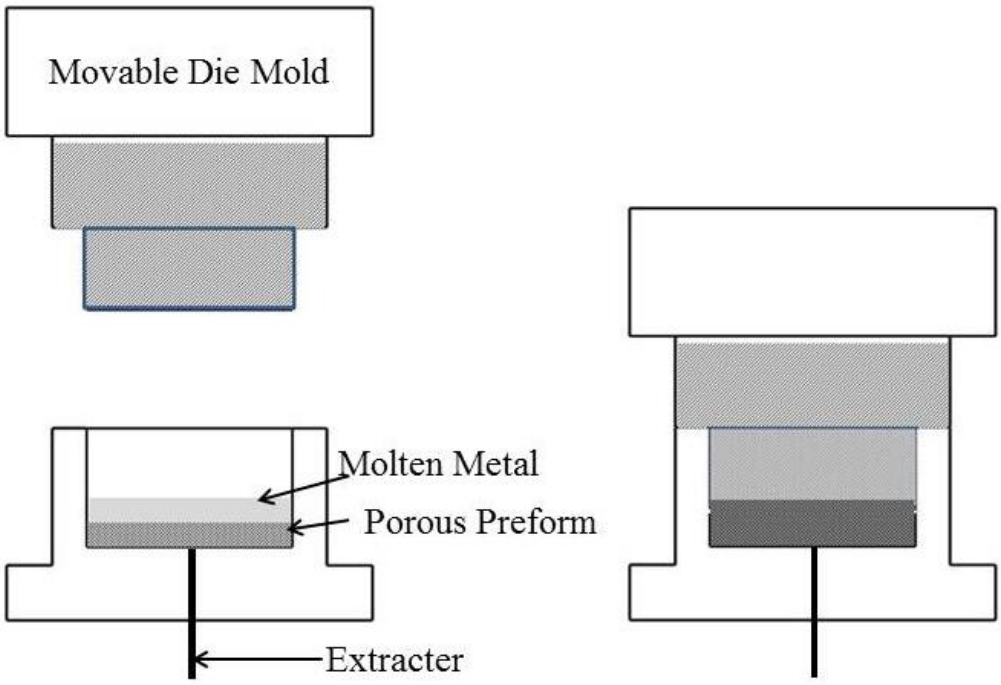

Figure 2.3: Schematic of a squeeze casting infiltration process

This method is used for infiltration of fiber reinforcements with aluminum and magnesium, and the composites thus formed are widely used in the automotive industry [61].

3) Pressure die infiltration

Figure 2.4 shows a schematic of pressure die infiltration process which uses a die casting technology to force a liquid into a porous preform. The porous preform is placed in a die which is filled with a molten metal entering the die through a spruce. This molten metal then penetrates the porous preform under the pressure of a movable piston. The moving solid piston causes turbulent flow of the melt upstream the preform [62]. Aluminum composite materials are made using pressure die infiltration process.

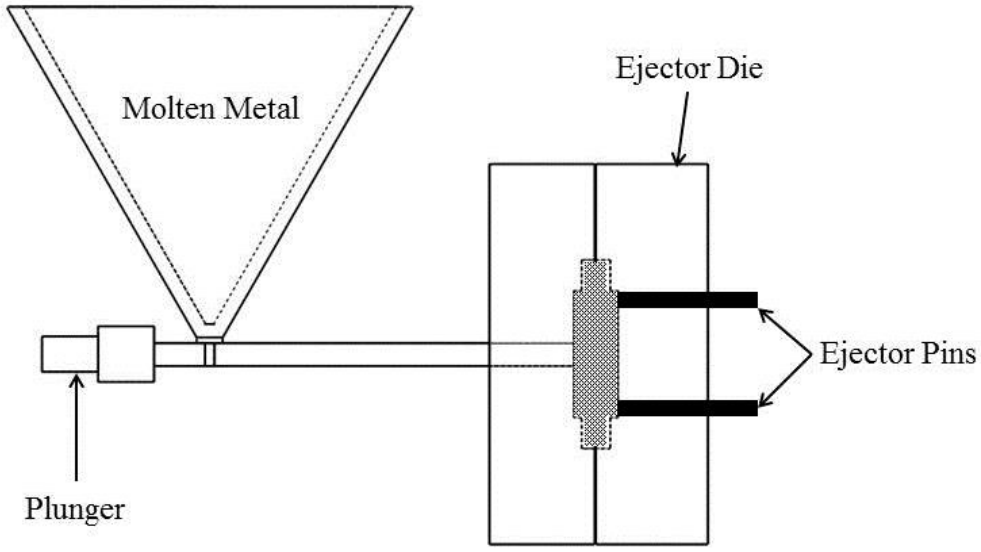

Figure 2.4: A schematic of pressure die infiltration

4) Pressure less infiltration

Pressure-less infiltration techniques work on the principle of capillary action; i.e. the molten metal fills the pores of the ceramic preform due to capillary action. Because most of the ceramics

do not show good wetting with molten metals under normal circumstances, it required to adjust several processing parameters such as alloy composition, atmosphere of the infiltration chamber and the temperature at which infiltration is carried out [7]. For example, for infiltration of porous Al_2O_3 with aluminum, addition of magnesium to the molten liquid and nitrogen atmosphere in the infiltration chamber are necessary [7].

5) Chemical vapor infiltration

Figure 2.5 shows schematic of a chemical vapor infiltration process. Chemical vapor infiltration is an infiltration process in which reactant gases diffuse into an isothermal porous preform and form a deposit. Deposited material is a result of chemical reactions occurring on the pore surface.

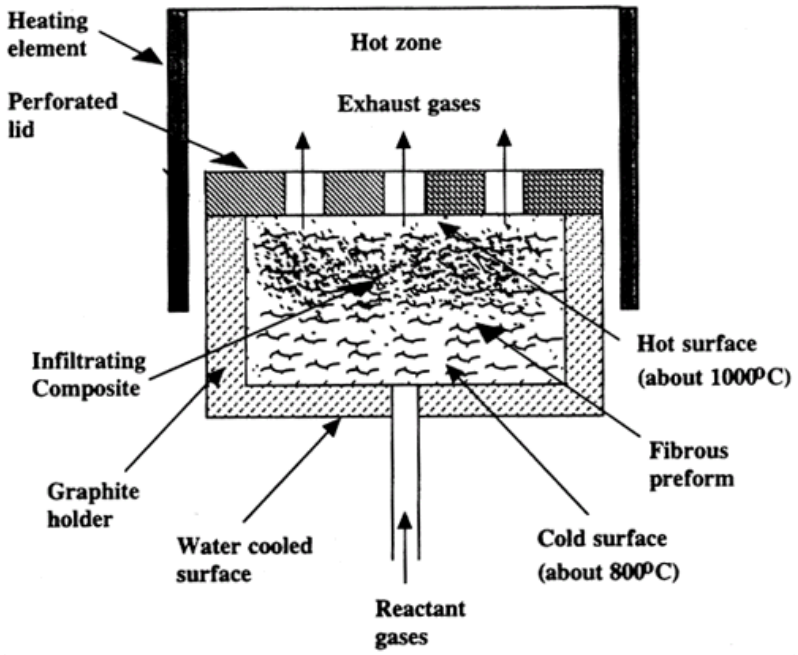

Figure 2.5: A schematic of a chemical vapor infiltration process

The deposition fills the space between the fibers, forming composite material in which the matrix is the deposited material and the dispersed phase is the fibers of the preform [9]. This method is widely used for producing hard composite coatings [63, 64].

2.4. Electrodeposition of metals

Electrochemical deposition of metals involves the reduction of metal ions from aqueous, organic or fused-salt electrolytes. The electrodeposition process is an interfacial phenomenon that occurs at the electrolyte-electrode (figure 2.6) interface when a favorable electric potential is applied. The reduction of metal ions in the aqueous solution is represented by:

$$M^{n+} + ne^{-} \rightarrow M \qquad (2.1)$$

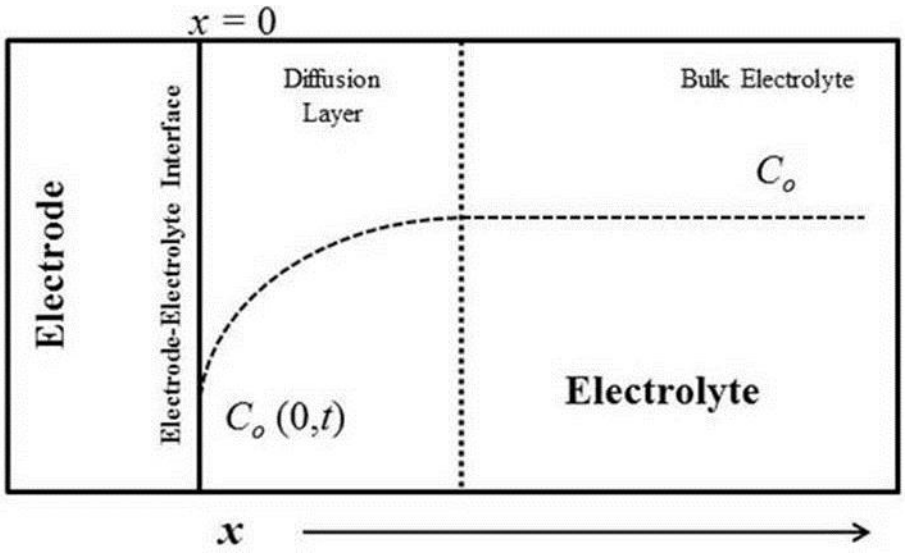

Figure 2.6: A schematic of evolution of ionic concentration as a function of time and distance from the electrode-electrolyte interface in an electrochemical process.

The metal ions are reduced to their elemental form at the interface. Consequently, there is a decrease in the concentration of the metal ions close to the interface. As the applied current is increased, the rate of reaction increases due to the availability of more electrons for the reaction. When the current is increased to a value where $C_o(0,t)$ becomes equal to zero, no more electrons can be accepted by the system. This value of current is called the mass-transfer limited current. Since electrochemical processes involve transfer of electrons, it can be represented using current-potential-time curves. In general, applied current, potential and time can be related using the Butler-Volmer equation of the form [65]:

$$I(t) = nFAk_0\left[C_o(0,t)\exp\left(\alpha_c \frac{nF}{RT}\left(E - E_{eq}\right)\right) - \exp\left(\alpha_a \frac{nF}{RT}\left(E - E_{eq}\right)\right)\right] \qquad (2.2)$$

Where, $I(t)$ is the current applied to the electrolysis cell at time t, n is the number of electrons, F is the Faraday's constant, A is the active surface area of the electrode, k_0 is the rate constant of the electrochemical reaction, C_o is the concentration of metal ions in the electrolyte. α is the charge transfer coefficient and the subscripts c and a denote cathodic and anodic parts of the reaction respectively. E is the applied electrical potential and E_{eq} is the equilibrium potential of the electrode-electrolyte system.

Electrodeposition of any metal involves the dissolution of its ions in a solution, reduction of these ions and finally incorporation product of the reduction reaction into a lattice structure. The dissolution of ions into a solution is an exothermic process, and the energy required for reduction and incorporation into a lattice structure is supplied using an external electric field [65]. These depend on the substrate and the metals ions being deposited. Electrodeposition of metal ions leads to formation of nuclei which subsequently grow as the electrodeposition process is carried forward.

2.4.1. Copper electroplating

Electrochemical deposition of copper is most commonly applied in fabrication of micro components such as heat sinks and interconnects in electronic circuits [66-69]. Elemental copper provides several advantages such as high thermal and electrical conductivity that are critical to these applications. Although the technology for electrodeposition of copper in electronic circuits has advanced rapidly, copper plating also finds use in other areas such as sliding electrical contacts and components [70], protective and decorative applications [71]. Copper deposits can be applied as thermal shock absorbers and barrier coatings in multi-coating systems. Copper coatings also prevent failure due to corrosion because of their high ductility. Copper deposits generally get stained or tarnished when exposed to atmosphere, which is why they often need an overcoating of lacquer or another corrosion-resistant finish [72].

Copper can be electrodeposited using electrolytic and electroless methods which can be acidic or basic in nature. One of the most common alkaline copper baths is a copper cyanide bath. It produces a uniform coating thickness and is easily controllable. It also produces the best relative thickness distribution over all current densities; i.e., it has a good macro-throwing power. However, because of hazard and waste management issues, non-cyanide systems have replaced copper cyanide systems. They require more precise control and surface preparation compared to cyanide systems. Copper sulfate is the most widely used non-cyanide copper plating system. Acid based systems are more commonly used in electroforming, electrorefining and decorative plating. Acid based plating baths contain copper in bivalent ion form and have poorer macro-throwing power and non-uniform metal coating thickness. On the other hand, they have a good micro-throwing power, and hence they are widely used in filling trenches and vias for semiconductor applications.

Electroless copper plating was widely used in 1950s for plated-through-hole printed wiring boards. Major components of an electroless copper plating solution are metal salt and a suitable reducing agent. Since copper salts are insoluble at pH below 4, complexing and buffering agents are necessary to act as a chelating compound to maintain and regulate the pH of the solution. Surface preparation is also necessary, since electroless deposition reaction takes place only on catalytic surfaces. One of the major advantages of electroless copper plating is that it can be used for both conductive and non-conductive surfaces. Electrodeposited copper is also widely used in multi-coating systems such as copper-nickel-chromium system. The cost of copper coating is generally higher for non-cyanide baths when compared to cyanide baths because they require better process control and use of brightening, levelling and wetting agents. Electroless copper plating is also more expensive compared to electrolytic plating.

2.5. Electrochemical co-deposition of metal matrix composite coatings

Electrodeposition of metals is generally used to produce metal or alloy coatings on a given substrate to enhance finish, improve surface properties such as wear and provide protection against corrosion. During the electrodeposition process, it is required that the electrolyte bath is free of any impurities including insoluble impurities such as particles and insoluble anode debris. Several filtering steps are used for purification of the electrolyte for this purpose. If proper precautions are not taken during electrodeposition of pure metals and alloys, debris/particles present in the bath can get incorporated into the coating and adversely affect its properties. In certain cases, the phenomenon incorporation of impurities into the electrodeposited coatings can be useful. If the impurities are properly chosen and added to the electrolyte bath in a controlled fashion, metal matrix composite coatings can be formed [26]. The properties of these coatings

depend on the type and volume of the particles added to the electrolyte bath and the electrodeposition parameters.

There are several studies from the literature that explore the production of metal matrix composite coatings using electrochemical methods [20, 26, 73-75]. Electrodeposited composite coatings have mainly been used to provide dispersion hardened, wear and corrosion resistant coatings. Electroplating of composites improves the properties of electroplating metal coatings and needs only minor adjustments of the commercial electroplating methods. It also provides an energy efficient method to produce composite coatings with a metal matrix. The most commonly used methods for producing composite coatings include laser cladding, metal spraying and internal chemical reactions such as nitriding and oxidizing in the metal coatings [18, 19, 23, 63, 76, 77]. These techniques require high temperatures and expensive equipment. For example, laser cladding is done at temperatures close to the melting point of the matrix material. In general, the composite coatings made in any way are used for enhancing the surface properties such as hardness and wear resistance of the coatings.

2.5.1. Hardening in composite coatings

Hardening or strengthening of a metal or alloy can occur due to following [10]:

1) Direct transfer of load from matrix to the reinforcements through the matrix-reinforcement interface.
2) Indirect strengthening due to dislocation pile up due to thermal mismatch, deformation, precipitation hardening etc. during processing
3) Orowan looping and resistance to dislocation motion due to presence of micron or sub-micron sized particles.

Direct strengthening of metals due to addition of particles can be explained using strengthening mechanisms in fiber reinforced composites. When a load is applied to the metal matrix composite, the load is transferred from the matrix to the high stiffness reinforcements. Thus the metal matrix is strengthened because the reinforcements are able to carry much of the applied load. The particles in a particulate reinforced metal matrix composite have a small aspect ratio, and the strengthening due to transfer of load is not lower when compared to fiber reinforced composites. The improvement in the mechanical properties due to direct strengthening can be computed using rule of mixtures [10]:

$$\alpha_c = V_m \alpha_m + V_r \alpha_r \qquad (2.3)$$

where, α_c, α_m and α_r are the concerned property of the composite, matrix and the reinforcements respectively. V_m and V_r are the volume fractions of the matric and the reinforcements in the composite, respectively.

Most of the ceramic particles used as fillers in a metal matrix have a much lower coefficient of thermal expansion compared to the metal matrix. Thus when a ceramic particle is embedded in the metal matrix, thermally induced dislocations are formed at the matrix-reinforcement interface which cause indirect strengthening of the composite. This type of strengthening mechanism is most prevalent in composites that are melt processed, i.e. via melt infiltration, casting, etc. In age hardnable metal matrices, such dislocations can act as nucleation site for precipitates formed during age hardening [73, 78].

Orowan looping occurs in metal matrix composites when the size of the particles is small and is absent in particulate reinforced composites with particle size of reinforcement of the order of tens of microns [79-81]. In certain cases, when the particles with size > 10 microns might have

irregular shape, Orowan looping may be present as a strengthening mechanism. This is because the sharp corners of the matrix-reinforcement interface can effectively serve as hindrances to dislocation motion [80].

Metal matrix composites containing ceramic particles such as oxides, nitrides and carbides show better mechanical properties such as higher strength and hardness when compared to pure metals and alloys. Generally the addition of such particles to the metal matrix leads to an increase in brittleness and decrease in percent elongation. For example, the micro hardness of a composite of Ti6Al4V alloy ranges from 398 HV to 1140 HV due to the addition of TiN particles [18]. The hardness of the ceramics particles such as that mentioned above is very high compared to the metal matrix. For example, TiN has a Vickers's Hardness number of 2600 HVN which is much higher that the micro-hardness of Ti6Al4V-TiN composites. The micro-hardness of the metal matrix composite is of the same order as the pure metal or alloy. On the other hand, presence of soft particles such as graphite or MoS_2 as reinforcements in the metal matrix composite leads to an overall reduction in hardness and strength [25].

In general, the increase in the volume fraction of incorporated particles leads to an increase in the hardness of the composite coatings. The hardness of a metal matrix composite is directly proportional to the square-root of the volume fraction of reinforcement particles [20]. Particle size of fillers added to the bath in electrochemically deposited metal matrix composite coatings is of the order of 1 micron or lower. Hardening of the metal matrix composites produced in this manner is dependent on the extent of agglomeration of reinforcement particles and interparticle distance. Contrary to hardness, the strength of the metal matrix composite increases with the addition of the filler until it reaches a maximum value. Further addition of particles leads to a

decrease in the strength of the composite. Brown and Gow found a maximum ultimate tensile strength and hardness for composite at approximately 10 vol% [82].

Although metal matrix composites offer advantages of high strength and high hardness compared to the matrix materials, such properties are desired in bulk structures. For example, materials which possess high strength and hardness are ideal for making pressure dies, machining tools and automotive parts. Since electrochemical deposition of metals and alloys is a much slower process and requires a higher degree of control compared to the conventional methods for producing bulk structures, it is not used for making bulk structures [20].

2.6. Wear resistance in composite coatings

Electrochemical deposition of metals and alloys is most widely used for coating materials to improve their surface properties such as hardness, wear rate and corrosion resistance. In this particular field of manufacturing, electrochemical deposition of composite coatings provides several industrial applications. The presence of a hard particles like SiC and soft particles such as graphite in metal coatings can enhance its tribological properties. Such a coating can improve the life of the surface of machining tools and machine parts that are in moving contact.

Incorporation of hard particles such as SiC, TiN, WC and diamond in metal matrices improve resistance to abrasive wear when compared to pure metal coatings [20]. Presence of micron and sub-micron SiC particles in a Ni matrix improves its wear resistance by a factor of 6 [74]. The improvement in the wear resistance is higher when the density of silicon particles per unit volume in the coating is increased. A high and uniform surface coverage of particles provides a large contact area, and, the smaller the particle size, the more difficult they are removed during abrasion. However, addition of a large quantity of particles can make the coatings brittle and

prone to cracking. Even though soft particles such as graphite, MoS_2 and PTFE can significantly reduce the hardness of a metal matrix; their presence in coating same can significantly improve the wear resistance in dry wear conditions [83, 84]. This is because soft particles are easily broken down during wear and form a layer on the composite as well as the counter surface. This provides a self-lubricating effect which significantly reduces the coefficient of friction and wear rate between the sliding surfaces.

2.7. Challenges in manufacturing of electrochemically co-deposited composite coatings

During electrochemical deposition, particle incorporation in the metal matrix occurs in two steps. First a particle is transferred from the bulk electrolyte to the electrode under electrophoresis and then the charged particle interacts with the electrode surface leading to particle incorporation into the matrix. The electrode-particle interaction depends on several parameters such as properties of suspended particles and their shape, size, surface roughness and polarization. This interaction is also dependent upon process-parameters such as bath agitation, pH, applied current, particle loading, etc. [20, 26].

2.7.1. Effect of particle size

With the increase in the size of the particles introduced into the electrolyte bath, the weight fraction of the particles incorporated into the metal matrix increases. However, according to Bozzini *et al.* the increase in the particle size reduces the number density of the particles introduced into the metal coatings [85]. It is well known that the particle size selection for electrochemical deposition of composite coatings is very difficult. It is required that the particles are large enough that they can be easily suspended in the bath but they need to be small enough so that the poor surface quality in the coatings can be avoided.

2.7.2. Effect of particle shape

There are not many studies on the effect of particle shape on electrochemically deposited composited coatings. However, it is well established that an increase in the aspect ratio of the particles used in electrodeposition bath leads to poorer results [20]. One study on Al_2O_3 codeposition with Ni reports that the incorporation of Al_2O_3 fibers in the matrix is very poor compared to the Al_2O_3 spherical particles [86].

2.7.3. Effect of particles on polarization of the cathode

The co-deposition of particles with the metal ions can increase or decrease the highest current density that can be applied during electrochemical deposition. In certain cases, the inert particles in the bath cover the surface of the cathode and can lead to a decrease in the area available for deposition of the metal [20].

2.8. Electrodeposition of pure metals as an infiltration technique

As discussed earlier, the conventional methods of infiltration of ceramics with metals use a melt infiltration to produce metal matrix composites. Due to the relatively high melting point of metals, production costs are usually high, and the process has poor environmental sustainability. Such a route of process processing may also encounter restrictions because of infiltration atmosphere, owing to chemical reaction between metal and introduced gas which can lead to poor mechanical properties in metals [17].

Electrolytic deposition from aqueous solutions can take place at room temperature without affecting structural and physical properties of the substrate onto which material is deposited. Although electrochemical techniques offer this advantage, the working conditions are much

more complicated compared to infiltration of molten metal into a ceramic preform. There have been very few studies on infiltration of metals into porous metals or ceramics in the past [29, 87]. The major obstacle in infiltration of metals into porous preforms is the depletion of ions inside the porosity network of the preform [65]. If the reacting species, i.e. metal ions, are in short supply, the mass transfer of that species becomes rate limiting. This is called concentration polarization. Sukwon Jung and co-workers have reported successful infiltration of copper into 60 μm thick Ni-YSZ cermets for fuel cell applications by carrying out electrodeposition while flowing an electrolyte through the porous material [88]. According to this study, the electrolyte must be transported to the interior porous structure to avoid depletion of ions inside the porosity.

Chapter 3: Derivation and Verification of Mathematical Model

This chapter summarizes the mathematical model of flow electrolysis cells used for electrodeposition of copper into the porous templates. The most established mathematical description of porous electrode theory was provided by Newman and Tobias [34]. Several studies have used this description, either in original or modified forms [36, 39, 40]. In the present study, a modified form of this porous electrode theory was used to develop constitutive equations for the electrochemical systems. These equations were solved using a finite element method in Comsol 4.4, and experiments were carried out to verify the model. This was done for both flow-through and flow-by porous electrodes.

3.1. Model geometry

Electrodeposition of a metal can be represented by the following reduction reaction at the cathode:

$$M^{n+} + ne^{-} \rightarrow M \qquad (3.1)$$

An oxidation reaction takes place at the counter electrode to complete the circuit:

$$O^{n-} \rightarrow O + ne^{-} \qquad (3.2)$$

The transfer of electrons takes place due to the externally applied electrical current. The distribution of this electrical current in the porous electrode can be used to predict the spatial distribution of the electrochemical reaction.

A physical model of an electrolysis cell employing porous electrodes is shown in figure 3.1. The cell consists of cathodic and anodic sections separated by a porous separator or membrane. Both cathodic and anodic sections contain rectangular electrodes of the same dimensions as the

sections themselves. The cathode and anode are porous electrodes with thickness D in X direction, length L in Y direction and width W in Z direction. The anode and cathode are separated by a porous membrane of thickness D_m to insure electrical insulation. The pore network of the porous electrodes is filled with the electrolyte using an external pumping mechanism. It is assumed that the external pump is pumping the electrolyte through the porous electrode at a constant flow rate such that the reactants taking part in the electrochemical reactions are constantly replenished.

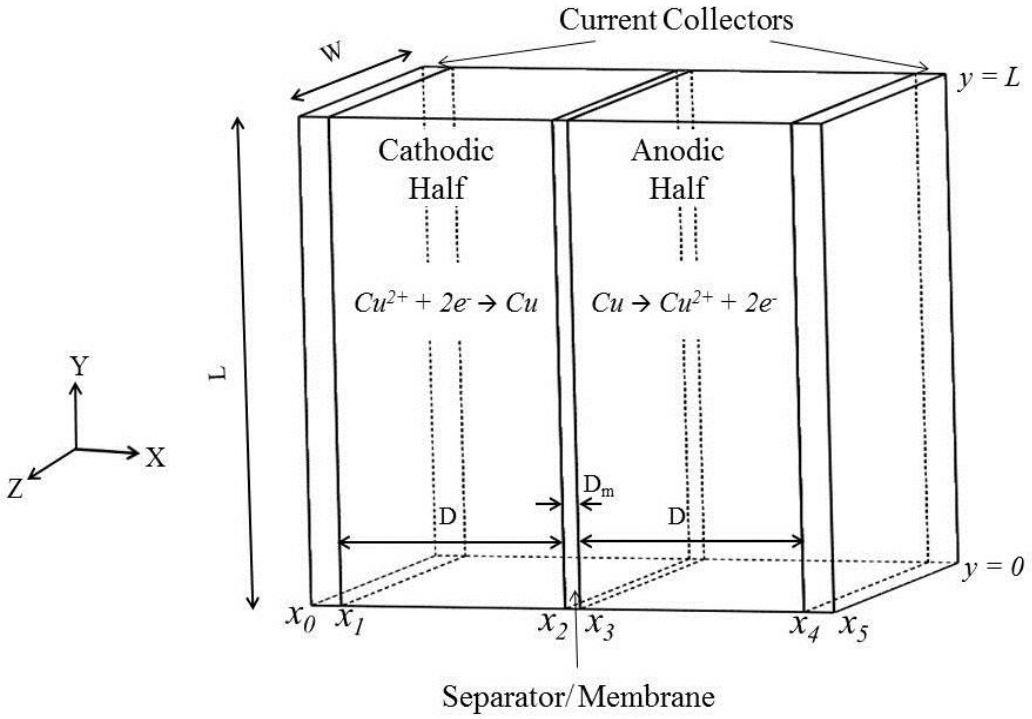

Figure 3.1: A schematic of a electrochemical reactor employing porous cathode and anode

Based on the direction of the flow of the electrolyte, the resulting flow cell can be classified into two categories [89]:

1) **Flow-through cell:** In a flow through cell, the electrolyte stored in a reservoir is pumped through the porous electrodes in the X direction. The electrolyte first flows through the

anode, where the anodic half reaction takes place. The electrolyte then passes through the cathodic reactor where the cathodic half reaction takes place. The cathode and anode are separated by a porous separator such as a Nomex felt.

2) **Flow-by cell:** In a flow by cell, the electrolytes for cathodic and anodic half cells can be stored separately. The electrolytes are pumped through the cathode and anode respectively in Y-direction. The products of the electrochemical reactions at cathode and anode diffuse through the separator/ membrane and complete the electrical circuit.

In this study, we performed a mathematical analysis on a stationary volume element the electrochemical reactor shown in figure 3.1.

3.2. Constitutive equations

The equations derived in the section are applicable to both flow-by and flow-through porous electrodes. The governing electrochemical equations are:

At cathode: $Cu^{2+}+2e^{-} \rightarrow Cu$ (3.3)

At anode: $Cu^{2+}+2e^{-} \rightarrow Cu$ (3.4)

Following assumptions were made while deriving the constitutive equations for the electrochemical cells:

1) The electrolyte fills the pore network nearly completely or completely
2) The change in the bulk concentration of the ions in the electrolyte is negligible
3) The properties of the electrode, electrolyte and the membrane/separator are isotropic and homogenous

4) Fluid flow is treated as incompressible flow

5) Dispersion in Y direction and variations in Z direction are neglected

6) Side reactions such as hydrogen evolution and oxygen evolution are neglected

7) The temperature is assumed to be constant throughout the process

8) Solvent permeation and drag in the membrane are ignored

3.2.1. Variables and constants

Symbol	Parameter	Value	Unit
α	Symmetry Coefficient	0.54	1
n	Number of Electrons	2	1
k_0	Reaction Rate Constant	5E-06	m/s
F	Faraday's Constant	96485	C/mol
f	Constant	nF/RT	1/V
R	Universal Gas Constant	8.31	J/mol-K
T	Temperature	298	K
a	Electrode Specific Surface Area	3.50E+05	1/m
E_0	Standard Electrode Potential	0.334	V
z_i	Charge number of the ions	2	1
D_i	Diffusion Coefficient of the ion	3×10^{-6}	cm^2/s
C_{cu}	Concentration of reduced Cu	1	1

Table 3.1: Symbols and values of various constants used in the constitutive equations

Symbol	Parameter	Unit
ϕ_s	Electrode Potential	V
ϕ_l	Electrolyte Potential	V
ϕ_m	Potential in the Membrane	V
I_{app}	Applied Current	A
j_{app}	Applied Current Density	A/m^2
j_s	Current Carried by the Electrode	A/m^2
j_l	Current Carried by the Electrolyte	A/m^2
j_{BV}	Reaction Current Density	A/m^2
σ	Electrode Conductivity	S/m
σ_{eff}	Effective Electrode Conductivity	S/m
κ	Electrolyte Conductivity	S/m
κ_{eff}	Effective Electrolyte Conductivity	S/m
ε	Electrode Porosity	1
η	Overpotential	V
$C_{cu}{}^{2+}$	Concentration of Cu^{2+}	mol/m^3

Table 3.2: Symbols corresponding to various variables used in the constitutive equations

The definition of various symbols used in the derivation can be found in tables 3.1 and 3.2.

3.2.2. Equations at the electrodes

The equations were derived by extending the concepts of a flat electrode to a porous electrode based on the approach developed by Newman and Tobias [34]. The density of the electric current

carried by the matrix and the electrolyte can be found using Ohm's law. The application of Ohm's law to the electrolyte in the pores gives:

$$\nabla \phi_s^{n,p} = \frac{-j_s^{n,p}}{\sigma_{eff}} \quad (3.5)$$

$$\nabla \phi_l^{n,p} = \frac{-j_l^{n,p}}{\kappa_{eff}} \quad (3.6)$$

The superscripts *n* and *p* refer to the corresponding parameter in the cathodic and anodic sections respectively. The potential difference between the positive and negative electrode can be calculated by:

$$E_{app} = \phi_s^p(x_1) - \phi_s^n(x_4) \quad (3.7)$$

The reaction current density or Butler-Volmer current density can be found from the first order derivative of the current density in the electrode [40]:

$$\nabla j_s^{n,p} = -a j_{BV}^{n,p} \quad (3.8)$$

$$\nabla j_l^{n,p} = a j_{BV}^{n,p} \quad (3.9)$$

From equations (3.5), (3.6), (3.7), (3.8) and (3.9),

$$\sigma_{eff} \cdot \nabla^2 \phi_s^{n,p} = a j_{BV}^{n,p} \quad (3.10)$$

$$k_{eff} \cdot \nabla^2 \phi_l^{n,p} = -a j_{BV}^{n,p} \quad (3.11)$$

The electric potential observed by the ions in the solution is the difference between the potential in the electrode matrix and the liquid electrolyte. Hence, the overpotential can be found from the following relation [35]:

$$\eta^{n,p} = \phi_s^{n,p} - \phi_l^{n,p} - E_{eq} \quad (3.12)$$

The equilibrium potential in its simplest form can be calculated using Nernst equation:

$$E_{eq} = E_0 + RT\ln(C_{Cu^{2+}} / C_{Cu}) \quad (3.13)$$

The overpotential can be related to the local current density by using a polarization equation [34]. In the present work, the Butler-Volmer equation was used as follows:

$$j_{BV}^{p} = nFk_0[\exp(-\alpha f\eta^{p}) - \exp((1-\alpha) f\eta^{p})] \quad (3.14)$$

$$j_{BV}^{n} = nFk_0[\exp(-\alpha f\eta^{n}) + \exp((1-\alpha) f\eta^{n})] \quad (3.15)$$

Since copper in its reduced form is a solid, C_{Cu} in solution is always equal to 1.

The effective conductivity of the electrode is given by [39, 40]:

$$\sigma_{\text{eff}} = \sigma\left(1-\varepsilon\right)^{3/2} \quad (3.16)$$

The electrolyte conductivity κ_{eff} appearing in (3.6) is calculated using:

$$\kappa_{\text{eff}} = \frac{F^2}{RT}\varepsilon^{3/2}\sum_i z_i^2 D_i C_i \quad (3.17)$$

where the sum is over all charged species and the Bruggemann correction for the conductivity of electrolytes in a porous electrode has been included.

3.2.3. Equation at the separator

Ohm's law was used to define the conduction of electric current inside the porous separators used in both the cases. The concentration of the current carrying ion was assumed to be constant throughout the separator. In the case of the polypropylene separator, the Bruggemann rule used in equation (3.17) was used to calculate the effective electrical conductivity. The porosity of the electrode was replaced with the porosity of the separator. Similarly, pore volume fraction of the ion exchange membrane was used to find the conductivity of the electrolyte inside the

membrane. For the ion exchange membrane used in flow by electrolysis, it was assumed that the electric current was carried across the membrane by hydrogen ions. This assumption was made because the size of hydrogen ions is very small as compared to copper ions in the solution. Also, since Cu^{2+} ions are hydrolyzed in the solution, a large quantity of H^+ or H_3O^+ ions can be present in the electrolyte. In general Ohm's law was used for both the porous separator and the ion exchange membrane:

$$\kappa_{eff}^{mem} \cdot \nabla \phi_{mem} = I_{app} \frac{D_m}{A} \qquad (3.18)$$

3.2.4. Boundary conditions

The boundary conditions in the porous electrode in both types of cells depend on the potential distribution [40]. The boundary conditions involved in the charge transfer remain same for both types of electrolysis cells and are shown in equations (3.19) and (3.20):

$$-\sigma_{eff} \cdot \nabla \phi_s = \begin{Bmatrix} j_{app}(x = x_1) \\ -j_{app}(x = x_4) \\ 0(x = x_2, x = x_3, y = 0, y = L) \end{Bmatrix} \qquad (3.19)$$

The charge leaving the porous electrode is balanced by the charge entering the electrolyte:

$$-\kappa_{eff} \cdot \nabla \phi_l = \begin{Bmatrix} -j_{app}(x = x_2) \\ j_{app}(x = x_3) \\ 0(x = x_1, x = x_4, y = 0, y = L) \end{Bmatrix} \qquad (3.20)$$

In the separator/ ion exchange membrane, the only boundary conditions are applicable on the electrolyte/ separator interface:

$$\nabla \phi_m = \begin{Bmatrix} \phi_l(x = x_2) \\ \phi_l(x = x_3) \end{Bmatrix} \quad (3.21)$$

3.3. Determination of constants

The constants used in the derivation of the constitutive equations are shown in table 3.1. To determine these constants a variety of electrochemical techniques were used. These techniques included: cyclic voltammetry, linear scan voltammetry and Tafel polarization. Details of these measurements and calculations are provided in chapters 4, 5 and 6.

3.4. Method of solution

The constitutive equations for a stationary volume element were discretized and solved using a finite element method in commercially available package Comsol 4.4. A Lagrange-quadratic basis was used for all of the simulations. A triangular mesh with 3055 mesh elements was used. The relative error tolerance was set to 10^{-6}.

3.5. Verification

The constitutive equations were solved using porous graphite felt as the porous electrolyte. The parameters were chosen such that they represented the graphite felt as the porous electrodes in the cathodic and anodic sections and Nafion^{TM} 117 as the membrane in a flow by electrolysis cell. These parameters can be found in table 3.3. A flow cell shown in figure 4.13 (chapter 4) was prepared. 2.5 mm thick graphite felt was used as the porous cathode. A soluble porous anode was prepared by stacking copper mesh. The experiments were carried with a solution of 0.8M $CuSO_4$ and 0.5M H_2SO_4 in deionized water. A constant current was applied by operating the electrochemical workstation in galvanostatic mode in a two electrode setup. The resulting

potential difference between the cathode and the anode was measured. This was compared with the value of E_{app} obtained from equation (3.7).

Figure 3.3 shows a comparison of calculated values of applied potential and those determined experimentally. A good agreement between the theoretical and experimental values was observed. It was also observed that the experimentally determined value of the applied potential were higher than the calculated value. This can be attributed to potential drops caused by the current collectors, contact resistance between the electrodes and current collectors and connections between the electrolysis cell and the galvanostat. The equations were solved for applied current, I_{app} of 50 mA, 100 mA, 150 mA and 200 mA. The distribution of electric potential in the cathode and anode was obtained and is shown in figure 3.2 and equation (3.7) was used to find E_{app}.

Parameter	Value	Units
κ	0.2	S/m
σ	1000	S/m
ε	0.5	1
C_{cu}^{2+}	800	mol/m^3
D	0.25	mm
D_m	200	μm

Table 3.3: Parameters used for validation of the model

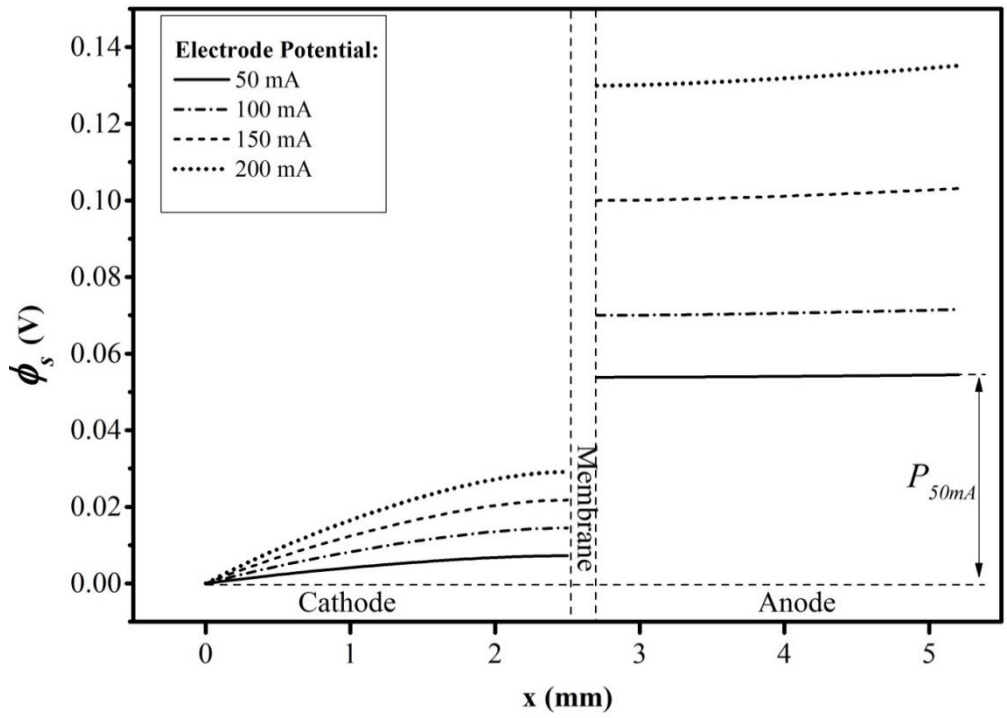

Figure 3.2: Distribution of potential in the cathode and anode at various values of I_{app}.

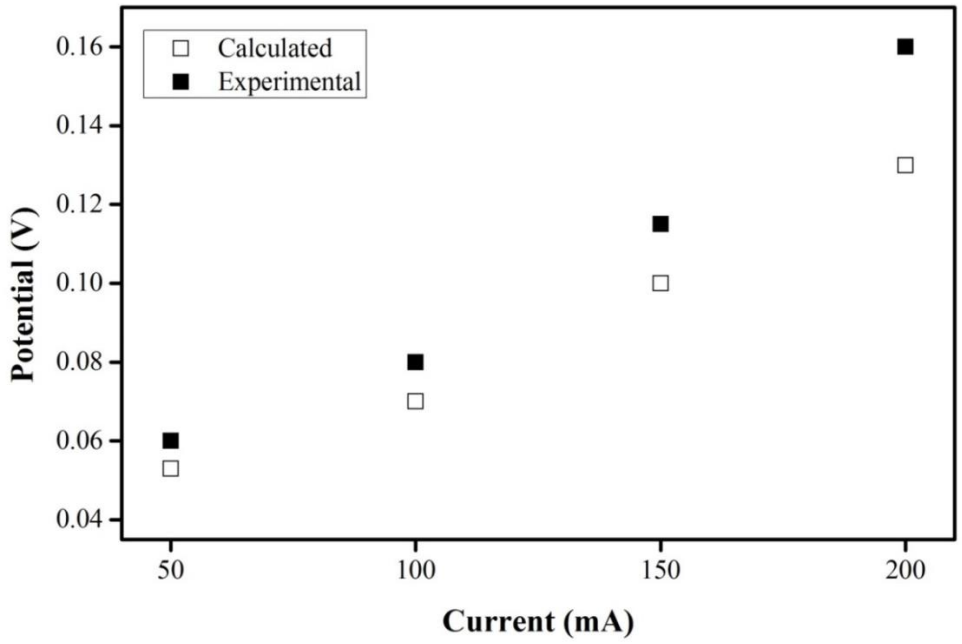

Figure 3.3: The comparison of E_{app} obtained theoretically and experimentally for the flow-by cell with graphite felt electrodes.

3.6. Results

The effect of various parameters such as: electrolyte conductivity, electrode porosity, electrode thickness, electrode conductivity and applied current was computed and dimensionless current distribution I ($I(x)/I_{app}$) was plotted against dimensionless distance X (x/l), where l is the thickness of the porous electrode. The distribution of current in the porous cathode was used to predict the distribution of electrochemical reaction rate in the electrode. For producing completely infiltrated parts, it is essential that the reduction of copper ions occurs predominantly inside the porous part. Hence it is required to achieve higher current density inside the porous part compared to the geometrical surfaces.

3.6.1. Effect of electrolyte conductivity

Figure 3.4 shows the effect of electrical conductivity of the electrolyte on distribution of reaction current distribution. It was seen that with an increase in specific conductivity of the electrolyte, our model predicted that the reaction rates would become more uniform throughout the thickness of the porous part. However at lower specific conductivities, our model predicted a higher reaction rate at the face. The effect of specific conductivity can be explained on the basis of potential drop and change in concentration across the electrode. When the conductivity of the electrolyte is low, copper, due to higher electrical field and higher mass transport at the face of the porous part, has the tendency to build up faster at the face [69]. High conductivity copper electrolytes have been long known to have higher throwing power as a result of their ability to reduce potential drop due to geometrical non-uniformities in an electrode [90]. This property has been utilized successfully in through hole plating of circuit boards as well as in copper via filling in semiconductor industry [69, 91].

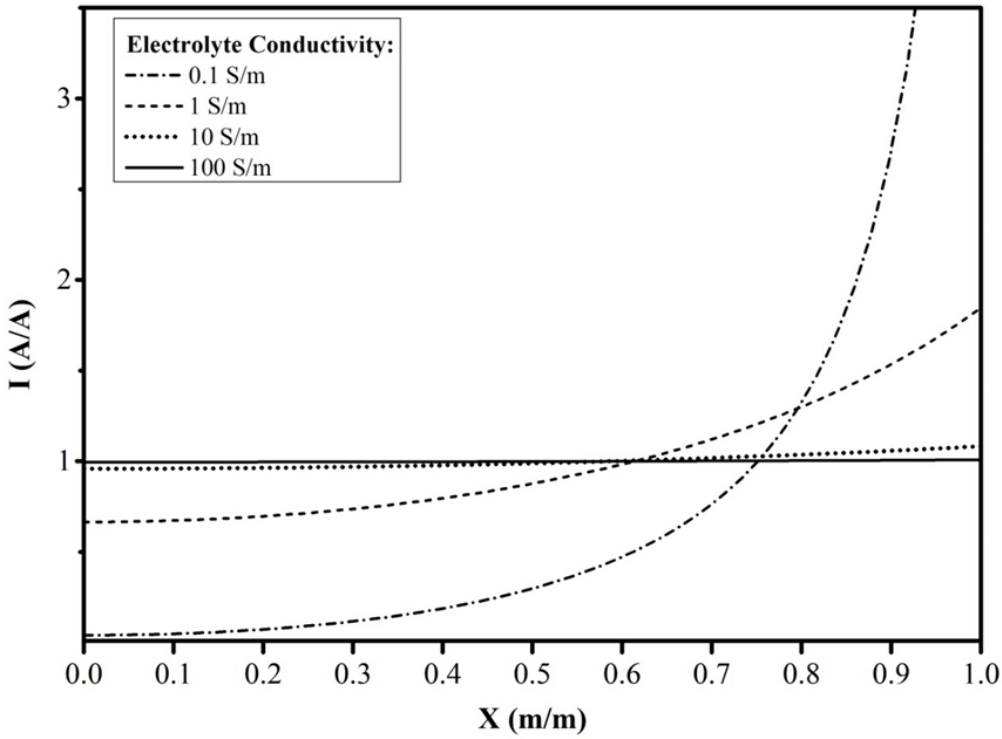

Figure 3.4: Computed effect of electrolyte conductivity on reaction current distribution in the porous electrode matrix. All the parameters except electrical conductivity are the same as those found in table 3.3.

3.6.2. Effect of electrode porosity

Figure 3.5 shows the effect of electrode porosity on the current distribution in the cathode. The change in porosity leads to the variation in both the value and distribution of the over-potential by changing effective conductivity of the electrode and the electrolyte. For high porosity, the over-potential distributes mainly on the region close to the current collector. The maximum over-potential is much more negative than that for lower porosity due to the decrease in electrode conductivity. As the electrode porosity decreases, the values of over-potential in the area close to the membrane become higher, and the distribution of over-potential becomes more uniform throughout the electrode [40].

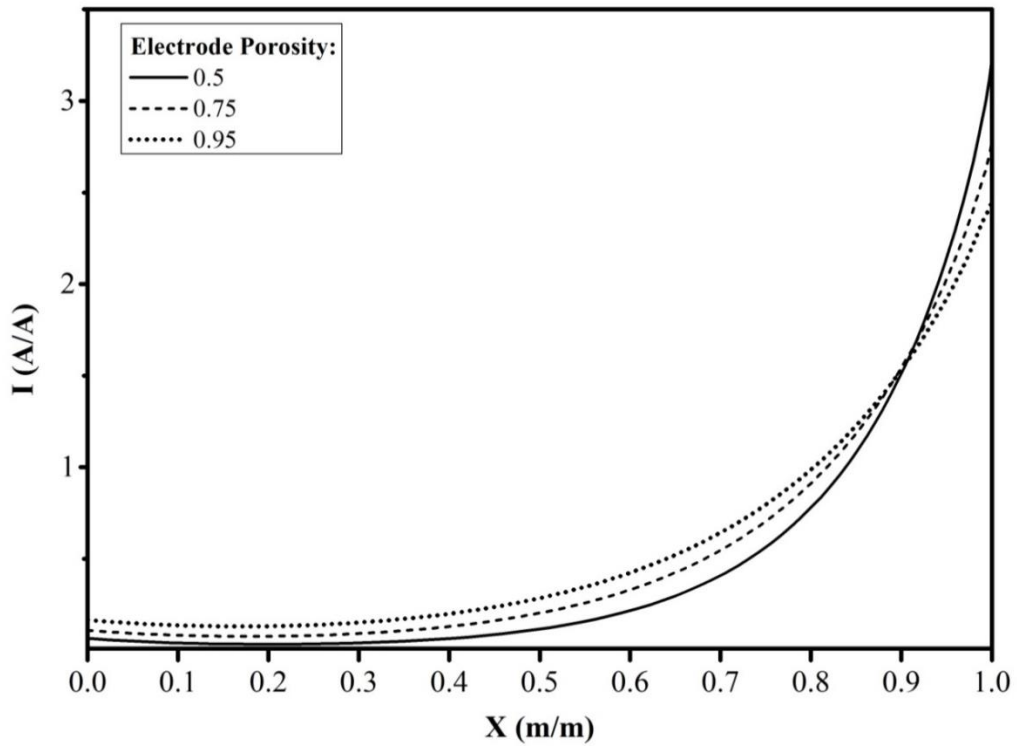

Figure 3.5: Computed effect of electrode porosity on reaction current distribution in the porous electrode matrix. All the parameters except pore volume fraction are the same as those found in table 3.3.

3.6.3. Effect of electrode thickness

Figure 3.6 shows the effect of electrode thickness on the current distribution in the cathode. As the electrode thickness decreases the potential drop in the electrolyte across the porous electrode decreases. This is because the overall resistance of the electrolyte in the pore network is dependent on the effective solution conductivity as well as the distance over which the potential drop is measured. The overall resistance of the electrolyte in the pore network is equal to the product of the effective solution conductivity and thickness of the electrode. As the thickness is reduced, the overall resistance decreases. Therefore, the drop in potential across the electrode also decreases. Hence, a more uniform potential distribution in the electrolyte in the pore

network can be expected, which leads to a more uniform distribution of reaction current in the porous electrode.

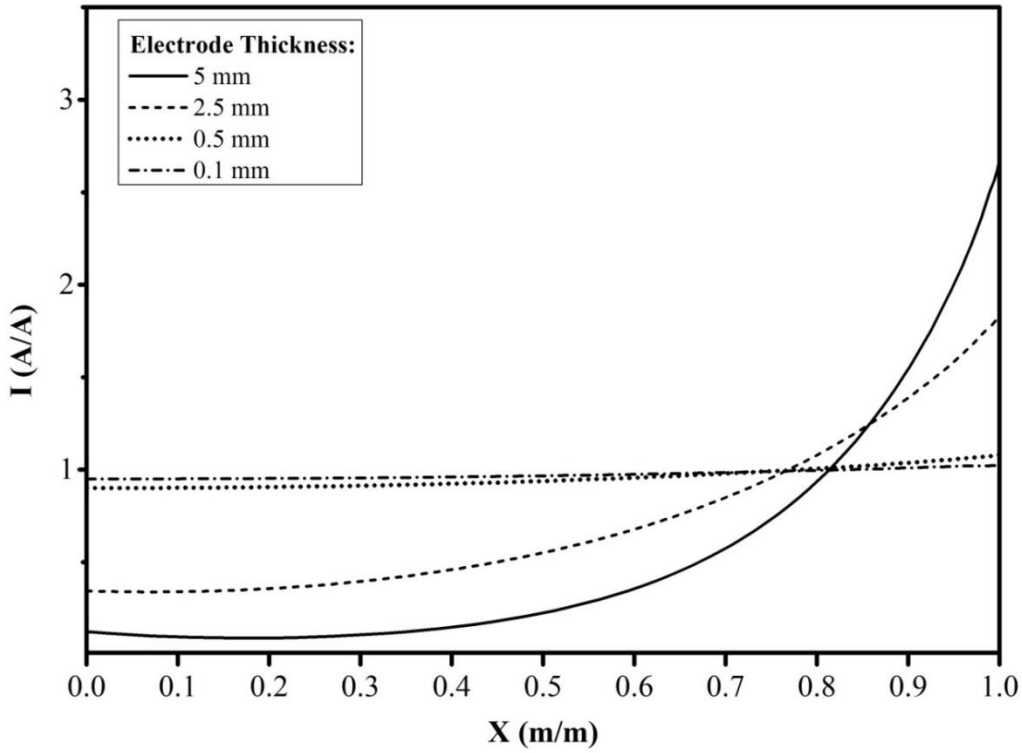

Figure 3.6: Computed effect of electrode thickness on reaction current distribution in the porous electrode matrix. All the parameters except electrode thickness are same as those found in table 3.3.

3.6.4. Effect of electrode conductivity

Figure 3.7 shows the effect of electrode conductivity on the distribution of reaction current in a porous electrode. As the electrical conductivity of the porous electrode is decreased from 1000 S/m to 1 S/m, the rate of electrochemical reaction becomes faster near the current collector. As the electrode conductivity is reduced, the electron transfer from the porous matrix to the copper

ions reduces [37]. Hence, copper electrodeposits such that it provides a “bottom-up” filling of the porous electrode.

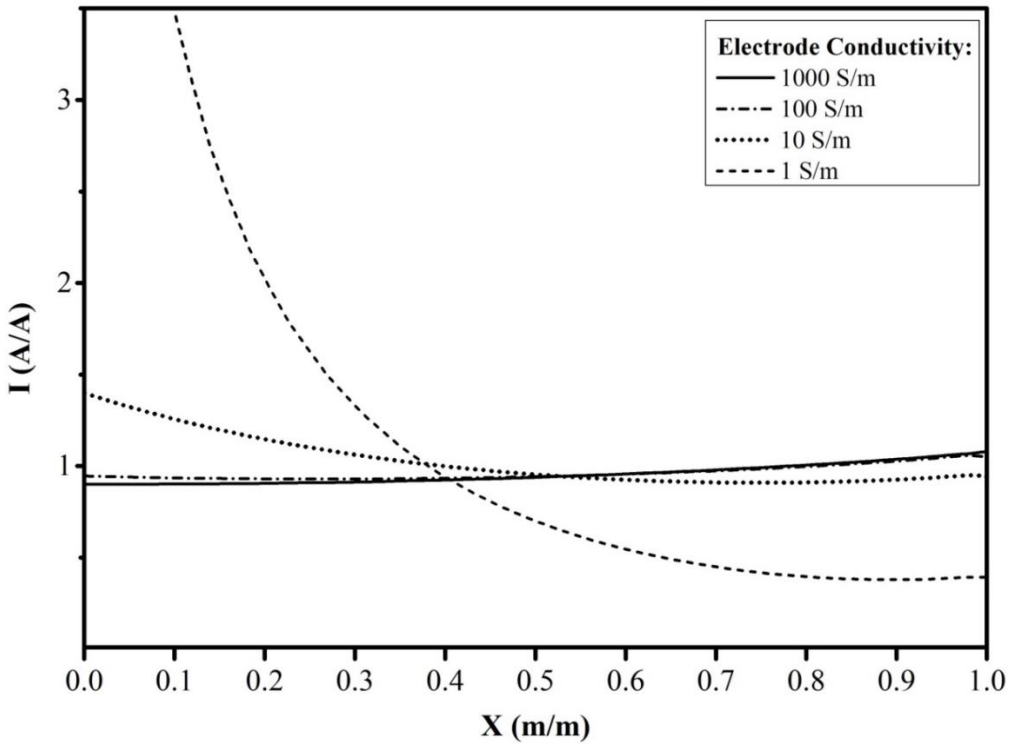

Figure 3.7: Computed effect of electrode conductivity on reaction current distribution in the porous electrode matrix for D = 500μm. The rest of the parameters are the same as those found in table 3.3.

3.6.5. Effect of applied current

Figure 3.8 shows the effect of electrodeposition current on the distribution of electrochemical reaction. It was found that as the applied electrical current is increased, the rate of reaction at the face of the porous electrode increased and that near the current collector decreases. This is because the potential drop at the face is a product of applied current, distance and conductivity of the electrolyte. Due to an increase in the potential drop, the electrochemical reaction takes place at the face of the porous electrode.

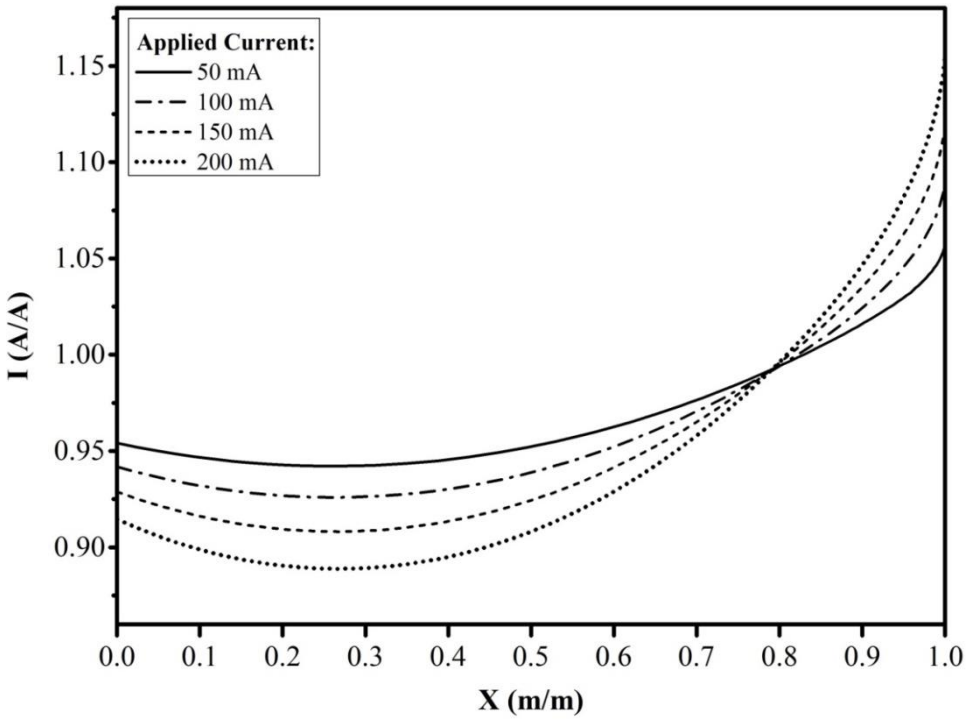

Figure 3.8: Computed effect of applied current on reaction current distribution in the porous electrode matrix for D = 500μm and σ = 100S/m. The rest of the parameters are the same as those found in table 3.3.

3.7. Summary

The model equations were solved, and it was found that when the electrochemical reaction is activation controlled, the distribution of the electrochemical reaction inside a porous electrode matrix depends on several parameters. A uniform distribution of reaction current inside the porous electrode matrix is desired when a current collector is not present. Increasing the electrolyte conductivity and electrode porosity makes the electrochemical reaction rate more uniform throughout the porous matrix. On the other hand, decreasing electrode thickness and applied current leads to more uniform reaction through the porous matrix. A decrease in electrical conductivity of the porous matrix makes the distribution of current uniform and at very

low values of electrical conductivity; most of the reaction takes place close to the current collector. It should be noted down that the constitutive equations do not allow us to compute the reaction rates for polarizable electrodes such as those made of insulating materials and electrolytes with very low conductivity. This is because the equation (3.5 **)** and (3.16 **)** become unstable if the electrical conductivity of the porous matrix is close to 0. From the findings of this chapter following attributes are desired for electrolytic infiltration:

1) Highly electrically conductive electrolyte.
2) High pore volume fraction in the porous preform.
3) Low electrical conductivity of porous preforms.
4) It is easier to perform electrolytic infiltration into thin porous preform at small applied current.

Chapter 4: Materials and Methods[1]

Since this research aims at post-processing of laser sintered inter-metallic and ceramic preforms, the parts were made using a DTM Sinterstation® 2000. In this chapter the experimental methods are discussed in detail, beginning with pre-processing of SLS powder mixture, SLS part fabrication, post-processing of the preforms, porosity measurements, electrodeposition and SEM characterization.

4.1. Raw materials

Figure 4.1(a) shows the SEM image of the phenolic resin, Durite AD 332A, obtained from Hexion Speciality Chemicals, Inc. and the properties (from datasheet) of the phenolic resin is given in table 4.1. Figure 4.2 shows the DSC curve for phenolic resin. The first endothermic peak (~50^{o}C) corresponds to melting of novolac resin while the second broad peak (~65^{o}C) corresponds to heat of solution of hexamine in the molten resin [92]. The only exothermic peak in the graph represents the cross-linking mechanism of novolac resin and hexamine which occurs around 155°C. Based on the DSC results the part bed temperature was set to be 45^{o}C.

The laser sintered porous parts were prepared from silicon carbide (Washington Mills, <44 μm) and graphite (Ashbury Mills, <70 μm) powders. Figures 4.1(b) and 4.1(c) show the SEM images of graphite and silicon carbide powders, respectively. The properties (from datasheet) of these powders are shown in table 4.2.

[1] The work presented here has been published in International Journal of Precision Engineering and Manufacturing 14 (6), 881-889 and Materials Science and Technology, 2014. This work was supervised by David Bourell.

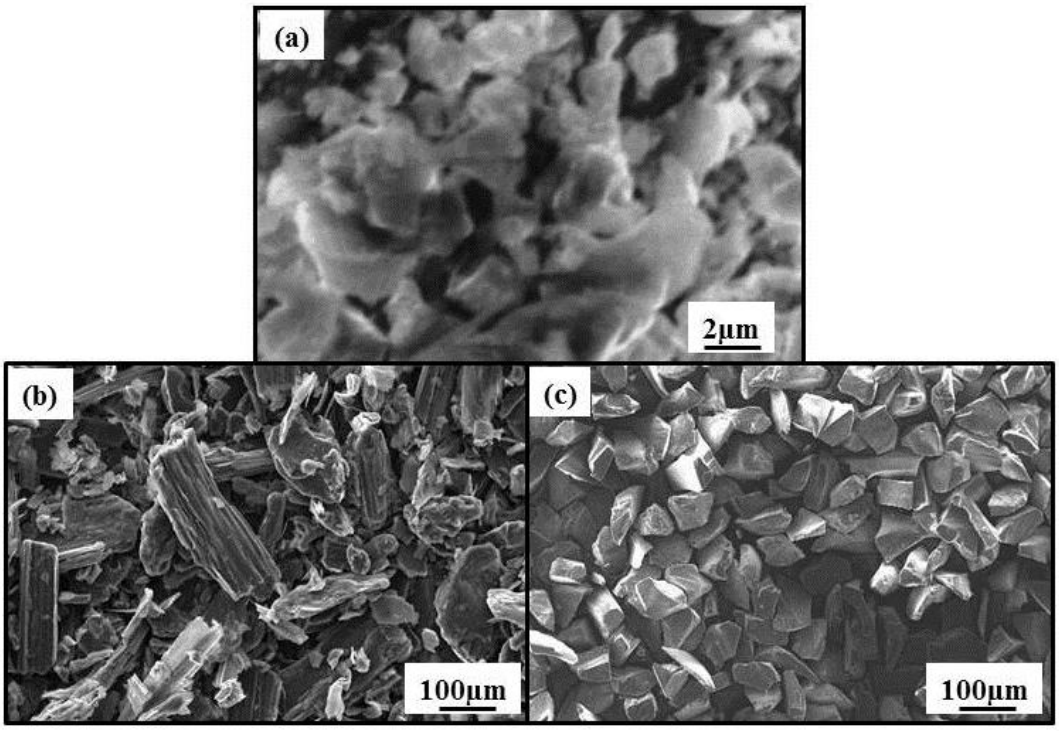

Figure 4.1: SEM images of (a) phenolic resin powder (b) graphite powder (c) silicon carbide powder prior to mixing

Property	Value
Hot plate cure, 150°C	60-90 sec
Hexa Content	9.5-10.5%
Particle Size	98-100% thru 200 mesh
Cost	~$4.85/lb

Table 4.1: Properties of Durite AD 322A (Phenolic Powder)

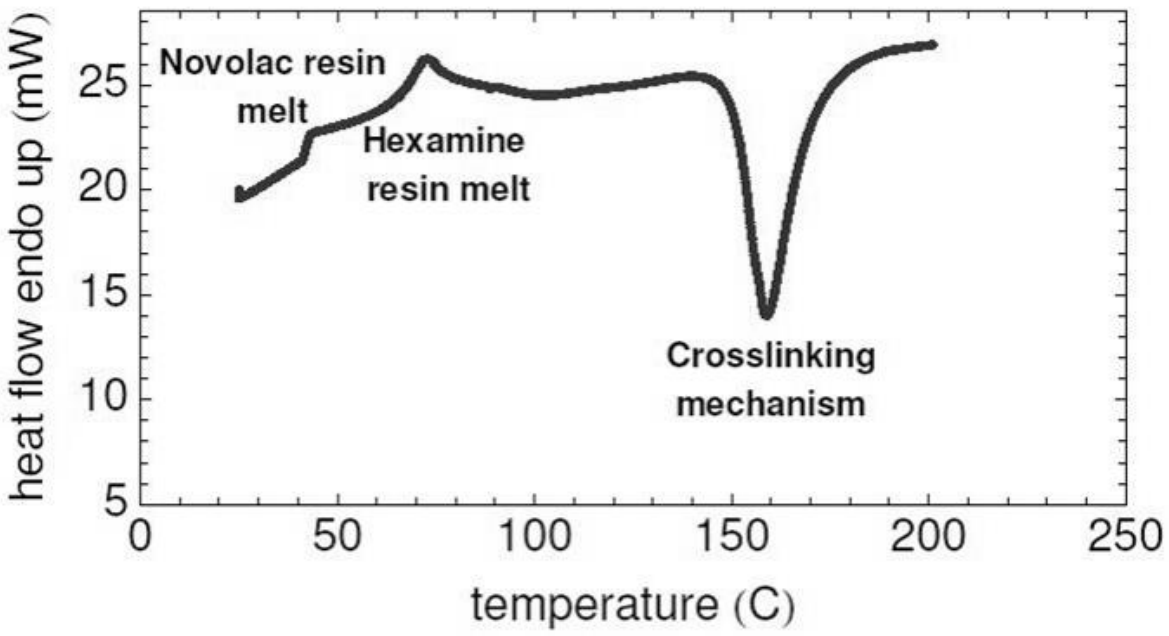

Figure 4.2: Differential Scanning Calorimetry of phenolic resin [93]

Property	Silicon Carbide	Graphite
Specific gravity	3.2	2.25
Particle Size	98-100% thru 120 mesh	(+/-2%) 83% < 75 microns
Cost	~$0.80/lb	~$2.3/lb

Table 4.2: Properties of silicon carbide and graphite powders used to produce laser sintered parts

4.2. Powder preparation

Powder mixing is essential in determining the quality of the SLS parts. Non-uniform mixing of powder can lead to poor green strength in the laser sintered parts. Uniform mixture minimizes the extent of anistropic shrinkage and promotes bonding strength distribution within the parts.

The graphite and silicon carbide powders were mixed separately with phenolic using a roller system as shown in figure 4.3. The material systems were blended in milling jars from US Stoneware with cylindrical alumina pellets (diameter: 0.5 cm) as the grinding media.

Figure 4.3: Roller system used for mixing of the silicon carbide and graphite powders with the phenolic binder

The graphite/phenolic system was mixed in a ratio of 3:1 by weight and the silicon carbide/phenolic system was mixed in a ratio of 10:1 by weight. About 1% carbon fibers by weight were added to the silicon carbide/phenolic system to improve electrical conductivity of the laser sintered parts. The jar was filled one-third with grinding media and one-third with the powder mixture to ensure proper mixing. The powders were mixed at 60 RPM for 24 hours to ensure complete mixing. SEM images of the graphite and silicon carbide powders after mixing with the phenolic binder are shown in figure 4.4. The phenolic powder appears as bright spots in the SEM images due to its poor electrical conductivity and associated charging.

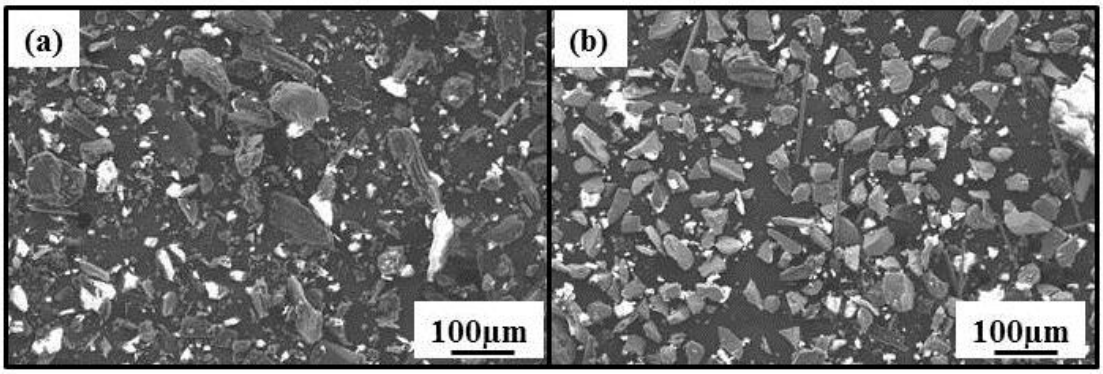

Figure 4.4: SEM images of (a) graphite powder and (b) silicon carbide powder after mixing with phenolic resin

4.3. Fabrication of porous templates using laser sintering

Parameter	Values
Outline laser power	4 W
Scan speed	1.3 m/s
Beam diameter	450 µm
Scan spacing	76.2 µm
Part bed temperature	45°C
Feed Bin temperature	35°C
Part piston temperature	35°C
Part cylinder temperature	35°C
Process gas	Nitrogen

Table 4.3: Laser sintering parameters used in manufacturing of graphite and silicon carbide parts

CAD models required to produce 1 cm x 1 cm x 1 cm cubes were prepared in Solidworks™. The powder was loaded into feed bins and indirect laser sintering was carried out using a DTM Sinterstation® 2000. Table 4.3 shows the common parameters used for selective laser sintering of graphite and silicon carbide. These parameters, except part bed and feed bin temperatures, were set by the material default for Duroform polyamide powder used by the Sinterstation® 2000.

4.3.1. Fabrication of free standing porous parts

Parts were produced using different laser powers and layer thickness to determine the effect of these parameters on the porosity of the final parts. Selective laser sintering was carried at laser powers of 18 W, 25 W and 30 W. The part layer thickness was varied between 0.003 inches to 0.005 inches, which were the limits of the Sinterstation® 2000. The green parts produced in this manner were subjected to temperatures ranging between 300^{o}C to 600^{o}C for 6 hours in order to introduce crosslinking in the phenolic binder and also to partially burnout the binder. The pore volume fraction of these brown parts thus made was determined using the method described in section 4.4.1.

After finding the parameters required for producing parts with a large pore volume fraction, more parts were produced using these parameters. A CAD file was used to produce cuboids with length 5 cm, breadth 5 cm and thickness 3 mm. These parts were the burned out at temperatures ranging between 150^{o}C to 1200^{o}C for 6 hours. The electrical conductivity of these parts was measured using a four point probe method as described in section 4.4.3.

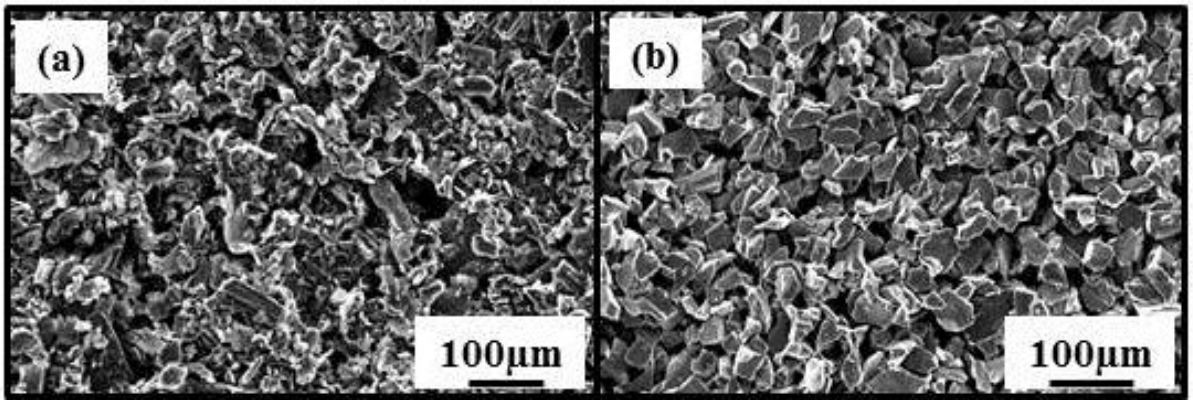

Figure 4.5: SEM images of top surface of a part produced via laser sintering of (a) graphite and (b) silicon carbide

4.3.2. Fabrication of thin parts

A Nylon-11 plate with slots was prepared and used to hold the copper -110 substrates as shown in figure 4.6(a). Figure 4.6(b) shows a picture of a thin porous part laser sintered on copper-110 alloy sheet. The part bin was lowered such that the surface of the copper-110 plate was level with the powder in the feed bins. Indirect laser sintering was performed and very thin parts (1.5 cm x 1.5 cm) were obtained on the substrate. The parameters were chosen such that highly porous parts (~80% porosity) could be obtained. These were determined by the experiments discussed in 0. The thickness of these coating was controlled by the number of layers sintered during the laser sintering process. The laser sintering process was continued until a 200-300 µm thick porous coating was obtained on the copper alloy plate. The samples thus formed were heated in a vacuum furnace at 300^{o}C for 6 hours to induce cross-linking in the phenolic binder and produce brown parts.

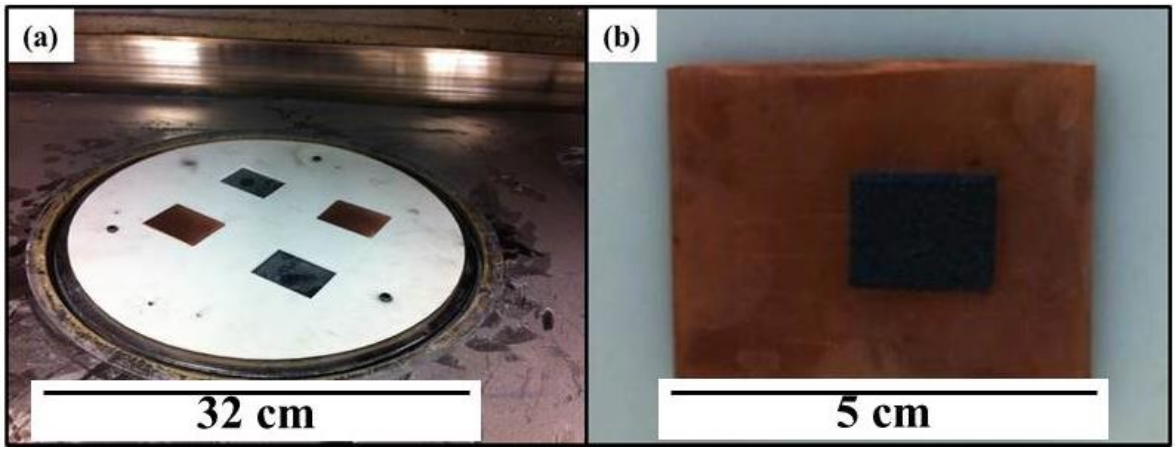

Figure 4.6: Photographs of (a) set up used to produce porous coatings on a copper-110 substrate and (b) a porous SiC coating on a copper-110 substrate

4.3.3. Other materials

Apart from the laser sintered parts, commercially available porous templates such as graphite felt (Sigra Cell™), Nomex® felt (DuPont) and Stainless Steel 316 mesh (McMaster-Carr) were also used in the electrodeposition experiments. The SEM images of these can be found in figure 4.7.

These porous templates were tested along with the laser sintered parts to determine porosity. These materials were chosen due to resistance to chemical attack in highly acidic environments and ease of availability. Hence, these materials do not corrode as a negative potential is applied in the electrochemical cell. Also, these materials are readily available and can be used to show that the application of electrochemical infiltration can be extended beyond laser sintered porous graphite and silicon carbide.

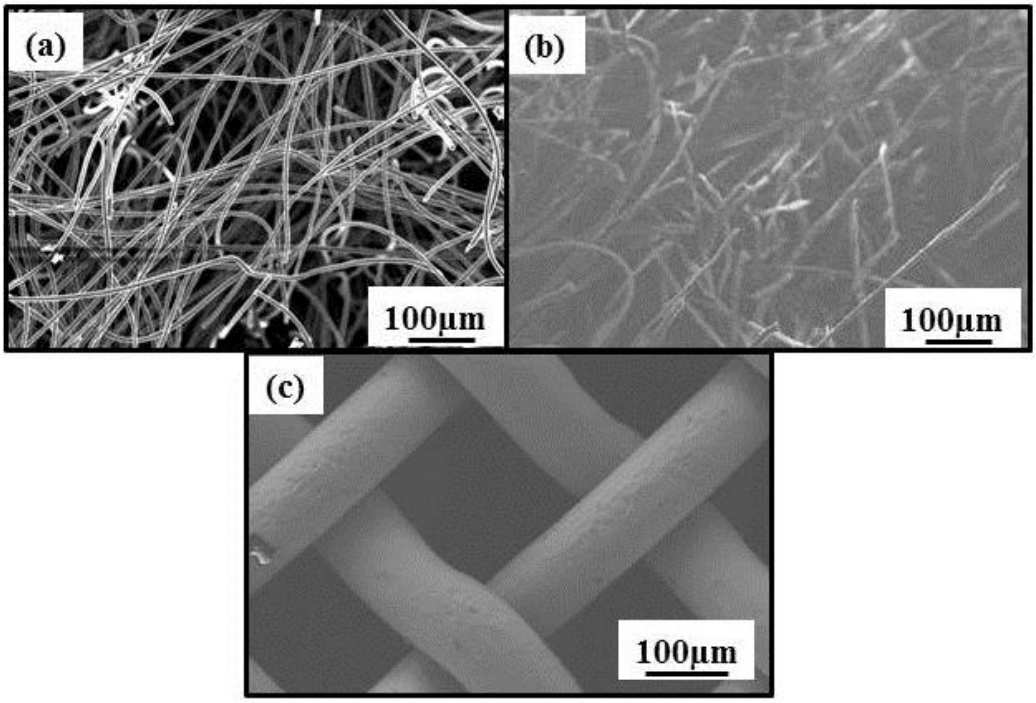

Figure 4.7: SEM images of (a) graphite felt (b) nomex felt (c) stainless steel 316 mesh

4.4. Measurement of properties of laser sintered parts

4.4.1. Density and pore volume fraction

The geometric volume (V_G) of the free standing parts was calculated by measuring the dimensions of the parts using a Vernier caliper. Pychnometry was performed on all the parts using using He gas to measure the apparent volume of the samples [44]. A schematic of a pychnometer is shown in figure 4.8(a) and photograph of instrument is shown in figure 4.8(b). A pychnometer uses the ideal gas law under free isothermal expansion to find the volume of a material. It consists of an empty reference chamber and a specimen chamber where the sample to be measured is stored. In the beginning of the measurement, the gas inlet valve is opened and a reference chamber of known volume is filled with helium until the pressure of the gas in the reference chamber reaches a preset value. As soon as the pressure of the gas reaches this value, a

gas valve between the reference and specimen chamber is opened and the gas is allowed to freely expand into the specimen chamber [94].

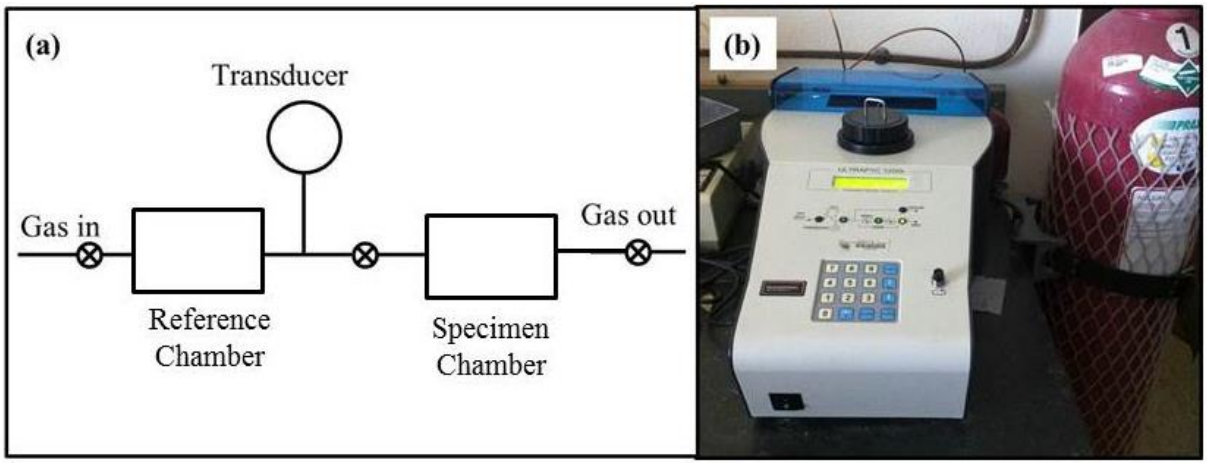

Figure 4.8: (a) A schematic of the circuit used by a pychnometer (b) A photograph of the pycnometer used in this study

The pressure of the gas is recorded again and following equation is used to find the volume of the specimen:

$$V_S = V_R + V_0 - \frac{P_R}{P_F} V_R \qquad (4.1)$$

Here V_S is the volume of the sample, V_R is the volume of the reference chamber, V_0 is the volume of the specimen chamber, P_R is the pressure applied in the reference chamber before the gas valve is opened and P_F is the final pressure obtained after expansion of He into the specimen chamber. The pore volume fraction of the porous parts can be calculated using following:

$$V_P = 1 - \frac{V_S}{V_G} \qquad (4.2)$$

Where V_P is the pore volume fraction and V_G is the geometric volume of the porous parts. This procedure was repeated for all the specimens described in section 0 and 4.3.3.

4.4.2. Pore size measurement

The brown parts produced at different part layer thickness were heated in an oven at a temperature of 120^{o}C for 20 minutes. An epoxy resin and binder were placed in separate containers and heated to a temperature of 120^{o}C for 20 minutes. This reduced the viscosity of the resin and preheated the porous parts to the same temperature to facilitate pressureless infiltration. Hardener was mixed into the epoxy resin in a ratio of 1:2. The laser sintered parts were then dipped into this mixture. This mixture infiltrated the porous laser sintered parts. The parts infiltrated with the epoxy cement were held at a temperature of 120^{o}C for 2 hours to achieve complete curing of the epoxy cement. The epoxy infiltrated parts were mounted and polished using a 1200 grit paper. These were then examined under a scanning electron microscope. This pore size was measured by measuring the distance between the particles. Repeated pore size measurements were made until an average value with less than 50% standard deviation could be obtained. Since the size of the particles is of the order of tens of microns, a standard technique such as BET could not be used because the specific surface areas was observed to be much lower than 10 m^2/g which is required to get accurate measurements.

4.4.3. Electrical conductivity

The electrical conductivity of the laser sintered parts depends on the temperature of binder burnout [49]. Electrical conductivity of the samples was measured using a four point probe method using a customized four point probe with probe spacing, S, of 1.5 mm. The testing was performed according to ASTM C611 specifications and consisted of a Keithley 224 programmable current source. The voltage measurements were made using a HP 3456A digital

voltmeter. The ratio of probe spacing and sample dimensions was used to arrive at the following relation to calculate the electrical conductivity of the parts [95]:

$$\sigma_s = \frac{V}{I} \cdot W \cdot \frac{\pi}{\ln 2} \cdot f\left(\frac{W}{S}\right) \qquad (4.3)$$

where σ_s is the electrical conductivity of the specimen, I is the applied current, V is the potential drop across the probes in the middle, W is the thickness of the sheet on which the measurement is made. $\frac{\pi}{\ln 2}$ is a constant associated with length and breadth of the sample being tested. $f\left(\frac{W}{S}\right)$ is a constant that depends on the thickness and probe spacing and has a value of 0.6336 in this study.

4.5. Electrolyte properties

Aqueous acid copper sulfate electrolytes were used to electrochemically deposit copper into the pore network. The electrolyte used in this study mainly consisted of copper sulfate (Fisher Scientific) and sulfuric acid in deionized water. In addition to these, Triton X-100 was added to the solution to improve the wetting properties of the electrolyte. Various properties of the electrolyte such as contact angle, viscosity and electrical conductivity with varying concentration of the constituents were measured.

4.5.1. Contact angle of the electrolytes with graphite and silicon carbide

It is essential that the electrolyte can access the pore network, so that the electrochemical reaction can take place inside the pores. The porous surfaces are slightly hydrophobic. Hence, an aqueous solution copper sulfate solution is not able to wet these surfaces which make the entire pore network inaccessible to the electrolyte [96, 97]. A wetting agent is needed to improve the

filling of the porosities with the electrolyte. Here Triton X-100 was used since it has been proven to be a good wetting agent for porous surfaces in electrochemical processes [44, 79, 98]. Completely dense graphite and silicon carbide plates (McMaster-Carr) were polished and cleaned with acetone. An contact angle goniometer was used to measure the contact angle of acid copper sulfate solutions containing varying amount of Triton X-100 on these surfaces. Since the plates were not polished to atomic smoothness, some surface roughness was expected and hence the value of contact angle obtained is larger than the actual contact angle [99].

A contact angle goniometer (figure 4.9(a)) consists of dropper system which drops a small volume of a liquid on the flat surface (on the stage) on which the contact angle is to be measured. A light source and a camera are located on either side of the stage. When the light is shined areas of the camera receiving less light appear brighter. A picture of a droplet on a graphite surface is shown in figure 4.9(b). The contact angle can be measured using ImageJ.

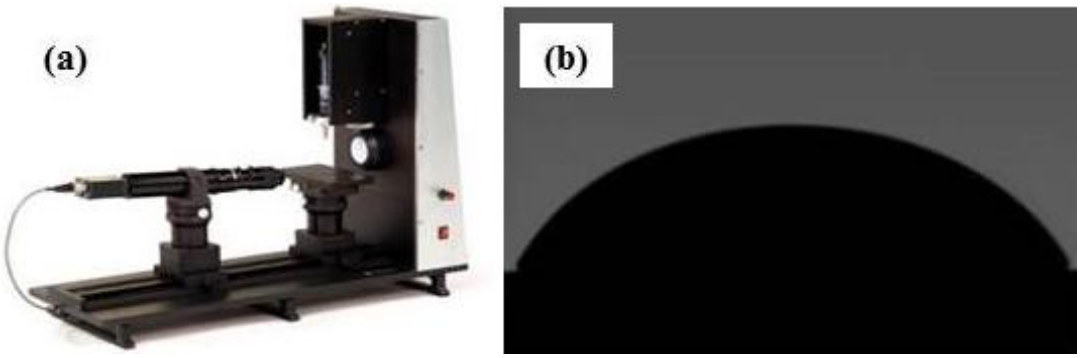

Figure 4.9: (a) A contact angle goniometer (b) An image of 0.1M $CuSO_4$/0.5M H_2SO_4 droplet on a polished graphite surface

4.5.2. Viscosity of the electrolytes

A ball in tube viscometer was used to determine the viscosity of solutions with varying concentration of $CuSO_4$ and H_2SO_4. A glass tube was filled with the solution whose viscosity was to be measured and a glass ball was dropped into to the tube and allowed to fall through the fluid. The terminal velocity of fall of the glass ball was measured and dynamic viscosity was evaluated using following relation [100]:

$$\mu = \frac{2}{9} \cdot \frac{r^2 g(\rho_s - \rho_f)}{v_s} \qquad (4.4)$$

Where μ is the dynamic viscosity, r is the radius of the glass ball and $\rho_s$and ρ_f are the densities of the sphere and fluid respectively, g is the acceleration due to gravity and Vs is the terminal velocity with which the glass ball falls through the fluid.

4.5.3. Electrical conductivity of the electrolyte

Since the specific conductivity of electrolyte is an important factor in uniform distribution of the deposits, the concentration of the $CuSO_4$ and H_2SO_4 was varied so that highly electrically conductive electrolytes were obtained. Electrochemical impedance spectroscopy (EIS) was performed on the various electrolyte compositions using an impedance analyzer connected to an electrochemical interface. EIS is an experimental method of characterizing electrochemical systems that measures the impedance of a system over a range of frequencies of alternating current, and therefore the frequency response of the system. An AC signal of small amplitude is used so that the current potential relation is observed only in the activation controlled region. EIS was plotted in the form of Nyquist plots. While preforming EIS measurements, deposition of copper could take place on graphite electrodes. The data in the Nyquist plots were then used to

find specific conductivity of the solutions using an equivalent RC circuit for a simple electrochemical system [101]. Copper electrodes of surface area 0.0625 cm^2 were placed 6 cm apart and immersed in solutions containing varying contents of $CuSO_4$ (Fisher scientific) and H_2SO_4 to perform the measurements. Since specific conductivity of a solution is dependent only on the concentration of ionic species, use of a different electrode material should not affect its measurement [65]. An AC excitation signal of 10 mV and of 1 MHz-0.1 Hz frequency was applied at the open circuit potential.

4.6. Electrochemical characterization

Electrochemical characterization techniques were used to determine the hydrogen evolution potential, rate constant, symmetry coefficient and diffusion coefficient of the copper ions in the electrolyte. The results from these measurements were used in the calculations of the constants in chapter 3. These results also assisted in determining the electrodeposition parameters. Linear scanning voltammetry, steady state voltammetry and Tafel polarization were performed.

It was assumed that at least one atomic layer of copper is deposited on the internal walls of the pores of the part being infiltrated. Since all electrochemical processes are interfacial reactions it can be assumed that the electrochemical reduction of copper takes place on a copper surface. Hence a copper microelectrode was prepared to perform electrochemical characterization. An insulated copper wire was cut and polished at one of the ends with a circular cross section. This end was shoved into a Tygon® tube and sealed using a silicone sealant. This was required to negate the effects of surface discontinuities on the electrode surface [65]. In this manner several microelectrodes could be prepared for one time use only. These were used in all the electrochemical characterization experiments.

4.6.1. Linear potential scans

A linear potential scan was performed using a conventional three-electrode setup to determine hydrogen evolution potential and to calculate the diffusion coefficient of copper ions in the electrolyte. The copper microelectrode described above was used as cathode and a platinum wire was used as the counter electrode. An $Hg/HgSO_4$ electrode was used as a reference electrode. A linear potential scan was carried out from -0.4 V to -1.4 V at a scan rate of 10 mV/s. The electrolyte used was an aqueous solution of 0.1 M $CuSO_4$. The amount of sulfuric acid was varied from 1 M to 4 M. All the experiments were carried out with 1ml/L Triton X-100 in the solution. This was done because Triton can be expected to shift the activation potential for the reactions by affecting mass transfer of the ions [98, 102].

The current-potential relationship was obtained, and the potential required for copper deposition and hydrogen evolution was identified. This information was used to find the electrical potential window is which copper electrodeposition could be performed with minimal hydrogen evolution. The hydrogen evolution potential and applied potential at the limiting current density were used to set the upper limit for the current applied to perform electrodeposition of copper. Hydrogen evolution leads to formation of bubbles at the cathode which blocks the cathodic sites at which copper reduction reaction can take place [103]. On the other hand, mass transfer limitations occur at limiting current conditions [65]. Hence, these were chosen as the upper limit for the applied potential.

Another set of linear potential scans was carried out using electrolytes with a fixed concentration of sulfuric acid (0.5 M) while varying the quantity of $CuSO_4$ in the solution. The linear potential scans were performed at scan rates of 50 mV/s, 100 mV/s, 150 mV/s, 200 mV/s and 250 mV/s.

4.6.2. Tafel polarization

Tafel polarization was carried out to determine the symmetry coefficient (α) and rate constant k_0. Tafel polarization was performed according to ASTM G59 at a potential scan rate of 0.1667 mV/s. It was performed on solutions containing 0.1 M to 0.5 M $CuSO_4$ and 1 M H_2SO_4.

4.7. Flow through electrolysis

4.7.1. Apparatus

Flow through electrolysis was carried out by flowing the electrolyte parallel to the direction of the applied current. Figure 4.10 shows a schematic of the flow through reactor. A solid current collector could not be placed because it would block the flow of the electrolyte in the flow-through cell. Therefore a higher conductivity in the porous SLS parts was desired so that the electric current could be applied to at a reasonable voltage. Also, it was found that it was impossible to produce unsupported laser sintered parts with thickness less than 2mm. Hence, the laser sintered parts with a thickness of 2 mm and high electrical conductivity were produced. Experiments were carried with porous parts manufactured with laser sintering parameters and graphite felt with properties listed in table 4.4. Copper mesh was placed downstream from the cathode and was used as a counter electrode. This allowed the flow of the electrolyte through the counter electrode.

An electrolyte containing 0.1 M $CuSO_4$ and 4 M H_2SO_4 was used as the electrolyte for the electrodeposition process using the specific conductivity data obtained from EIS measurements and the simulation results discussed in chapter 3. It was stored separately and pumped through

the flow cell using a pump as shown in figure 4.11. A potentiostat was used to apply a current of 30 mA.

A low flow peristaltic pump was used to flow the electrolyte through the porous materials. The flow rate was calculated using a simple relation, such that the residence time of the copper ions inside the pore network could be maximized [65]:

$$v \leq \frac{2A\varepsilon LD}{R^2} \qquad (4.5)$$

where v is the flow rate, ε is the pore volume fraction, A and L are geometric area and thickness of the preform, D is the coefficient of diffusivity for copper ions in the electrolyte and R is the mean pore diameter.

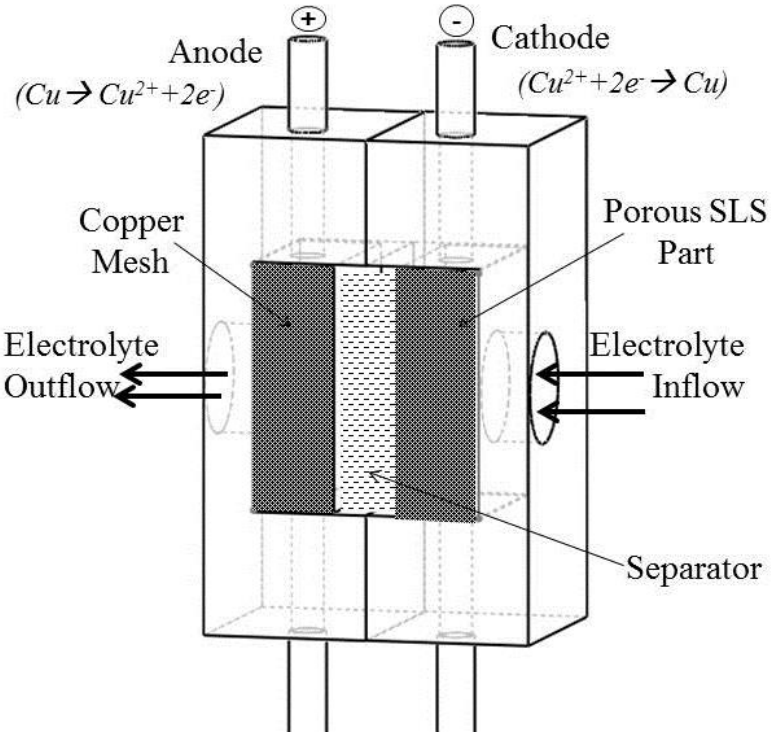

.

Figure 4.10: A schematic of the cross section of the flow through electrodeposition cell

The electrodeposition process was carried out for 10 hours. After completion, deionized water was flowed through the electrodeposition cell for 15 minutes to remove any solution present in the parts. The electrodeposited parts were dried at 120^{o}C for 2 hours and weighed.

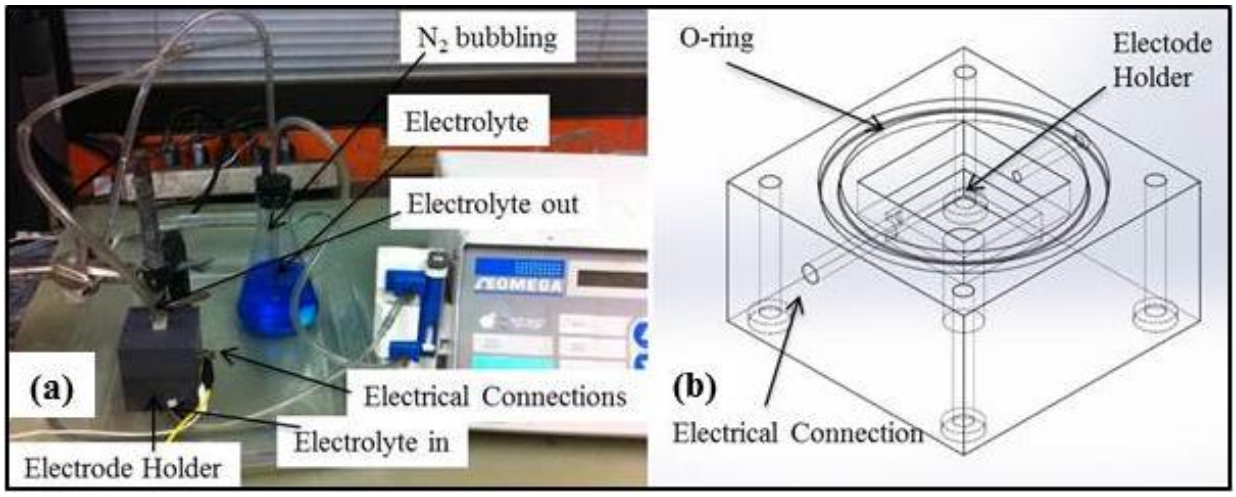

Figure 4.11: (a) A photograph of flow through apparatus (b) A drawing of the electrode holder used in the flow through apparatus

Sample	Laser Power (W)	Layer Thickness (µm)	Conductivity (S/cm)	Porosity %	Average Pore diameter (µm)
Graphite LS1	22	101.6	200 ±15	57 ±1.2	19.03
Graphite LS2	18	127	156 ±31	84 ± 2	27.79
Silicon Carbide	20	152.4	16 ±2	77 ± 2	25.97
Graphite Felt	-	-	1000	96 ±1.8	147

Table 4.4: Properties and manufacturing parameters of the porous materials used for electrolytic infiltration. Laser Sintered parts were burned out at 1200^{o}C

4.7.2. Analysis of the electrolytically infiltrated parts

The copper deposited on the face of the porous parts was removed by carefully grinding the parts on 600 grit paper such that only the copper deposits were removed from the face. Pychnometry was performed again to measure the porosity volume fraction in infiltrated parts. This was then subtracted from porosity of uninfiltrated parts to get the void fraction occupied by copper. The parts were fractured and the fracture surfaces were observed under SEM. EDS maps were obtained for each sample to determine the distribution of copper deposits throughout the porous parts.

4.8. Flow by electrolysis

4.8.1. Apparatus

Figure 4.12 shows a schematic of the flow by reactor. Copper 110 alloy plates were used as current collectors. A platinum foil (anode) was placed on the anodic current collector. Thin porous templates were made on the copper plate (cathodic current collector) using selective laser sintering. A Nafion®-117 membrane was placed between the cathodic and anodic sections. The cell was sealed using Viton sheets.

Electrodeposition was performed using the apparatus shown in figure 4.13. The electrolysis cell was divided into two compartments: anodic and cathodic. The two parts were separated using Nafion® 117, after a standard treatment with H_2O_2 and sulfuric acid [104]. Electrodeposition was performed using the apparatus shown in figure 4.13. The electrolysis cell was divided into two compartments: anodic and cathodic. The two parts were separated using Nafion® 117, after a

standard treatment with H_2O_2 and sulfuric acid [104]. Electrodeposition was performed using an acid sulfate bath containing 0.8 M $CuSO_4$ and 0.2 M H_2SO_4 in DI water.

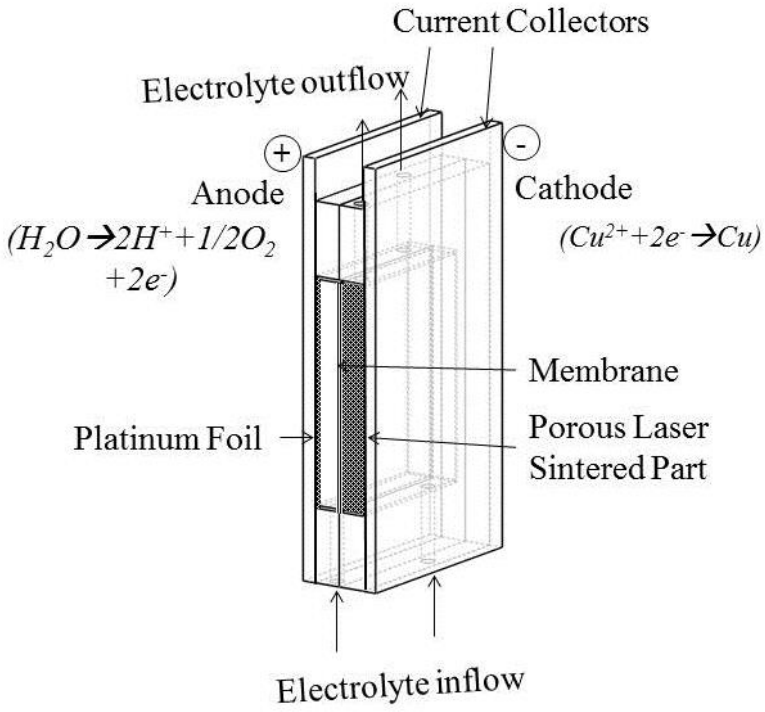

Figure 4.12: A schematic of the cross section of the flow-by electrodeposition cell

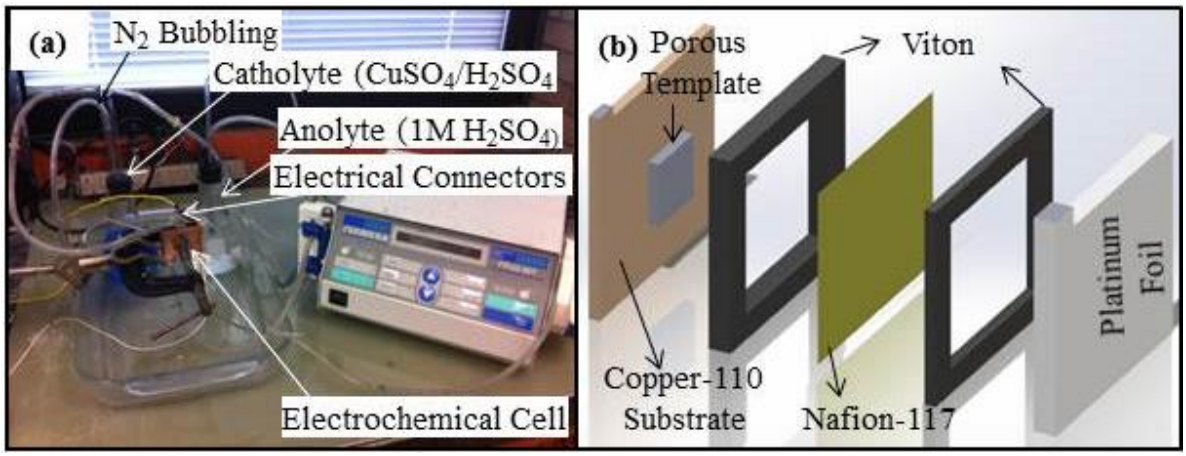

Figure 4.13: (a) A photograph of flow by apparatus (b) A drawing of the electrochemical cell used in the flow through apparatus

Triton X-100 was added as a surfactant to improve the wettability of the porous parts with the electrolyte. In a previous study [44], as presented in chapter 5, it was found that 1 ml/L of Triton X-100 is the optimum concentration for impregnation of the porous parts with the electrolyte. Consequently, 1 ml/L of Triton X-100 was added to the electrolyte. The electrolyte was flowed perpendicular to the direction of applied current using a peristaltic pump.

The laser sintered porous parts were manufactured with a layer thickness of 0.15 mm at a laser power of 18 W. The thickness of the parts was controlled by the number of layers sintered to give an approximate thickness of 0.5 mm. Apart from the laser sintered parts, Nomex® felt and stainless steel mesh described in 4.3.3 were also infiltrated electrochemically.

Initial experiments were carried out with the same electrolyte in the both anodic and cathodic compartments with a copper anode. It was realized that due to uncontrolled dissolution of the anode, copper particles that were attracted towards the cathode would stick to the membrane and block the pores of the membrane. Therefore, the solution in the anodic compartment was changed to 1 M H_2SO_4, and a platinum anode was used. Oxygen evolution was carried out on the counter electrode. Separate reservoirs were used to store the acid sulfate bath (catholyte) and the sulfuric acid solution (anolyte). The catholyte and anolyte were separately flowed through the cathodic and anodic sections respectively at the same flow rate. The sulfuric acid solution in the anolyte also provided better conductivity because hydrogen ions, due to their smaller size, can cross over to the cathodic side easily [105].

4.8.2. Diffusion of Cu^{2+} across Nafion®

Since Nafion is a cation exchange membrane, it allows copper ions to cross over to the anodic side. This can cause a drop in concentration of copper ions in the catholyte because a copper -

deficient solution is used as the anolyte. Since the concentration of copper ions is an important parameter for electrodeposition, it was required that the change in concentration of copper ions due to diffusion across the Nafion membrane is quantified. This was done by flowing the catholyte on one side of the membrane and the anolyte on the other side in the electrolysis cell without applying any potential. The concentration of copper ions in the anolyte was measured using an absorption spectroscope. The effect of flow rate and surfactant on Cu^{2+} cross-over was determined. The following relation was used to calculate the mass transfer coefficient of the Cu^{2+} ions to quantify the cross-over rate [106]:

$$m = \frac{V \times C_A}{A \times t \times \Delta C_{CA}} \qquad (4.6)$$

Here, *m* is the mass transfer coefficient in cm/s, V is the volume of the solution in the anodic section in cm^3, C_A is the concentration in the anodic section in mol/cm^3, A is the area of the membrane available for mass transfer in cm^2, t is the total time taken in seconds and ΔC_c is the concentration difference between the cathodic and anodic sections in mol/cm^3.

4.8.3. Electrodeposition parameters

Electrolytic deposition was performed under constant potential. The minimum reduction potential of an element is dependent on the ionization energy of the outer shell electrons and is independent of the concentration [107]. Since the concentration the Cu^{2+} ions in the catholyte can change over time, a galvanostatic process would require application of higher potentials to maintain the same current. Depending on the actual concentration of copper in the catholyte, the applied electric potential can increase to the reduction potential of hydrogen ions. Hence, to avoid any side reactions such as H_2 evolution, potentiostatic deposition is preferred.

Copper was deposited inside the porous templates by applying initial total currents of 50 mA, 100 mA, 150 mA and 200 mA using a potentiostat. The potential at which these currents were achieved were kept constant throughout the duration of electrodeposition. With time a small decrease in the applied current was observed. The current-time plots were recorded and the total time, T, required for electrodeposition was calculated using Faraday's law:

$$V_p \times \rho_{Cu} = M_{Cu} \times \frac{I \times T}{n \times F} \qquad (4.7)$$

Here, V_p is the pore volume fraction of the porous part supported by the current collector, ρ_{Cu} is the density of copper, M_{Cu} is the molar mass of copper, n is the number of electrons required to reduce Cu^{2+} ions and F is the Faraday's constant. I is the applied current and is assumed to be constant throughout the duration of electrodeposition.

4.8.4. Analysis of the electrolytically infiltrated parts

The electrodeposited samples were washed under running water. These were sectioned and polished using standard metallography sample preparation for copper which included grinding using 400 and 600 grit paper and consecutive polishing steps using 6 µm, 1 µm and 0.5 µm alumina particles on a polishing pad. The polished specimens were etched with a solution containing 25% NH_4OH, 20% H_2O_2 (3%) in deionized water to reveal the microstructure of the electrodeposited copper. Optical microscopy was performed, and grain size was measured from the intercept method using image processing software.

A separate set of samples was prepared to observe X-ray diffraction patterns of the samples thus formed. X-ray diffraction was performed with Cu(Kα) radiation between 40^o and 80^o. The scan rate was 5^o/s.

A set of porous coatings were prepared using a copper foil as a substrate. This was done to fabricate “free standing coatings”. The copper foil was ground away, and the total volume of the free standing coatings was measured using a pychnometer. These free standing coatings were then weighed and the pore volume fraction in the coatings was found using the following relation:

$$V_{pc} = \frac{M}{V \times \rho_t} \qquad (4.8)$$

Where, V_{pc} is the pore volume fraction. M and V are the mass and volume of the free standing coating. ρ_t is theoretical density of the coating free of porosities and was calculated using rule of mixtures.

4.8.5. Thermal properties

The thermal conductivity of the free standing coatings can be found using the following relation [10]:

$$k = \frac{\alpha \times C_p \times M}{V} \qquad (4.9)$$

Here, k is the thermal conductivity, α is the thermal diffusivity and C_p is the specific heat at constant pressure, M is the mass and V is the volume of the sample.

The free standing coatings described in 4.8.4 were cut into 8 mm x 8mm square samples which were used to measure thermal diffusivity, α, using a laser flash method in a laser flash analyzer at 50^{o}C, 100^{o}C, 150^{o}C and 200^{o}C. The samples were spray coated with graphite prior to the measurement to obtain maximum absorption of the laser on the surface.

Specific heat was measured using differential scanning calorimetry. It was performed using a Shimadzu DTG-60A thermal analyzer. The samples were heated from 40^{o}C to 200^{o}C in nitrogen

atmosphere. An α-Al_2O_3 crystal was used as a reference and the ratio method suggested by O'Neill was used to calculate C_p of each sample using the following relation [108]:

$$\frac{C_p}{C_p'} = \frac{m' \times y}{m \times y'} \qquad (4.10)$$

Here, C_p' is the specific heat of the reference. m and m' are the masses of the sample and the reference, respectively. y and y' are the ordinate variations of the sample and the reference from the baseline at the same temperature. These ordinate variations can be measured directly from heat flow rate into the sample.

4.8.6. Tribology

Wear rate of the coatings was measured using a linear reciprocating sliding pin on plate type contact. Copper matrix composite coatings produced by electrodeposition of copper at 50 mA were used for tribological studies. An alumina ball (3 mm diameter) was used to make contact with the samples and was used as the abrasive for a wear track length of 10 mm. A normal load of 5 N was applied. The wear measurements were carried out at three different sliding speeds: 1200, 1800 and 2400 mm/min for a total sliding distance of 500 m. The length of the wear tracks was 10 mm. The dynamic coefficient of friction for the surfaces in contact was recorded during each experiment as the ratio of tangential force (F_T) and normal load (F_N). After the completion of the test, the samples were analyzed using an optical profilometer to measure the depth of the wear tracks.

This information was used to calculate the volume of the wear tracks using volume of the segmented cylinder [109].

$$V_{WT} = L\left[R^2 \cos^{-1}\left(\frac{R - h}{R} \right) - (R - h)\sqrt{2Rh - h^2} \right] \qquad (4.11)$$

Where, V_{WT} is the volume of the wear track, L is the length of the wear track, R is the radius of the alumina ball used and h is the depth of the wear track.

Three sliding tests were performed on each sample before calculating the volumetric wear rate. The wear tracks were further analyzed using scanning electron microscopy to understand the mechanism of wear.

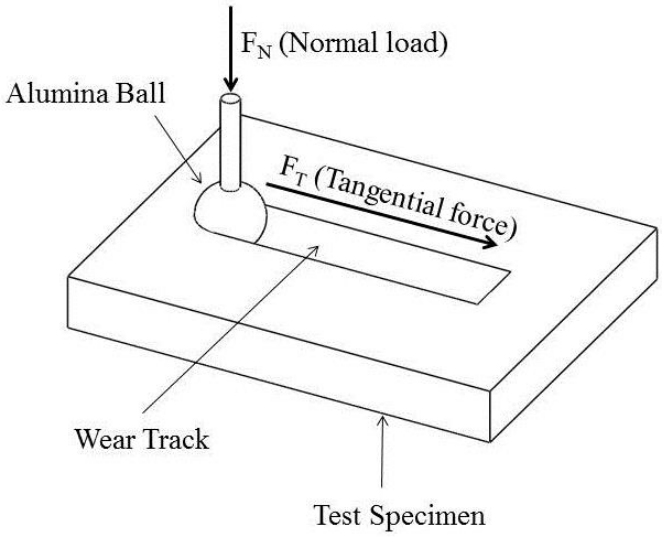

Figure 4.14: A schematic of the operation of a tribometer

Chapter 5: Results[1]

5.1. Porosity measurement

Porosity of the brown parts produced using different laser sintering parameters was measured using a He pycnometer. Table 5.1 shows the porosity measurements for laser sintered graphite brown parts and table 5.2 shows the porosity measurements for laser sintered silicon carbide brown parts. The pore volume fraction increased with both the increase in burnout temperature as well as the increase in layer thickness.

Laser Power (W)	Burnout Temperature (^{o}C)	Layer Thickness (μm)	Porosity (%)
18	600	101.6	61
25	600	101.6	57
30	600	101.6	59
18	300	101.6	61
18	400	101.6	63
18	500	101.6	59
18	300	76.2	54
18	300	127	78

Table 5.1: Porosity of graphite parts produced by laser sintering after binder burnout

[1] The work presented here has been published in International Journal of Precision Engineering and Manufacturing 14 (6), 881-889 and Materials Science and Technology, 2014. This work was supervised by David Bourell.

Laser Power (W)	Burnout Temperature (^{o}C)	Layer Thickness (μm)	Porosity(%)
18	600	101.6	57
25	600	101.6	56
30	600	101.6	59
18	300	101.6	58
18	400	101.6	56
18	500	101.6	58
18	300	76.2	51
18	300	127	73

Table 5.2: Porosity of silicon carbide parts produced by laser sintering after binder burnout

However it was observed that the layer thickness has a more pronounced effect on the pore volume fraction as compared to the burnout temperature. As the layer thickness is increased the volumetric energy density of the laser scanning the part bed decreases and hence results in poorer density of the green part [110].

5.2. Pore size measurement

The pore volume fraction was varied by changing the layer thickness and the parts were burnt out at a temperature of 300^{o}C. These were subsequently infiltrated with a curable epoxy resin. Pore size measurement was performed by observing epoxy infiltrated laser sintered graphite and silicon carbide under a scanning electron microscope. The SEM images of the epoxy infiltrated graphite and silicon carbide are shown in figures 5.1 and 5.2, respectively. Individual particles of silicon carbide and graphite can be seen in the SEM images. Pore size of the porous parts produced via selective laser sintering was measured using an image processing software by

measuring the distance between the individual particles. The pore diameter of the laser sintered parts is tabulated in table 5.3.

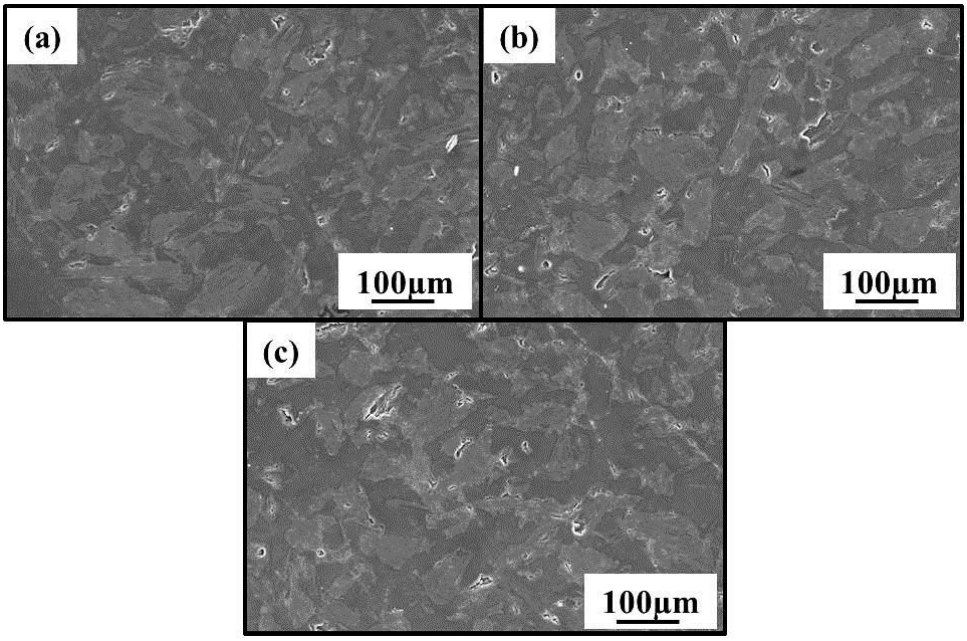

Figure 5.1: SEM images of epoxy infiltrated laser sintered graphite produced at powder layer thickness of (a) 0.005 µm (b) 0.004 µm and (c) 0.003 µm

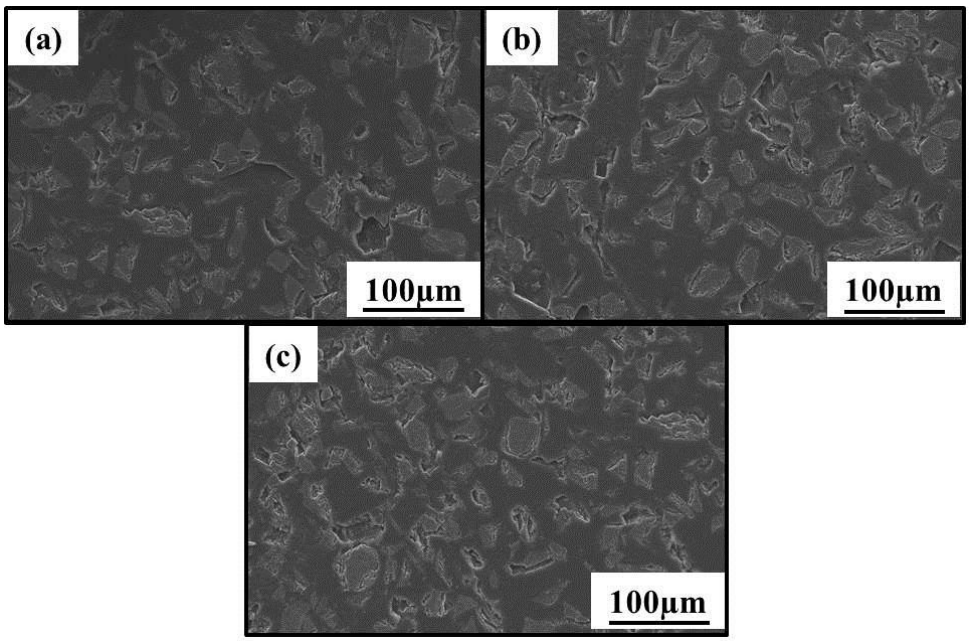

Figure 5.2: SEM images of epoxy infiltrated laser sintered silicon carbide parts produced at powder layer thickness of (a) 0.005 µm (b) 0.004 µm (c) 0.003 µm

Layer Thickness (in)	Pore Diameter (µm)	
	Graphite	Silicon Carbide
0.003	39.03±8.1	28.7±13
0.004	45.8±21	34.8±11
0.005	49.62±23	42.1±19

Table 5.3: Average pore diameter of graphite and silicon carbide parts produced via laser sintering after burnout at 300^{o}C

5.3. Electrical Conductivity

Burnout Temperature (^oC)	Electrical Conductivity (S/cm)	
	Graphite	Silicon Carbide
150	25	2
200	27	3
300	26	3
400	31	5
500	41	6
600	39	8
1200	200	16

Table 5.4: Electrical conductivity of laser sintered parts manufactured at powder layer thickness of 0.005 μm.

The electrical conductivity is shown as a function of binder burnout temperature is shown in table 5.4. The electrical conductivity showed very small improvement over the binder burnout temperatures ranging from 300^{o}C–600^{o}C.

5.4. Viscosity and contact angle

Figure 5.3 shows a plot of viscosity of $CuSO_4/H_2SO_4$ solutions with the concentration of $CuSO_4$ and H_2SO_4. It was observed that the addition of both copper sulfate and sulfuric acid lead to an increase in the viscosity of the solutions. Figure 5.4 shows a plot of viscosity of 0.1M $CuSO_4$/4M H_2SO_4 and 0.8M $CuSO_4$/4M H_2SO_4 with quantity of Triton X-100. It was found that the increase in the concentration of Triton X-100 in the solutions lead to an increase in the viscosity of the

solutions. Figure 5.5 shows the change in contact angle of the 0.1M $CuSO_4$/4M H_2SO_4 solution with graphite and silicon carbide with the amount of surfactant in the solution. It was observed that the contact angle of the solution with the graphite surface decreased with the addition of the surfactant from 60^o to 22.5^o as the concentration of Triton X-100 was increased from 0 ml/L to 1 ml/L. Similarly, a decrease of the contact angle with the silicon carbide surface from 58^o to 22^o was observed. It was also noticed that there was a negligible change in the contact angle as the concentration of the surfactant was increased beyond 1ml/L. It should be noted that the surfaces used for contact angle measurements in this study were not atomically smooth. Hence, the contact angle reported here is higher than the contact angle measured on an atomically smooth surface [97].

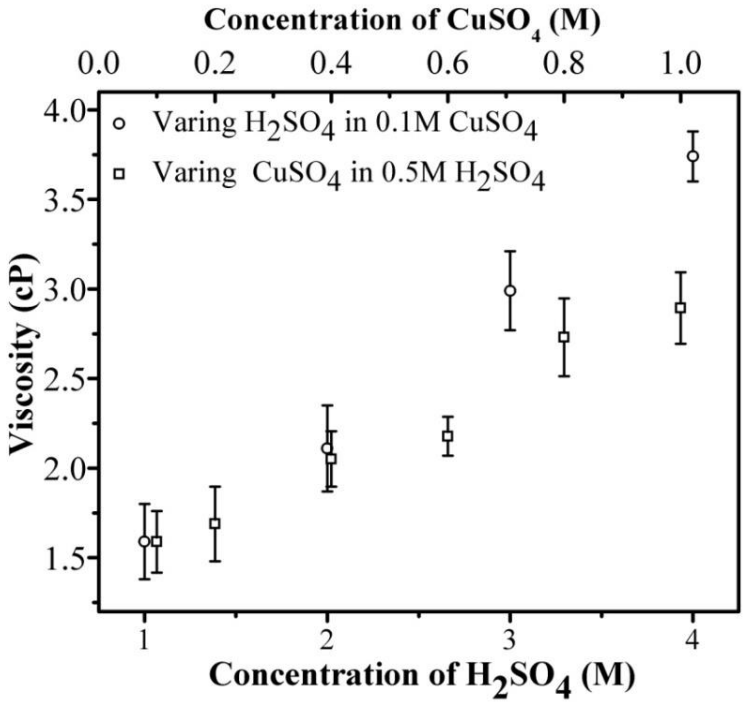

Figure 5.3: Viscosity of $CuSO_4$/H_2SO_4 electrolytes with change in the concentration of $CuSO_4$ and H_2SO_4

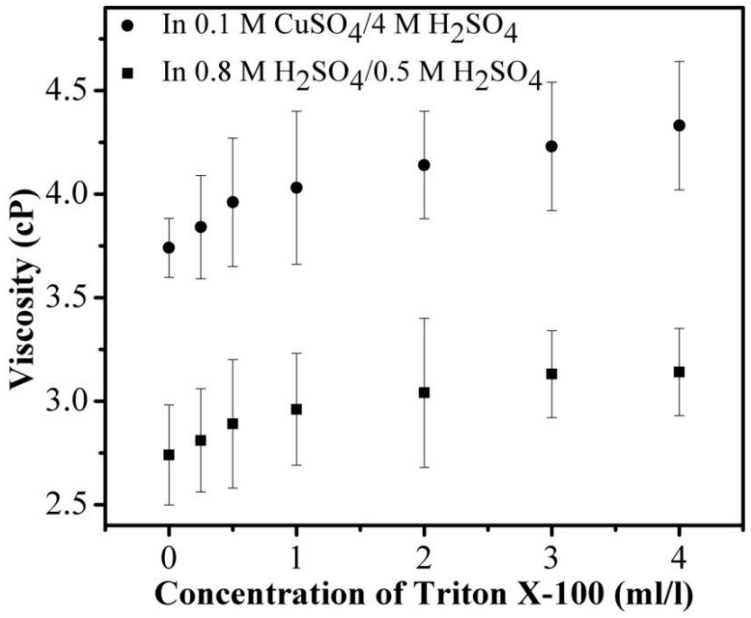

Figure 5.4: Viscosity of $CuSO_4/H_2SO_4$ electrolytes with addition of Triton X-100

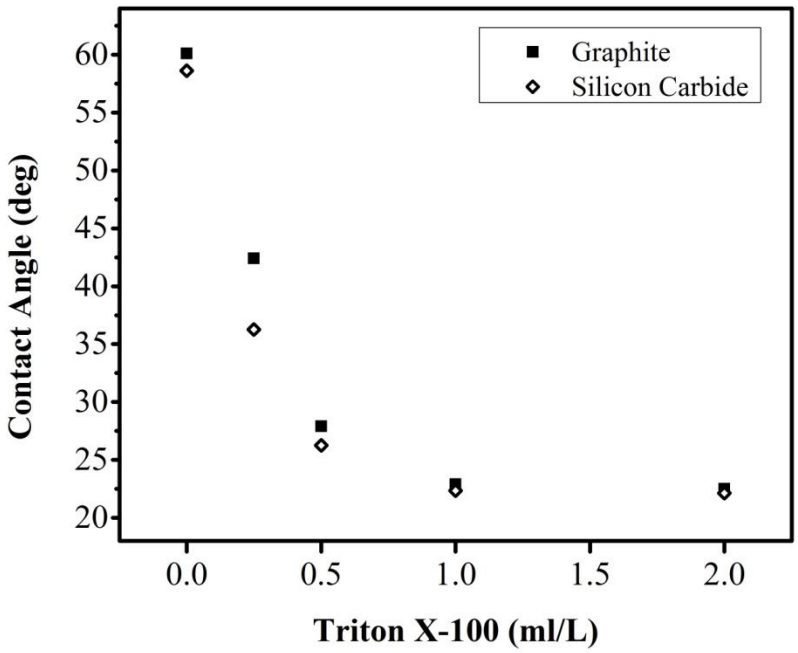

Figure 5.5: Contact angle of 0.1 M $CuSO_4$/4 M H_2SO_4 solutions with graphite and silicon carbide after 10 seconds

5.5. Electrical conductivity of the electrolytes

Figures 5.6 and 5.7 show the Nyquist plots obtained using electrochemical impedance spectroscopy performed using an alternating current with frequency ranging from 1 MHz to 0.1 Hz and amplitude of 10 mV. The Nyquist plots obtained here are distorted semicircles. This distortion has been attributed to inductive behavior of electrochemical systems [111]. Some workers have related this inductive behavior to the formation of a surface layer, like a passive layer or fouling [101]. Others have claimed that inductive behavior results from errors in the measurement, including potentiostat non-idealities [65]. In this case, passivating coating is formed on copper due to formation of an oxide layer on it when comes in contact with the acidic electrolytes used in this study [101].

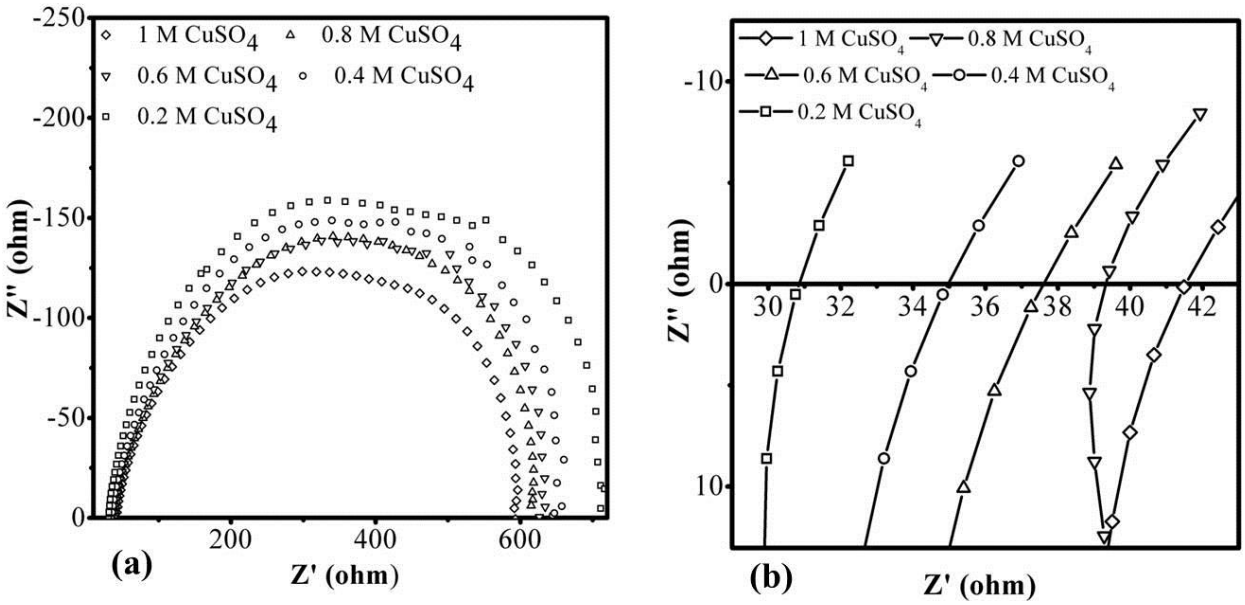

Figure 5.6: (a) Nyquist plots obtained electrolytes with varying concentration of $CuSO_4$ in 1 M H_2SO_4 solution (b) Point of intersection of Nyquist plots shown in (a) with real impedance axis at low AC frequency

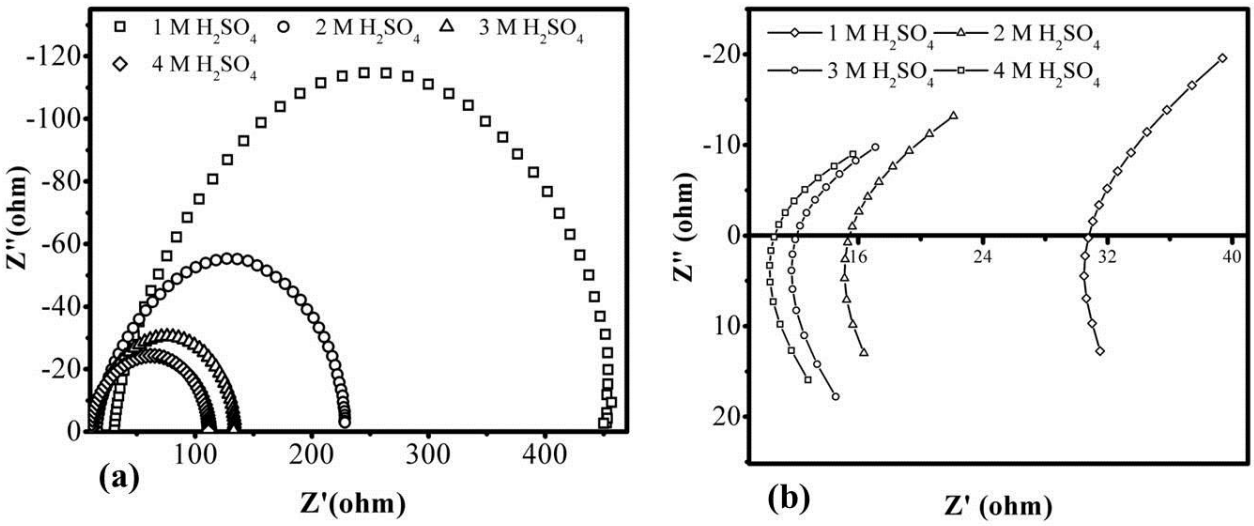

Figure 5.7: (a) Nyquist plots obtained electrolytes with varying concentration of H_2SO_4 in 0.1 M $CuSO_4$ solution (b) Point of intersection of Nyquist plots shown in (a) with real impedance axis at low AC frequency

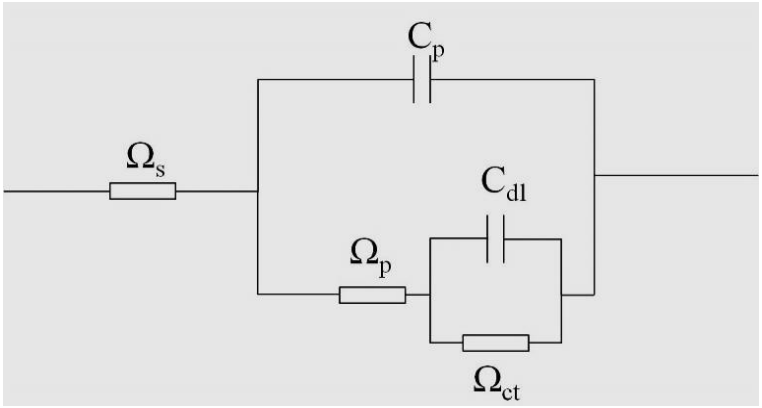

Figure 5.8: RC circuit used to fit the data in the Nyquist plots in figure 5.6 and 5.7

The RC circuit shown in figure 5.8 can be used to fit the data for an electrochemical system comprising of copper electrodes immersed in $CuSO_4/H_2SO_4$ solutions. The circuit consists of solution resistance Ω_s, polarization resistance Ω_p, double layer capacitance C_{dl}, capacitance of a passive coating C_p and charge resistance due to the passive coating [101]. The impedance response of a capacitor depends on the frequency and the impedance of a resistor is constant. At

very high frequencies the impedance of the capacitor, C_{dl}, becomes very small compared to the impedance of the resistors Ω_p and Ω_s. Since C_{dl} is in parallel with Ω_p, Ω_{ct} and C_p it acts as a short and effectively removes them from the circuit. Hence the impedance response is dependent only on solution resistance.

5.6. Electrochemical characterization

5.6.1. Linear potential scan

Figure 5.9 shows the current potential relations obtained as a result of linear potential scans performed on 0.1 M $CuSO_4$ solution with varying concentration of H_2SO_4 and 1 ml/l Triton X-100. The potential scan was performed at a scan rate of 10 mV/s.

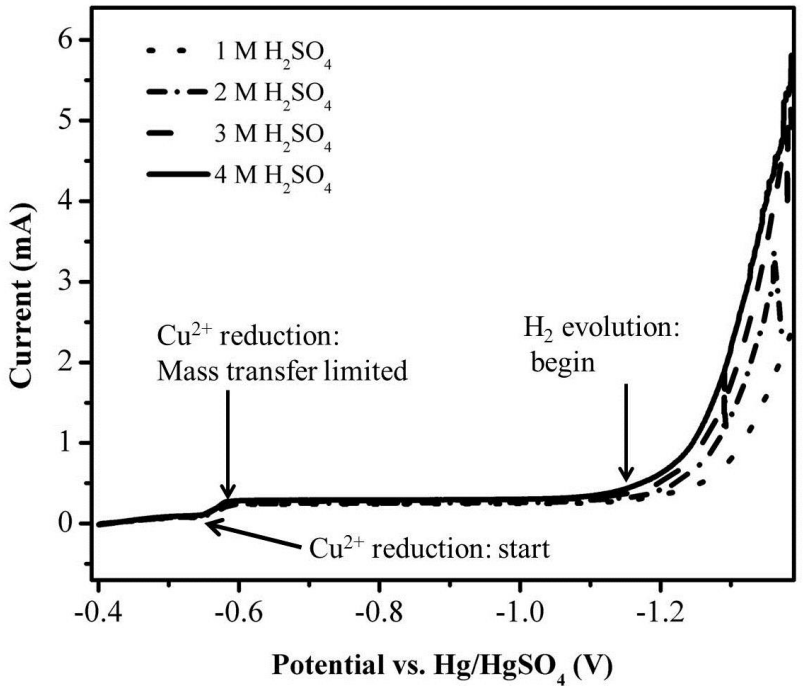

Figure 5.9: Current-Potential curves obtained via linear potential scans (10 mV/s) on 0.1 M $CuSO_4$ solutions with varying H_2SO_4 concentration

In all the cases, the mass transfer controlled Cu^{2+} reduction started close to -550 mV with respect to a $Hg/HgSO_4$ reference electrode. The current obtained as a result of copper reduction increased as the applied potential was increased and reached its mass transfer limited value at a potential of -590 mV.

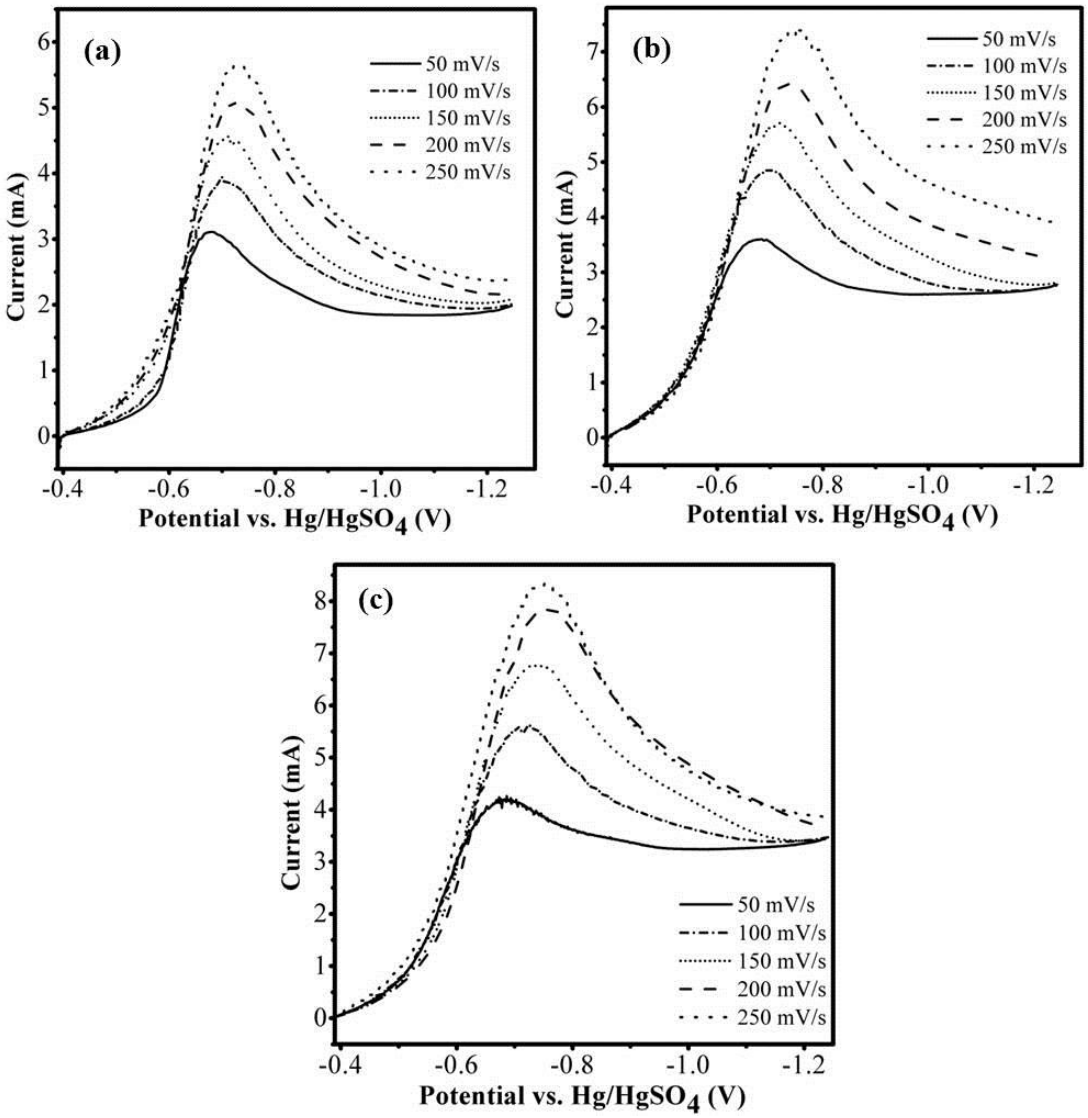

Figure 5.10: Current-Potential curves obtained via linear potential scans on (a) 0.3 M $CuSO_4$ (b) 0.4 M $CuSO_4$ and (c) 0.5 M $CuSO_4$ in 0.5 M H_2SO_4 solution at different potential scan rates.

H_2 evolution began only when the applied potential was higher than -1 V vs. the $Hg/HgSO_4$ reference. Although the potential for H_2 evolution did not change with the increase in the concentration of H^+ ions in the solution, the current obtained as a result of H^+ reduction increased with the increase in the concentration of H^+ ions. Hence H_2 evolution can only occur at very high potential when compared to the reduction of copper. A suitable potential can be chosen such that copper can be electrodeposited with high current efficiency in highly acidic solutions. The distance between beginning of Cu^{2+} reduction and H_2 evolution also provide a range of potentials suitable for electrodepositing copper without producing hydrogen.

Current-potential curves obtained via linear potential scans on 0.3 M $CuSO_4$, 0.4 M $CuSO_4$ and 0.5 M $CuSO_4$ in 1 M H_2SO_4 solution with 1 ml/l Triton X-100 are shown in figure 5.10. The scan rate of the potential was changed and the behavior of the peak current was observed. It was noticed that the peak current shifted to the right as the potential scan rate was increased. It was also observed that the peak current increased as the concentration of copper ions in the solution was increased due to a larger number of copper ions available for the reduction reaction.

The current-potential curves obtained here were used to calculate the diffusion coefficient of copper ions in the presence of Triton X-100, which acts as a suppressant in acid copper sulfate solutions, using the following relation [65]:

$$i_p = (2.99 \times 10^5)\alpha^{1/2} A C_0^* D_0^{1/2} v^{1/2} \qquad (5.1)$$

Where, i_p is the peak current, α is the charge transfer coefficient, A is the area of the electrode, C_0^* is the bulk concentration of the copper ions in the electrolyte, D_0 is the diffusion coefficient of the copper ions and v is the potential scan rate.

5.6.2. Tafel polarization

Figure 5.11 shows Tafel plots obtain via potential scans carried out on 0.1 M $CuSO_4$ to 0.5 M $CuSO_4$ solution in 1 M H_2SO_4 with 1ml/l Triton X-100. The potential was plotted against Log(I). In general an increase in Log(I), was observed with the increase in the concentration of copper sulfate in the solution.

The y-intercept of the slope of Tafel plot was used to find exchange current, i_0, which was subsequently used to calculate the symmetry factor, α and rate constant k_0. Although the rate constant and symmetry factor have been reported in literature before, a suitable value for these in presence of a surfactant were not found. Because of the polar nature of the surfactant molecules, they can form bonds with the ions in the solution due to dipole interactions. Hence the surfactant can act as a complexing agent and reduce the rate of reaction [65].

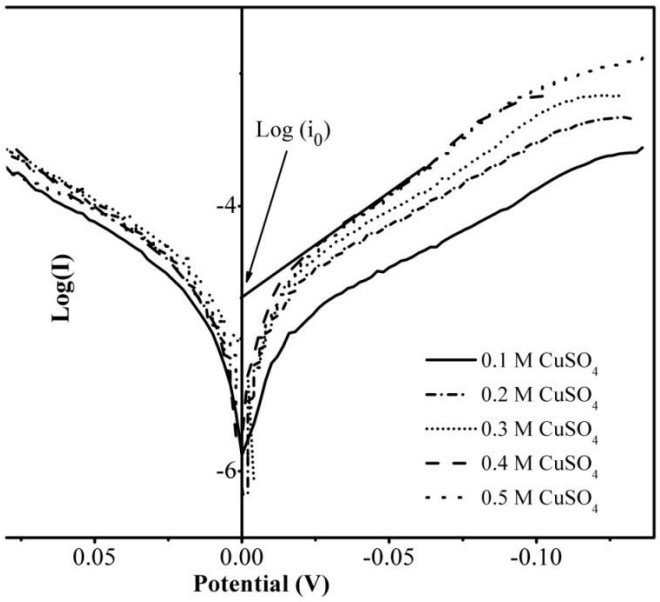

Figure 5.11: Tafel plots of 0.1 M to 0.5 M $CuSO_4$ in 0.5 M H_2SO_4 with 1ml/l Triton X-100

The exchange current is related to the bulk concentration and rate constant via the following equation [65]:

$$i_0 = FAk_0 C_0^{1-\alpha} C_R^{\alpha} \qquad (5.2)$$

Where, i_0 is the exchange current and C_R is the concentration of reduced species in the solution. Here, the reduced species is solid copper and hence, $C_R = 1$.

5.7. Electrodeposition of copper into free standing porous parts

A solution containing 0.1 M $CuSO_4$ and 4 M H_2SO_4 in deionized water was used as electrolyte. The electrolyte contained 0.1% Triton X-100 by volume. 30 PPM of HCl was added as chloride ions are known to be adsorbed strongly on copper plated surfaces and provides a charge transfer site which is slightly catalytic in nature. Chloride ions are also known to enhance the formation of an anode film which aids in proper dissolution of the anode [112]. The flow rate of the electrolyte was estimated at 6 ml/min using equation (2.5).

Figure 5.12 shows the plot of current applied by the potentiostat vs time. It can be observed that the applied current showed negligible change during the duration of electrodeposition due to the flow of electrolyte through the porous specimens.

Figure 5.14 shows EDS element maps of the fractured surface of the porous parts after infiltration. It can be seen that copper is deposited inside the porosities over the length of the porous parts. The element maps in all cases confirm the presence of copper and its uniform distribution over the entire thickness of the preforms. Table 5.5 shows the porosity of the porous parts electrodeposited with copper. It was found that the graphite LS2 samples were more filled compared to LS SiC and graphite LS1. In case of graphite felt, almost 26% porosity volume

fraction was filled with copper. This is because of the difference of the pore size as well as the porosity volume fraction.

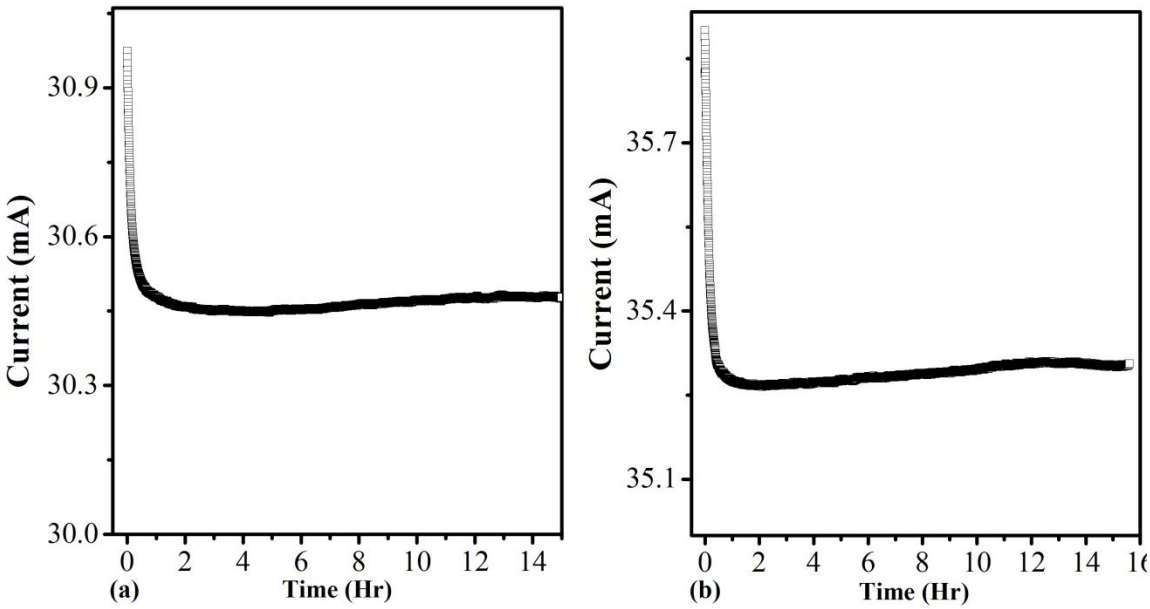

Figure 5.12: Current vs. time plots obtained during flow electrodeposition of copper on (a) laser sintered graphite-1 and (b) laser sintered silicon carbide for applied current of 30mA

Figure 5.13 shows SEM images of the cross section of the porous parts electrodeposited with copper in the flow electrolysis cell. It was observed that it was possible to deposit copper inside the pore network.

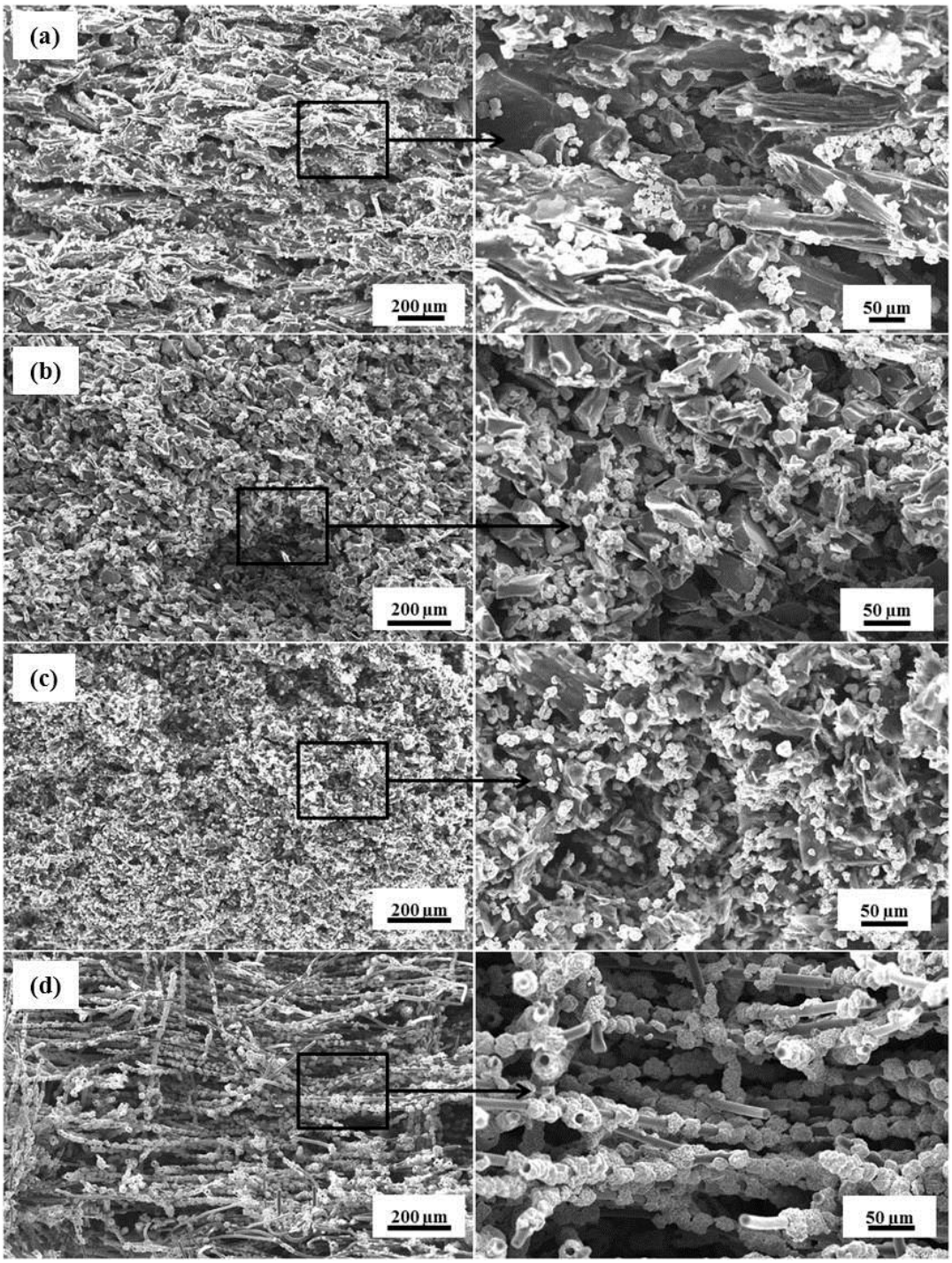

Figure 5.13: SEM images showing copper distribution in the fractured porous parts (a) Graphite LS1 (b) SiC (c) Graphite LS2 and (d) graphite felt

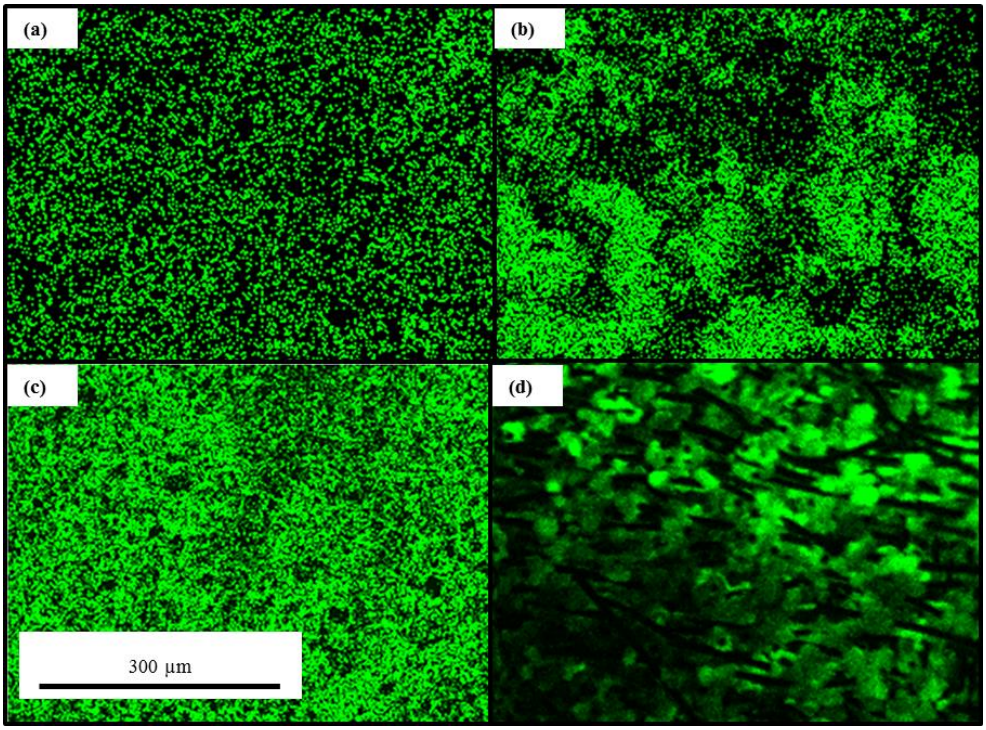

Figure 5.14: EDS element maps showing copper distribution in the fractured porous parts (a) Graphite LS1 (b) LS SiC (c) Graphite LS2 and (d) graphite felt after electrolytic deposition with copper.

Sample	Porosity fraction of electrodeposited parts	Porosity fraction occupied by copper
Graphite 1	49%	8.00%
Graphite 2	69.6%	14.40%
Silicon Carbide	61.2%	6.40%
Graphite Felt	70%	26.00%

Table 5.5: Porosity volume fraction of porous parts after electrodeposition with copper

5.8. Electrodeposition of copper into porous coatings on copper-110 alloy

Figure 5.15 shows current versus time plots obtained during electrodeposition of copper into laser sintered graphite and silicon carbide on a copper-110 alloy substrate for an applied current of 200mA. It was observed that the current stayed constant during the electrodeposition process. Due to the flow of the electrolyte in the electrolysis cell, the copper ions responsible for the flow of current are replenished near the electrode surface, thus giving a constant current. It can also be observed that more fluctuation was observed in the applied current when compared to figure 5.12. Here, the applied current is very high compared to that during flow through electrolysis and results in larger loss of reactants near the electrode surface. The non-laminar flow of the electrolyte leads to vigorous mixing of the electrolyte and can cause small fluctuations in the applied current [33].

Figure 5.16(a) and (b) show a photo and SEM of cross section of graphite felt that was electrolytically infiltrated with copper. It was observed that the graphite felt was not completely infiltrated with copper at applied current of 30 mA. Figure 5.17 shows a photo of a copper matrix composite coating formed by electrolytic infiltration of copper into laser sintered graphite at electrodeposition current of 200 mA. It was observed that at applied current higher than 200 mA poor coatings with very high porosity for all the porous material used for electrodeposition were obtained.

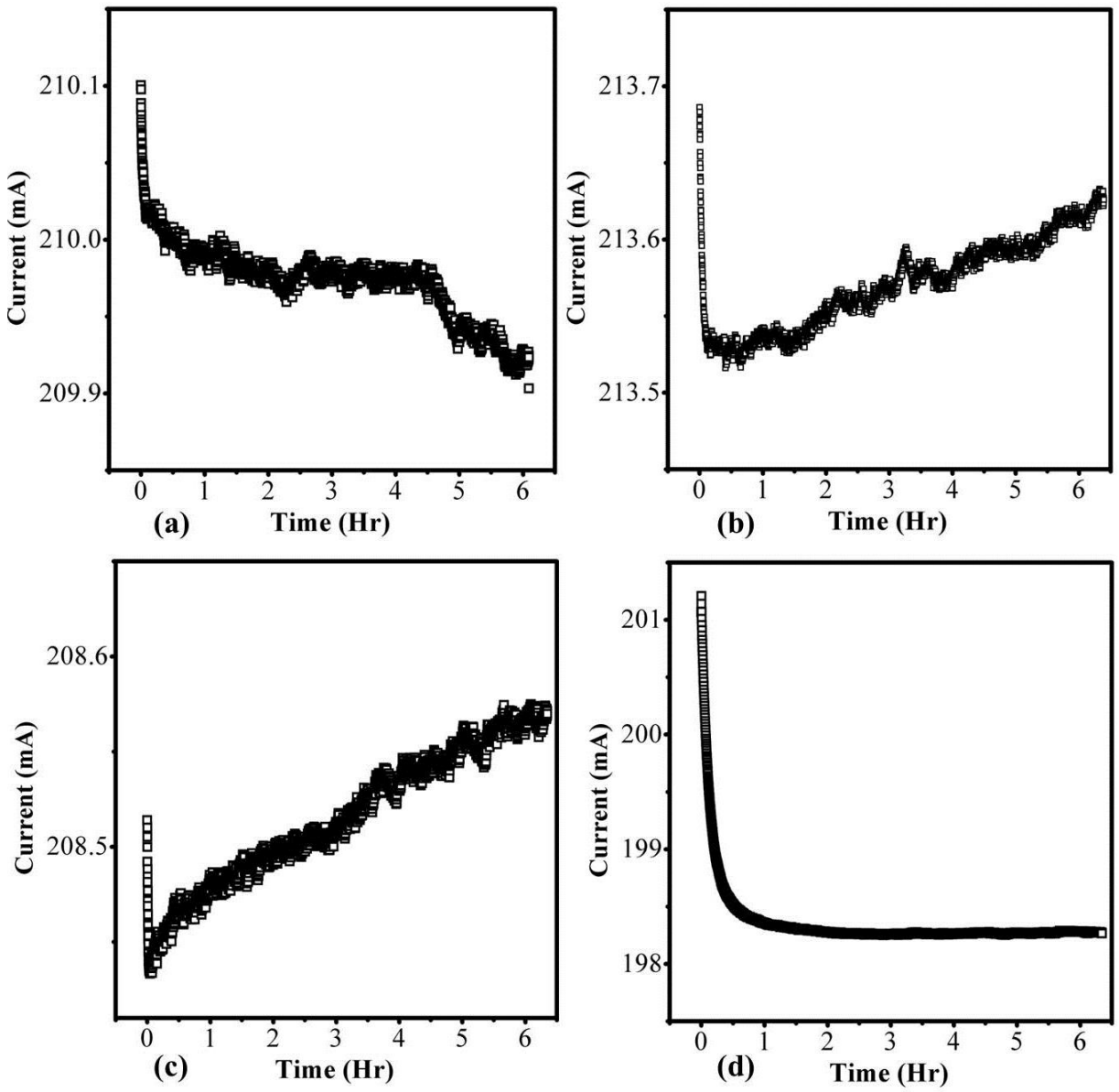

Figure 5.15: Current vs. time plots obtained during flow electrodeposition of copper on (a) & (b) laser sintered graphite and (c) & (d) silicon carbide for applied current of 200 mA in different experiments

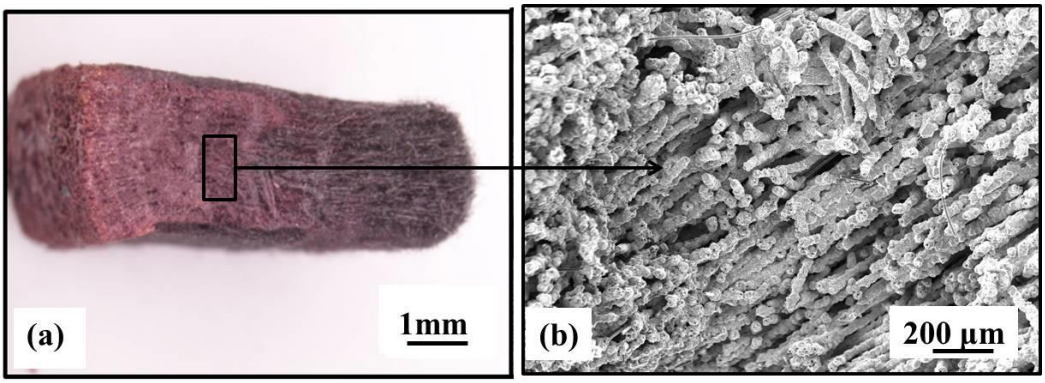

Figure 5.16: (a) Copper infiltrated graphite felt (b) SEM image of the infiltrated felt

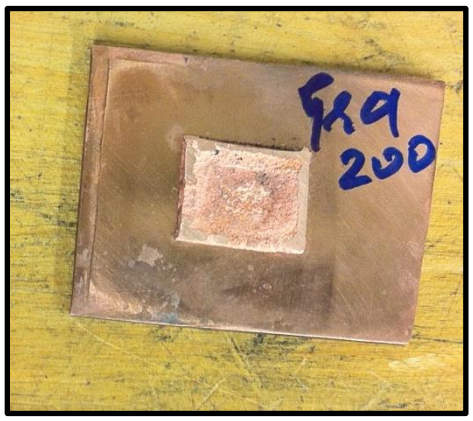

Figure 5.17: A photograph of a copper-graphite composite coating just after electrolytic infiltration of a graphite porous template with copper

5.8.1. Absorption spectroscopy

Figure 5.18 shows the intensity of visible light transmitted through the anolyte after 5 hours of the operation of the flow cell without application of any external potential. As the flow rate was increased, the transmittivity of visible wavelength greater than 650nm increased through the catholyte.

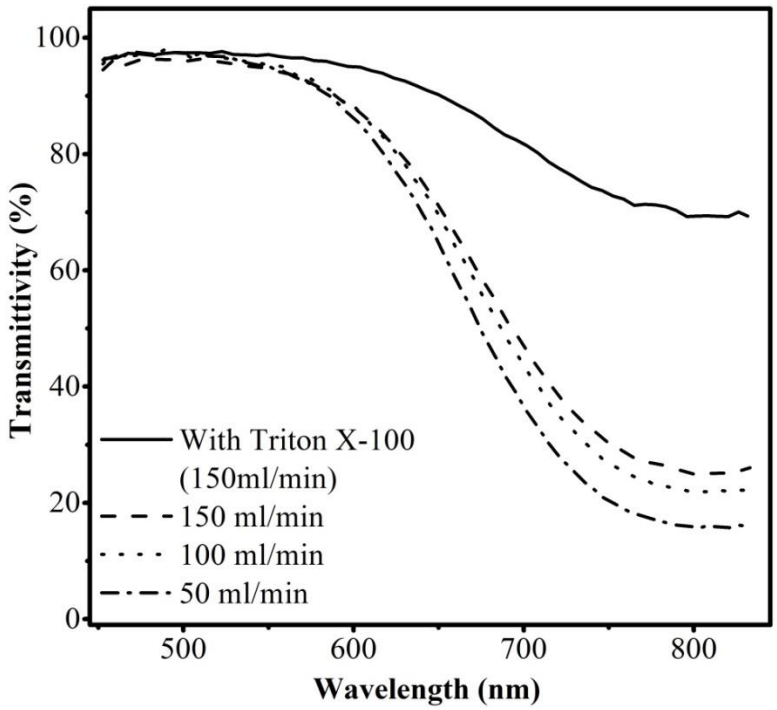

Figure 5.18: Transmittivity of anolyte in the anodic half-cell after 5 hours for different flow rates of catholyte and anolyte

The copper ions from the catholyte diffuse into the anolyte due to the chemical potential created by the difference in concentration of ions on either side of the membrane. Copper sulfate solutions are blue in color, and the aqueous solution of copper absorbs visible radiation with a wavelength more than 650nm.

The mass transfer rate of copper was measured by measuring concentration of copper ions in the anolyte under different flow conditions. In the beginning, the anolyte was an aqueous solution of 1 M H_2SO_4 and the catholyte was an aqueous solution of 0.8 M $CuSO_4$ and 0.5 M H_2SO_4. Since the anolyte is completely transparent, visible radiation at all wavelengths are expected to be transmitted completely through the anolyte. As the catholyte and anolyte were flowed in the respective sections, the copper ions diffused into the anolyte. Thus the concentration of copper in

the anolyte increased with time. An experiment was carried out using catholyte containing 0.8 M $CuSO_4$, 0.5 M H_2SO_4 and 1 ml/L of Triton X-100 at a flow rate of 150 ml/min. In these particular experiments the flow cell was run without application of any external potential. The transmittivity of the radiation of interest through the anolyte was slightly higher when the rate of flow of the electrolytes was lower. More interestingly, with the addition of Triton X-100, the transmittivity of the 650nm radiation through the anolyte became significantly higher.

To further investigate these observations, a set of experiments was carried out in which the transmittivity of visible radiation was recorded after the flow cell was operated with any external potential for 5, 10, 15, 20 and 25 hours for electrolyte flow rate of 150 ml/min. The experiments were carried out using catholytes with and without the surfactant. The corresponding plots between transmittivity and wavelength for these are shown in figure 5.19. The Beer-Lambert law was used to find the concentration of the Cu^{2+} ions in the anolyte using the following equation:

$$T = \exp(-A_m bC) \qquad (5.3)$$

Where, T is the percentage transmittance, A_m is the molar absorptivity of copper sulfate in aqueous solution and is equal to 20 $Lmol^{-1}cm^{-1}$ and C is the concentration of the copper ions.

The corresponding plot of concentration of copper ions in the catholyte for different flow conditions is shown in figure 5.20. It can be observed that the presence of the surfactant in the catholyte leads to a reduction of the copper ions in the catholyte. Using this observation, it was concluded that the presence of the surfactant in the electrolyte improves the wetting of the porous electrode with the electrolyte as well as reduces the mass transfer of the copper ions through the Nafion® membrane.

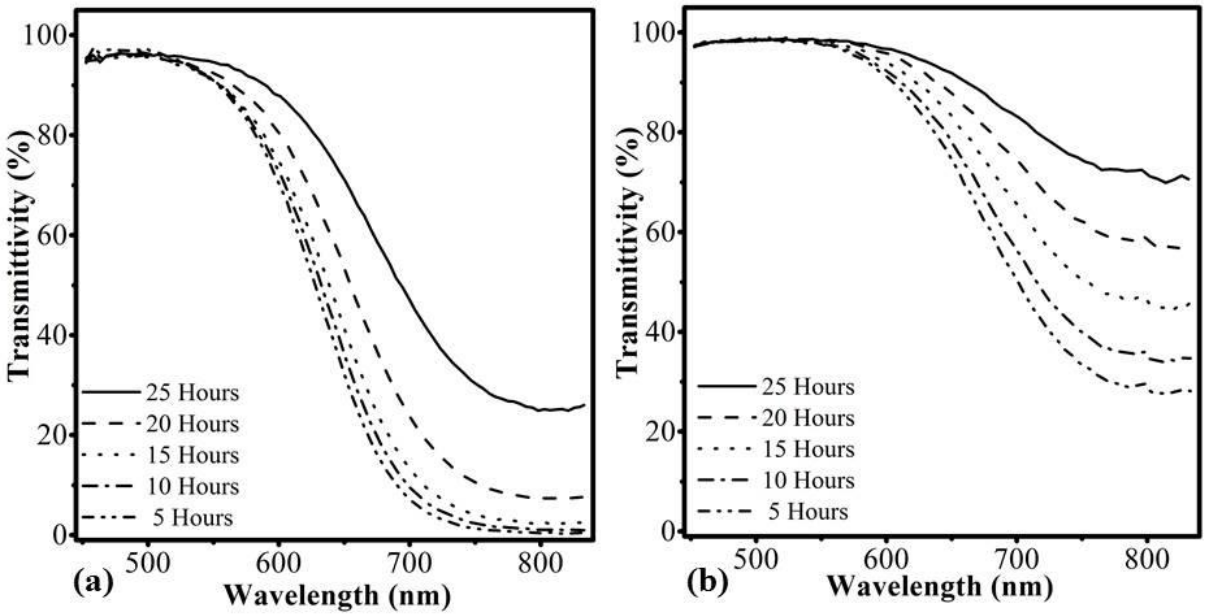

Figure 5.19: Transmittivity of anolyte in the anodic half-cell at various time intervals for catholyte with (a) without Triton X-100 (b) with Triton X-100 for a flow rate of 150ml/min

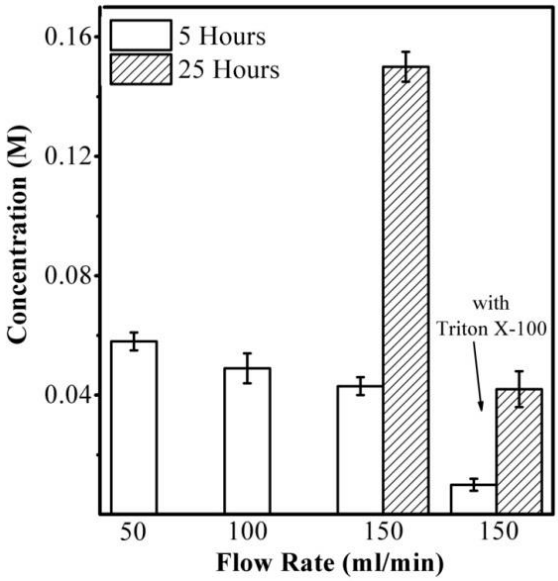

Figure 5.20: Concentration of copper ions in the anolyte as calculated by Beer-Lambert Law

5.8.2. Microstructure and X-ray diffraction

Figures 5.21 and 5.22 show scanning electron microscopy images of polished top surfaces and cross-sections of the deposited composite coatings obtained via electrolytic infiltration into the porous media. It was difficult to obtain good contrast between stainless steel and copper in the copper-SS coatings and a backscattered electron detector was used to obtain images shown in figure 5.22(c) and (d). Figures 5.23-5.26 show microstructures of composite coatings obtained after electrolytic infiltration of copper into porous media. The microstructure of the electrodeposited copper consisted of equiaxed grains of copper. It was realized that as the grain size of electrodeposited copper decreased as the applied potential was increased.

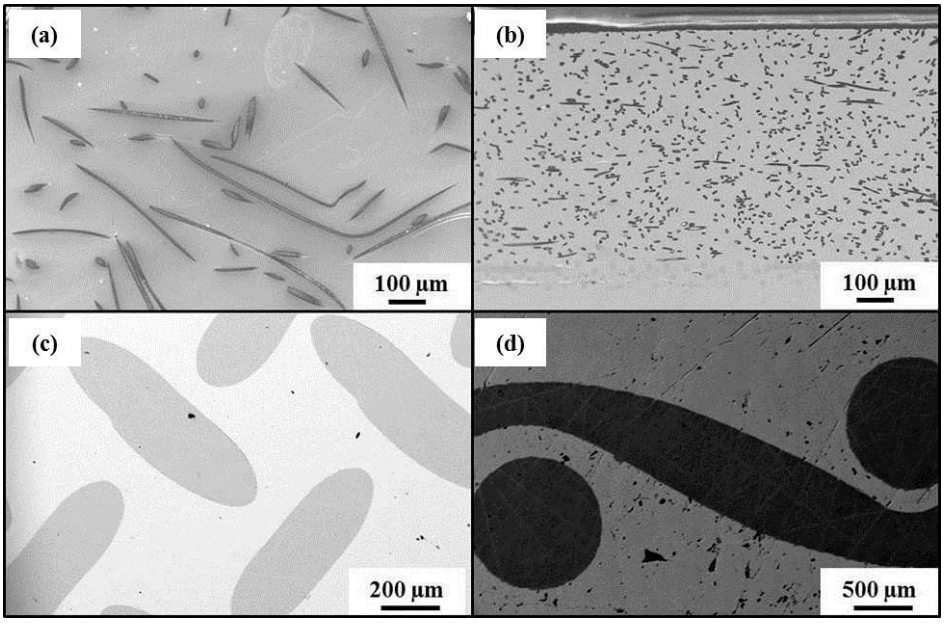

Figure 5.21: Secondary electron images of (a) top surface (b) cross-section of copper-nomex coatings. Backscattered electron images of (c) top surface (d) cross-section of copper-SS coatings

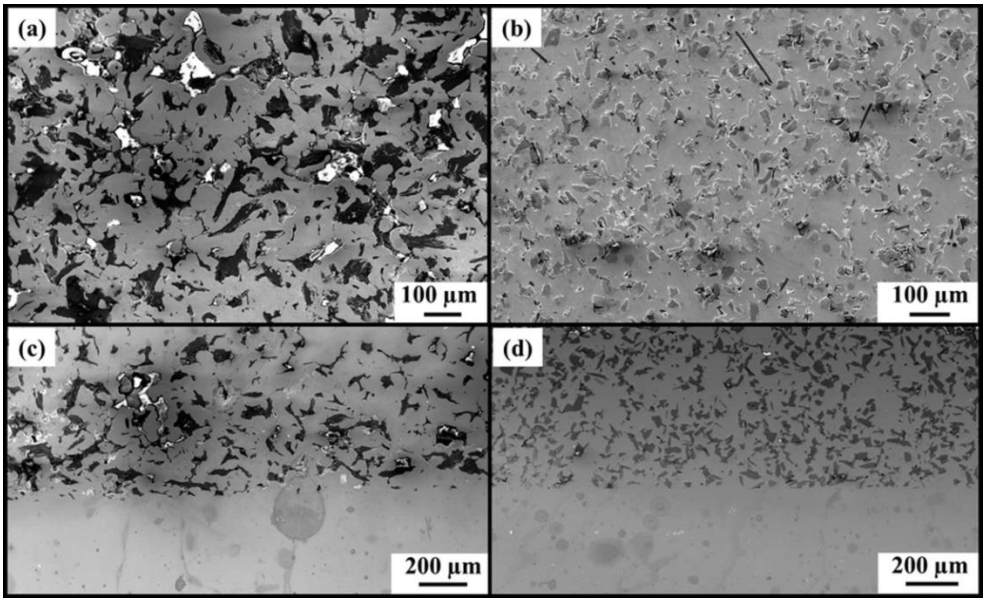

Figure 5.22: Secondary electron images of top surface of (a) copper-graphite (b) copper-SiC and cross-section of (c) copper-graphite (d) copper-SiC

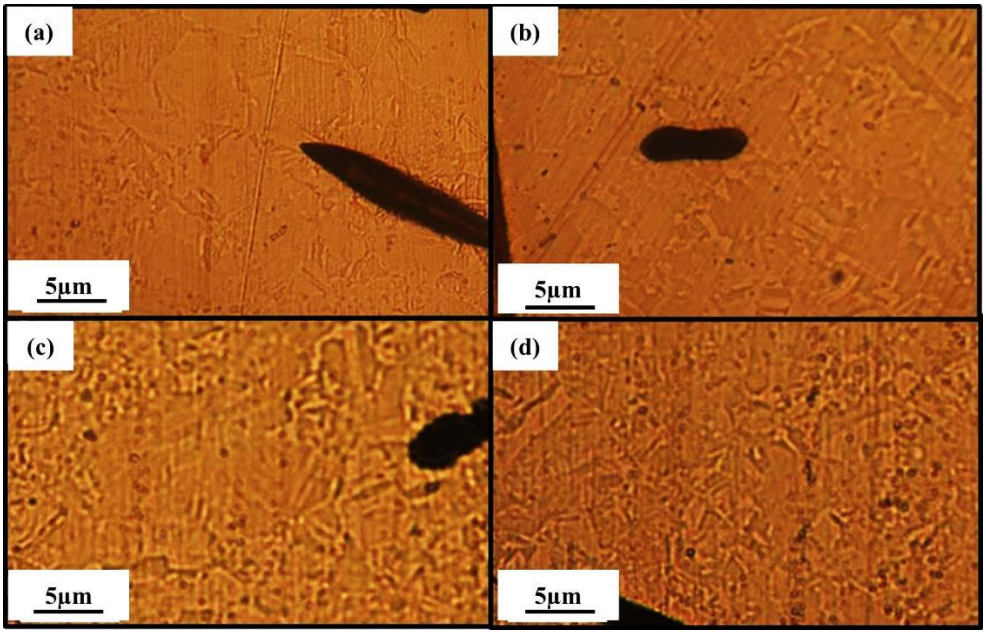

Figure 5.23: Optical micrographs of copper-graphite coatings produced by electrodeposition at (a) 50 mA (b) 100 mA (c) 150 mA and (d) 200 mA

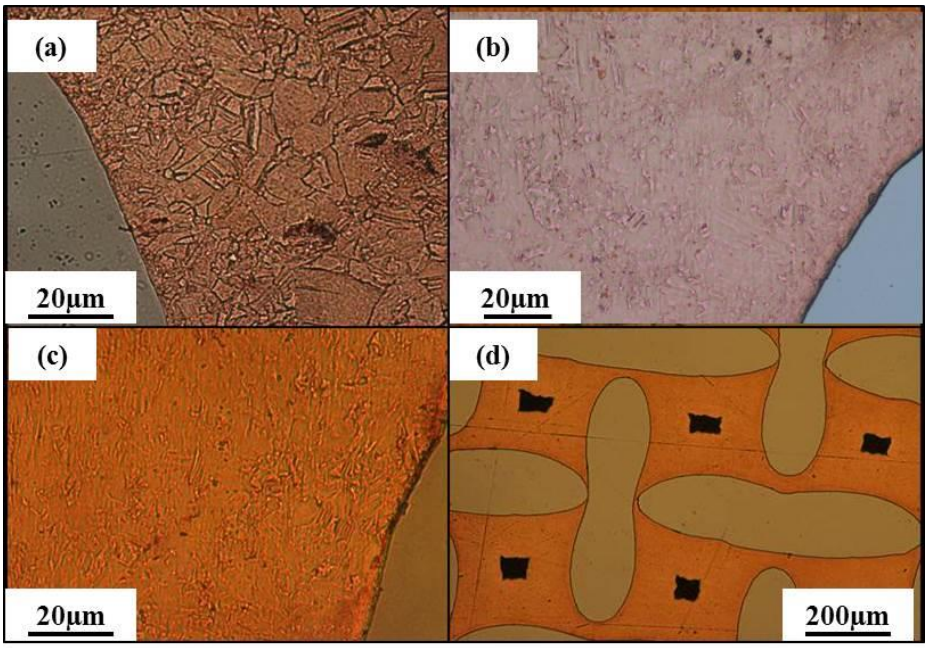

Figure 5.24: Optical micrographs of copper-graphite coatings produced by electrodeposition at (a) 50 mA (b) 100 mA (c) 150 mA and (d) 200 mA

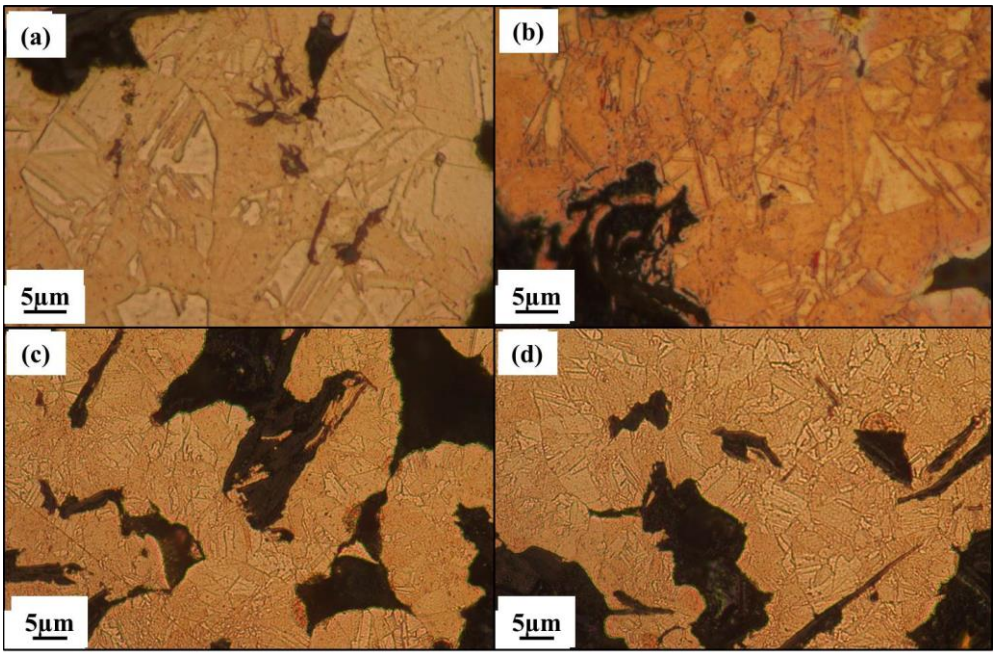

Figure 5.25: Optical micrographs of copper-graphite coatings produced by electrodeposition at (a) 50 mA (b) 100 mA (c) 150 mA and (d) 200 mA

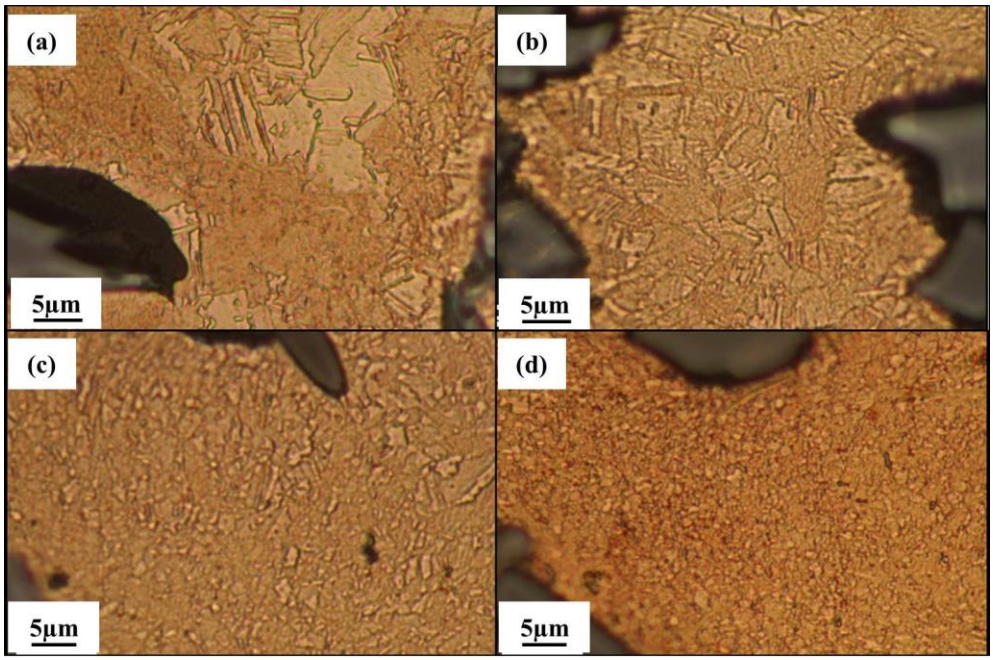

Figure 5.26: Optical micrographs of copper-SiC coatings produced by electrodeposition of copper at (a) 50 mA (b) 100 mA (c) 150 mA and (d) 200 mA

It was also observed that the grain size of copper was smaller when it was electrodeposited into non-conducted porous media. Coatings with high density were obtained when copper was electrolytically infiltrated into electrically non-conducting porous media: Nomex felt and laser sintered SiC.

Table 5.6 shows the grain size of copper and density of the composite coatings. Table 5.6 also shows the electrical potential required to apply current of 50mA, 100mA, 150mA and 200mA in the flow cell. It was observed that, as the conductivity of the porous media decreased, higher electrical potential was required to apply current. As the conductive surface area increases, more sites are available for copper reduction reaction. Hence, a larger current can be applied at a lower

applied potential. Figure 5.27 shows the X-ray diffraction patterns obtained from the composite coatings.

Sample	Current (mA)	Potential (V)	Grain Size (μm)	Density (%)	Hardness (VHN)
Copper-Nomex	50	0.01	4.5±0.3	97%	122
	100	0.02	4.3±0.6	96%	124
	150	0.066	3.2±0.4	98%	119
	200	0.1	2.4±0.6	95%	120
Copper-SS316	50	0.01	4.1±0.5	94%	129
	100	0.015	3.9±0.6	91%	126
	150	0.023	3.4±0.5	84%	117
	200	0.045	--	71%	--
Copper-graphite	50	0.01	7.5±0.6	89%	122
	100	0.04	5.7±0.8	87%	117
	150	0.08	4.6±0.5	88%	117
	200	0.1	3.8±0.5	83%	109
Copper-SiC	50	0.01	4.9±0.9	97%	132
	100	0.05	3.4±0.6	95%	130
	150	0.1	2.1±0.2	95%	127
	200	0.12	1.5±0.1	92%	119

Table 5.6: Grain size and density of the electrodeposited copper matrix. The applied potential corresponding to the applied current is also shown.

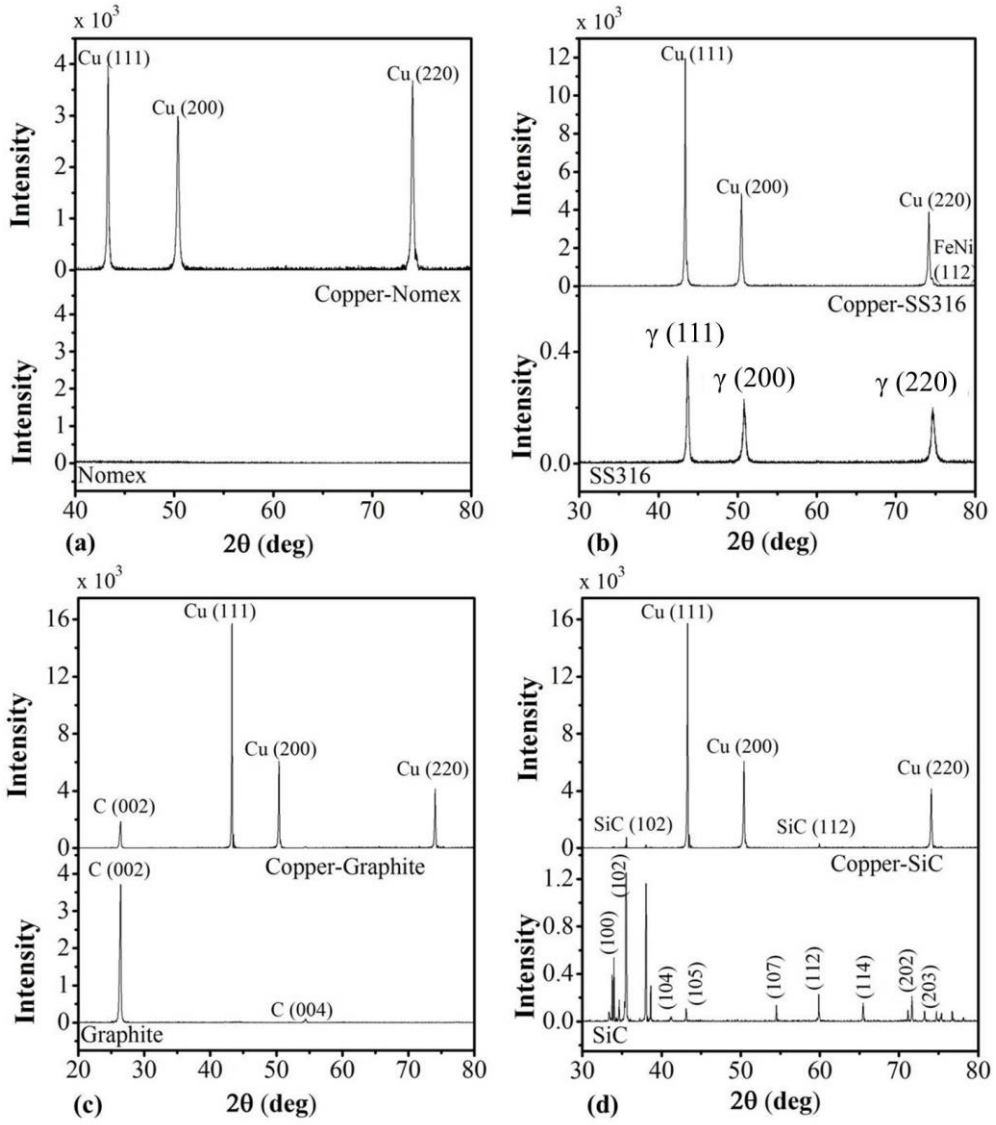

Figure 5.27: X-ray diffraction patterns obtained for composite coatings: (a) Copper-Nomex (b) copper-SS316 (c) Copper-graphite (d) Copper-SiC

All the X-ray diffraction patterns obtained by diffraction on coating surfaces showed characteristic peaks of elemental copper corresponding to {111}, {200} and {220} planes. The X-ray diffraction pattern of Nomex felt was devoid of any sharp peak in the interval of 40^o to 90^o. The diffraction pattern stainless steel showed sharp peaks corresponding to {111}, {200} and {200} planes of austenite. The peaks occurred at angles close to the diffraction angles for

elemental copper. It was possible to make out the peak for {200} planes of austenite in form of a small neck with the (220) peak of copper. Peaks were observed for graphite corresponding to the {200} and {004} planes and were also present in the XRD patterns of the copper-graphite coatings as shown in figure 5.27(c). In figure 5.27(d) the peaks were observed for several planes of Mossainite (6H) form of silicon carbide. It was possible to observe the peaks corresponding to {112} and {112} planes in the copper-SiC coatings.

5.8.3. Thermal conductivity

Table 5.7 shows thermal diffusivity, specific heat and thermal conductivity of the copper-110 alloy measured using a laser flash method and differential scanning calorimetry. The values presented here are close to those found in literature [113]. Figure 5.28 shows a DSC plot of the reference (sapphire) and control (copper-110 alloy) samples used in the study. The ordinate variations from the baseline, Y and Y', of the reference and the control sample, respectively, were used to find the specific heat capacity at constant pressure of the corresponding samples. The specific heat capacity, C_p, of the sapphire reference at temperatures ranging from 50^{o}C-200^{o}C can be found in the literature. The ratio Y: Y' was measured at the temperatures of interest and equation (4.10) was used to find the corresponding value of specific heat capacity of copper-110 alloy.

Figure 5.29 shows thermal diffusivity of the composite coatings prepared in this study. The value of thermal diffusivity was highest for copper-nomex coatings. This is possibly because the coatings consisted of ~95% copper and only ~5% Nomex. As the current for copper electrodeposition was increased, the thermal diffusivity of all composite coatings was lowered due to an increase in the pore volume fraction. The value of thermal diffusivity of copper is

much higher than Cu-Graphite and Cu-SiC. On the other hand Cu-Graphite has much lower thermal diffusivity compared to Cu-SiC due to a higher pore volume fraction in Cu-Graphite as well as a higher percentage of cross-linked phenolic resin.

Figures 5.30-5.33 show the DSC plots the free standing composite coatings. The calculated values of specific heat capacity at various temperatures for different types of composite coatings are shown in table 5.8. It was observed that the specific heat capacity increased with the applied current at which electrodeposition was carried. This can be attributed to increase in porosity with the increase in applied current. Table 5.9 shows the thermal conductivity of those specimens. There was a very small difference in the thermal conductivity of the samples obtained for the composite coating obtained under different applied currents.

Temperature (^{o}C)	Thermal Diffusivity (mm^2/s)	Specific Heat Capacity ($J/g/^{o}C$)	Thermal Conductivity (W/m-K)
50	109.68	0.387	380
100	106.32	0.396	375
150	102.56	0.405	370
200	98.42	0.412	360

Table 5.7: Thermal diffusivity, specific heat capacity and thermal conductivity of copper-110 alloy

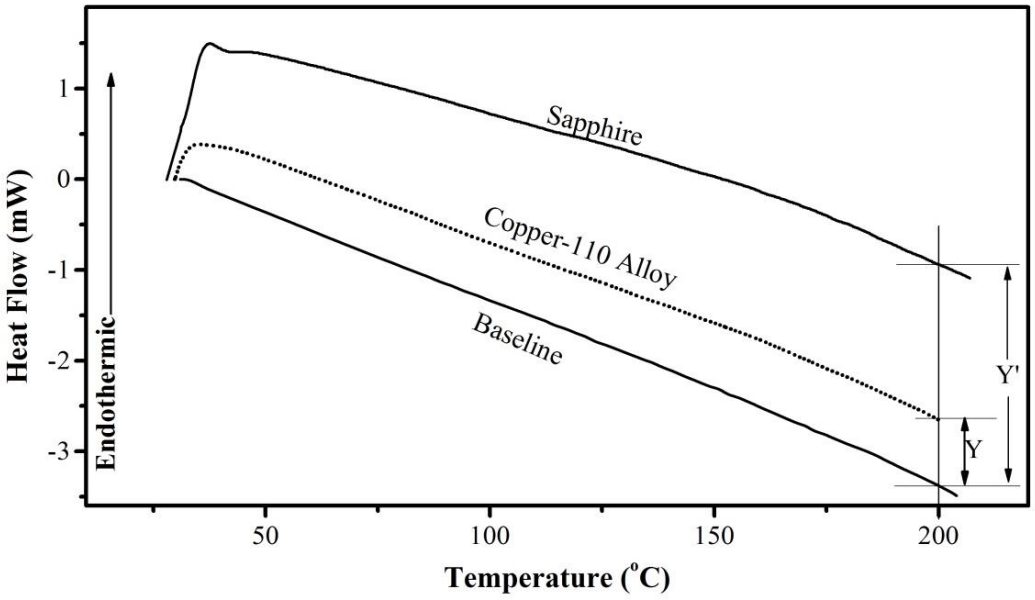

Figure 5.28: DSC plots showing heat flow into the sapphire reference and copper-110 alloy

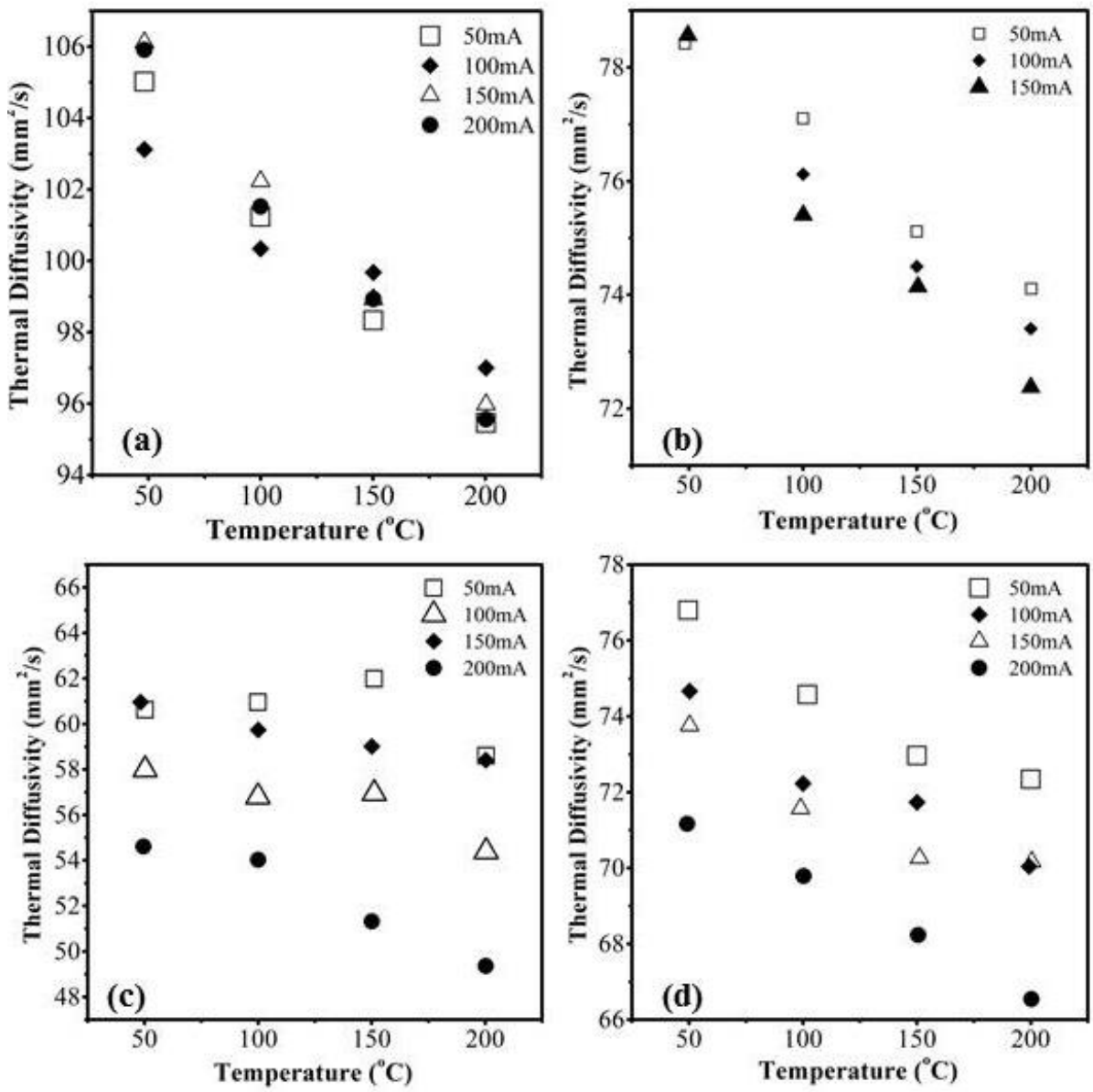

Figure 5.29: Thermal diffusivity of (a) Cu-Nomex, (b) Cu-SS 316, (c) Cu-Graphite and (d) Cu-SiC at temperatures ranging from 50-200°C. The data shown above is within a standard deviation of 10%.

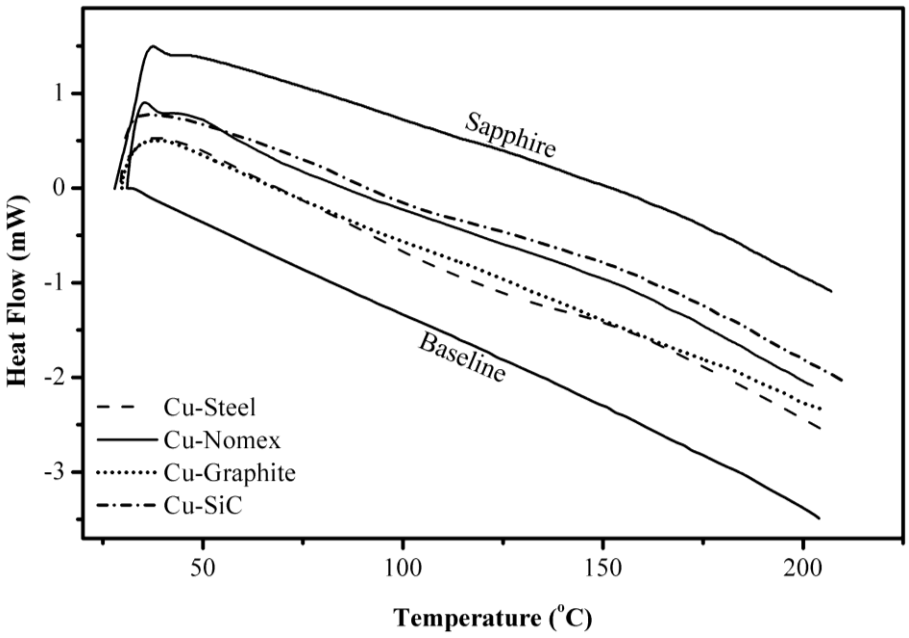

Figure 5.30: DSC plots of free standing composite coatings produced by electrochemical infiltration at an applied current of 50mA

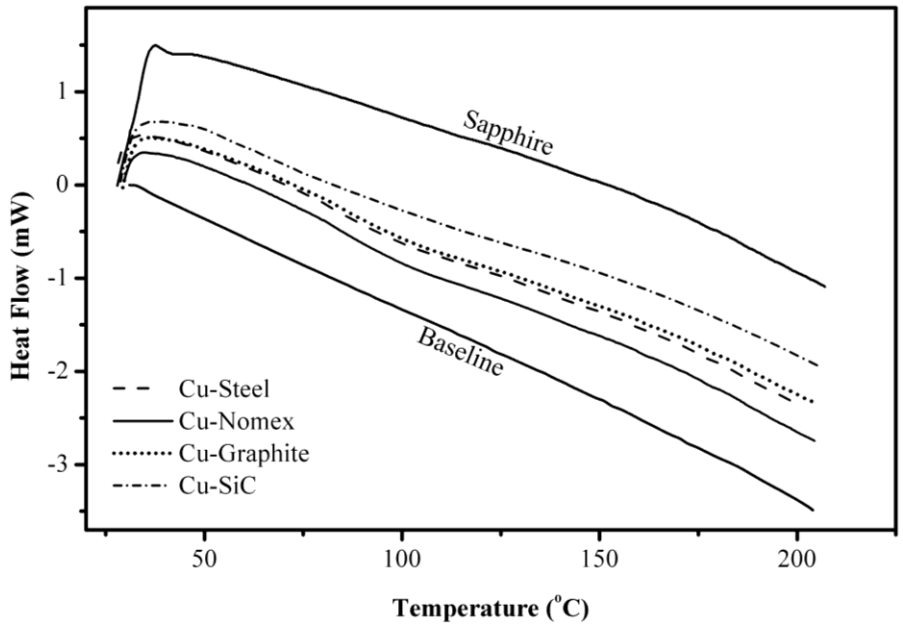

Figure 5.31: DSC plots of free standing composite coatings produced by electrochemical infiltration at an applied current of 100mA

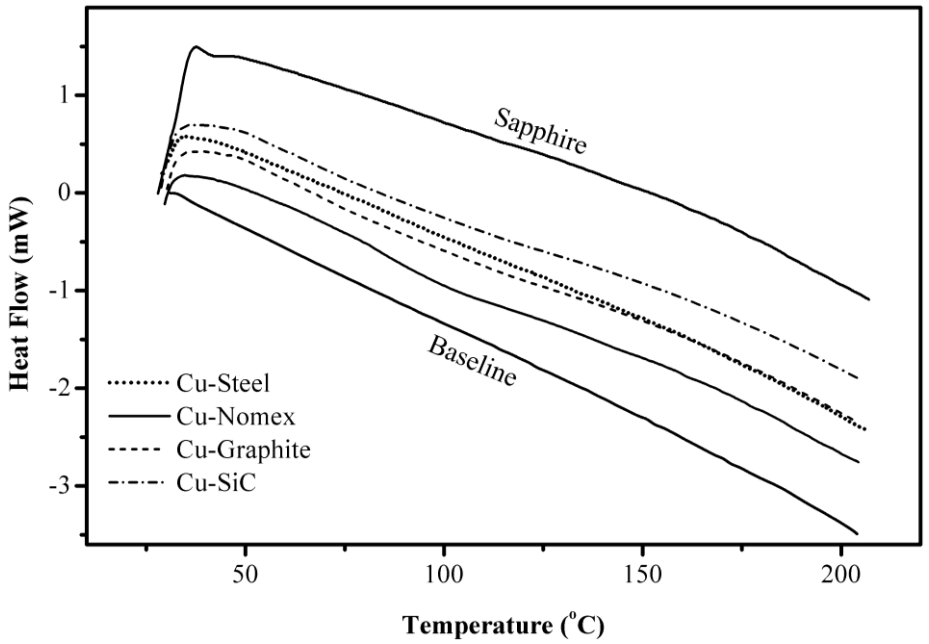

Figure 5.32: DSC plots of free standing composite coatings produced by electrochemical infiltration at an applied current of 150mA

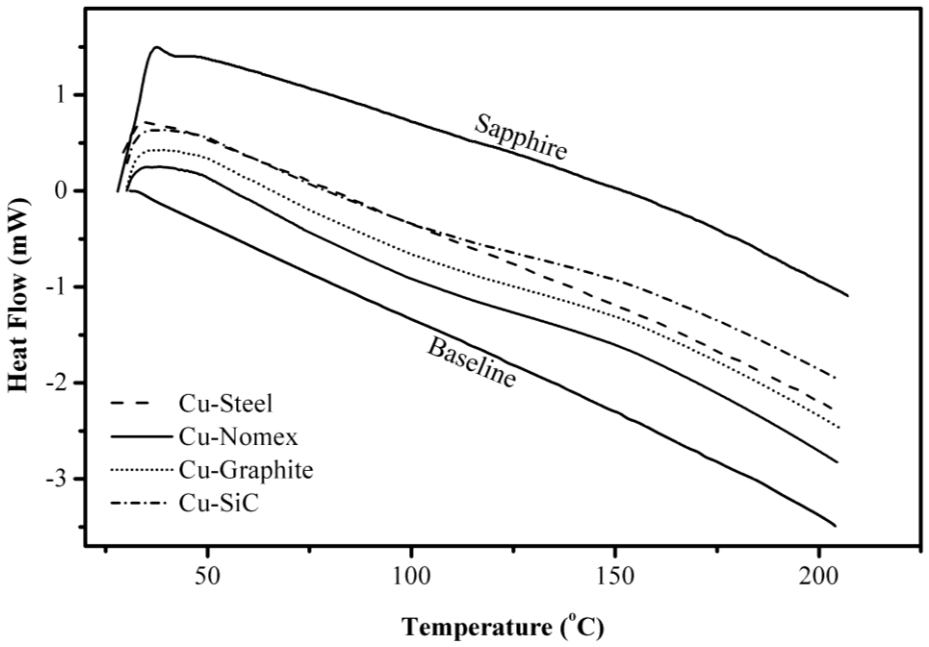

Figure 5.33: DSC plots of free standing composite coatings produced by electrochemical infiltration at an applied current of 200mA

Specimen	Temperature	Specific Heat (J/g/°C)			
		Deposition Current			
		50 mA	100 mA	150 mA	200 mA
Copper-SS304	50	0.394	0.395	0.446	—
	100	0.479	0.408	0.490	—
	150	0.411	0.416	0.505	—
	200	0.430	0.430	0.520	—
Copper-Nomex	50	0.394	0.395	0.390	0.395
	100	0.405	0.408	0.399	0.398
	150	0.412	0.416	0.407	0.407
	200	0.424	0.430	0.423	0.411
Copper-Graphite	50	0.483	0.451	0.431	0.421
	100	0.535	0.510	0.485	0.481
	150	0.574	0.541	0.515	0.515
	200	0.599	0.575	0.550	0.540
Copper-SiC	50	0.438	0.424	0.425	0.400
	100	0.474	0.476	0.476	0.459
	150	0.532	0.455	0.455	0.455
	200	0.552	0.558	0.558	0.523

Table 5.8: Specific heat capacity of composite coating at various temperatures and electrodeposition conditions. The standard deviation is less than 5 %.

Specimen	Temperature	Thermal Conductivity (W/m-K)			
		Deposition Current			
		50 mA	100 mA	150 mA	200 mA
Copper-SS304	50	268.09	266.48	278.70	—
	100	320.46	263.96	293.89	—
	150	267.88	263.40	297.83	—
	200	276.50	268.27	299.36	—
Copper-Nomex	50	349.98	340.91	339.00	331.51
	100	346.79	342.64	334.13	320.19
	150	342.66	347.05	329.81	319.07
	200	342.37	349.10	332.58	311.24
Copper-Graphite	50	207.9	191.22	172.71	141.24
	100	224.63	211.88	190.37	159.64
	150	240.53	222.05	202.66	162.37
	200	249.21	233.6	206.72	163.73
Copper-SiC	50	248.07	226.63	218.74	185.25
	100	260.69	248.61	241.2	208.28
	150	286.28	233.91	223.52	201.66
	200	294.5	280.28	269.99	225.79

Table 5.9: Thermal conductivity of free standing composite coating at various temperatures and electrodeposition conditions. The standard deviation is less than 10 %.

5.8.4. Tribological properties

Figures 5.34-5.36 show the dynamic coefficient of friction as a function of sliding distance of the alumina ball on the coatings. The coefficient of friction was recorded as the ratio of tangential

force and the normal load applied by the tribometer. The COF behavior of the samples differed significantly. The COF of copper-110 alloy quickly increased to a value of 0.7 and the dipped several times only to recover very quickly. This may be interpreted as gradual accumulation of debris and which clears out and then begins to accumulate again. Similar behavior of COF was also seen for copper-SS316 coating. The COF of copper-SiC coatings increased to value just above 0.6 and showed a gradual increase with the sliding distance. Copper-Nomex coatings showed a quick increase in the COF as the tribological testing was started. It stayed constant at a value of 0.4 for a distance of 100m and then increased to a value of 0.5. Copper-graphite coatings showed an increase in the coefficient of friction to 0.15 and decreased as the sliding distance was increased. This can be attributed to the self-lubricating properties of graphite. It was observed that at all sliding speeds, copper-110 alloy had the highest coefficient of friction (~0.8). Copper-graphite coatings had the lowest coefficient of friction (~0.2) at all sliding speeds.

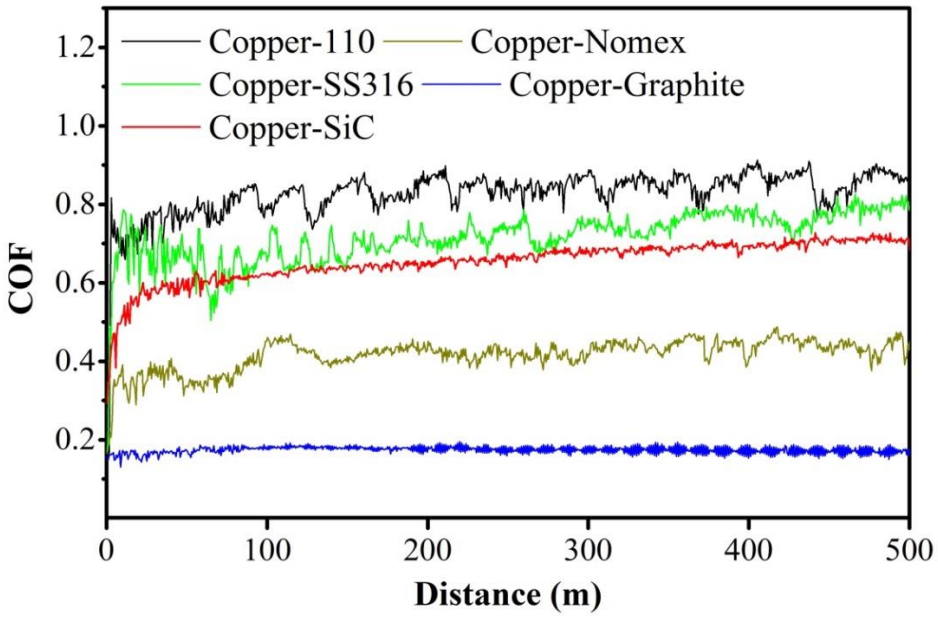

Figure 5.34: Dynamic coefficient of friction (COF) as a function of distance for various surfaces tested using an alumina ball at a speed of 1200 mm/min

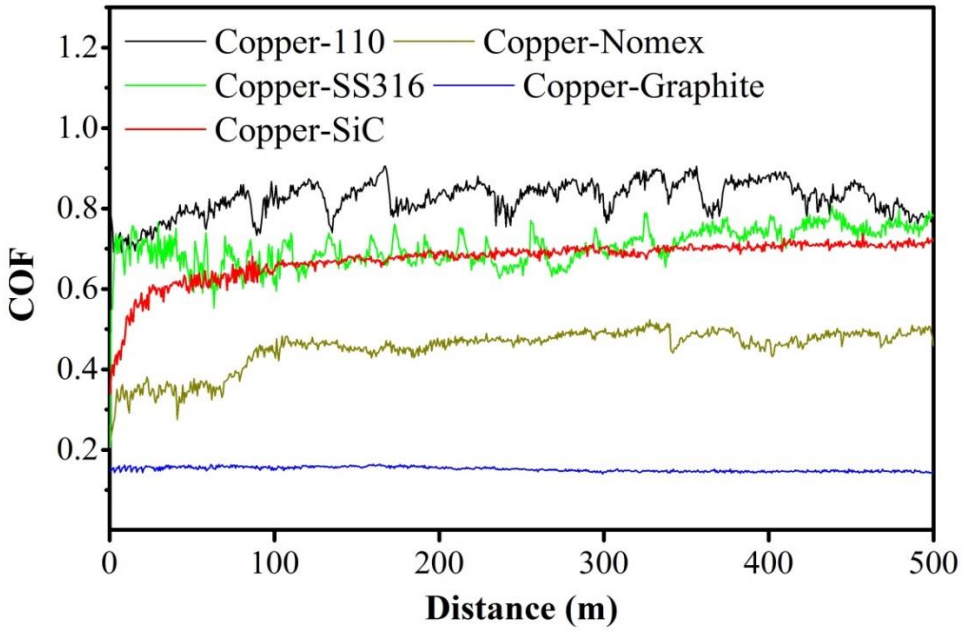

Figure 5.35: Dynamic coefficient of friction (COF) as a function of distance for various surfaces tested using an alumina ball at a speed of 1800 mm/min

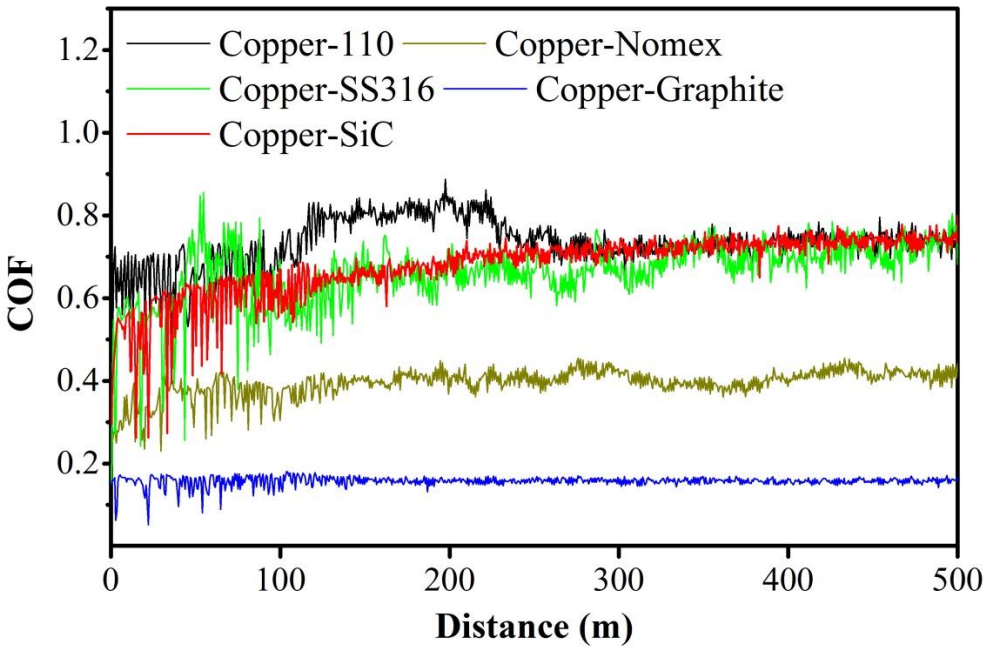

Figure 5.36: Dynamic coefficient of friction (COF) as a function of distance for various surfaces tested using an alumina ball at a speed of 2400 mm/min

Figures 5.37-5.41 show depth profiles of the composite coatings along the wear tracks formed by sliding wear after 500 m of sliding distance. In all the depth profiles, it was observed that the depth of the wear tracks increased as the sliding speed was increased. However, copper-nomex and copper-SS316 coatings showed a very small increase in the depth of the wear track formed at sliding speeds of 1800 mm/min and 2400 mm/min. The depth of the wear tracks formed on the copper-SiC ranged between 7µm-15µm and was the lowest among all the materials tested. Copper-SS316 composite coatings had the deepest wear tracks with the wear depth ranging from 80µm-100µm. Copper-110 alloy specimen showed a large variation with the increase in sliding speed.

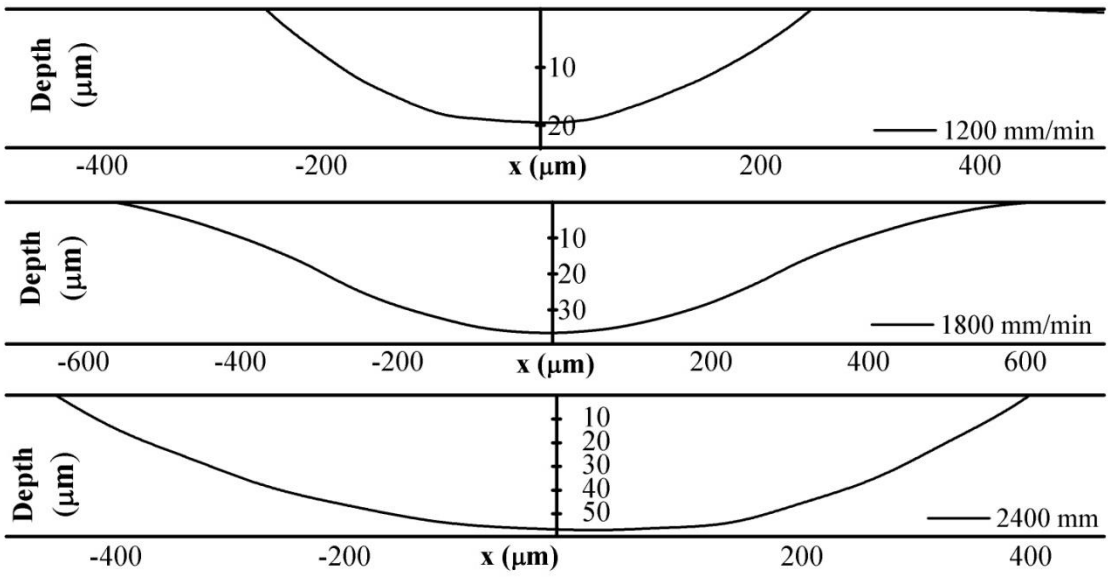

Figure 5.37: Depth profile of the wear track formed on copper-110 alloy after sliding distance of 500 m

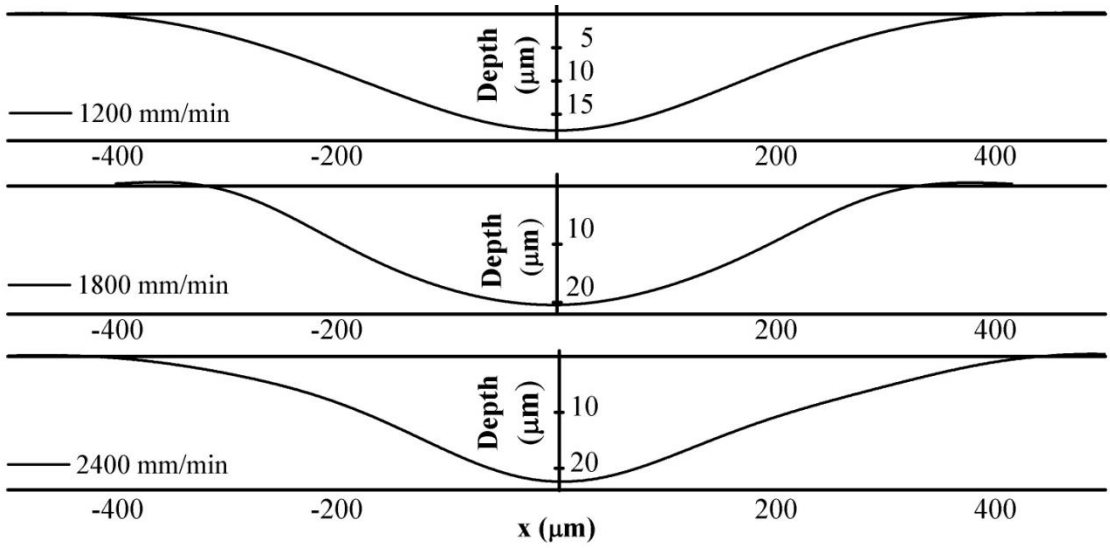

Figure 5.38: Depth profile of the wear track formed on copper-nomex coatings after sliding distance of 500 m

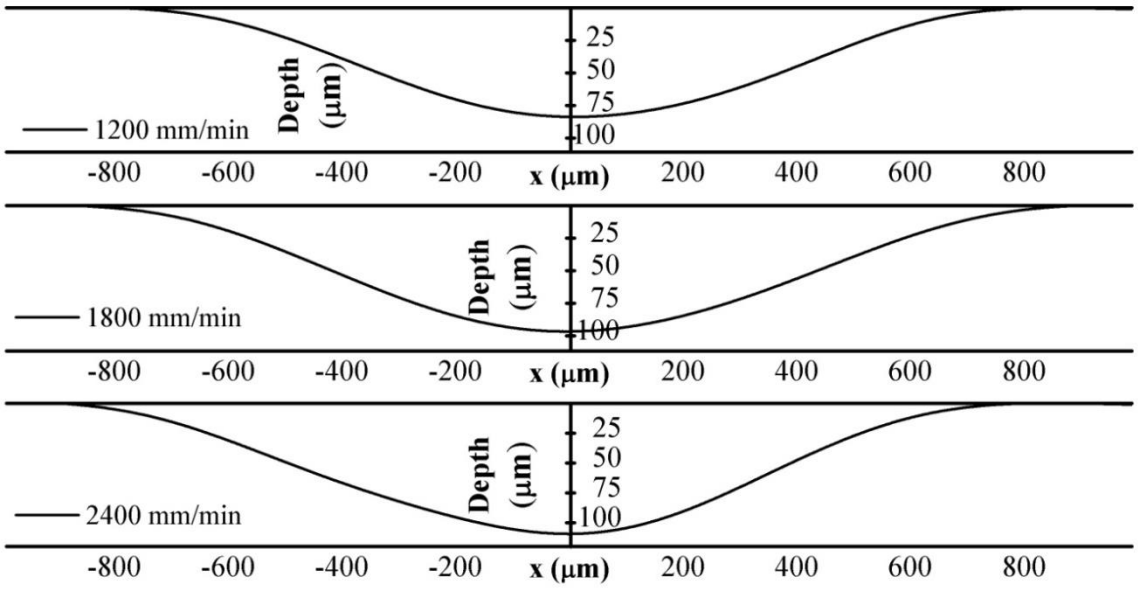

Figure 5.39: Depth profile of the wear track formed on copper-SS316 coatings after sliding distance of 500 m

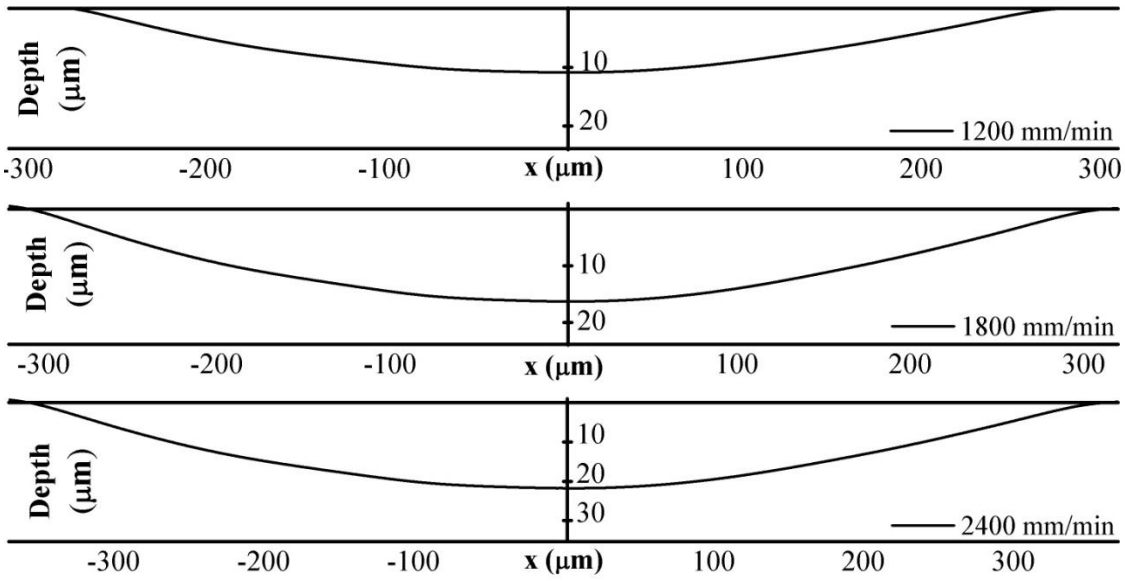

Figure 5.40: Depth profile of the wear track formed on copper-graphite coatings after sliding distance of 500 m

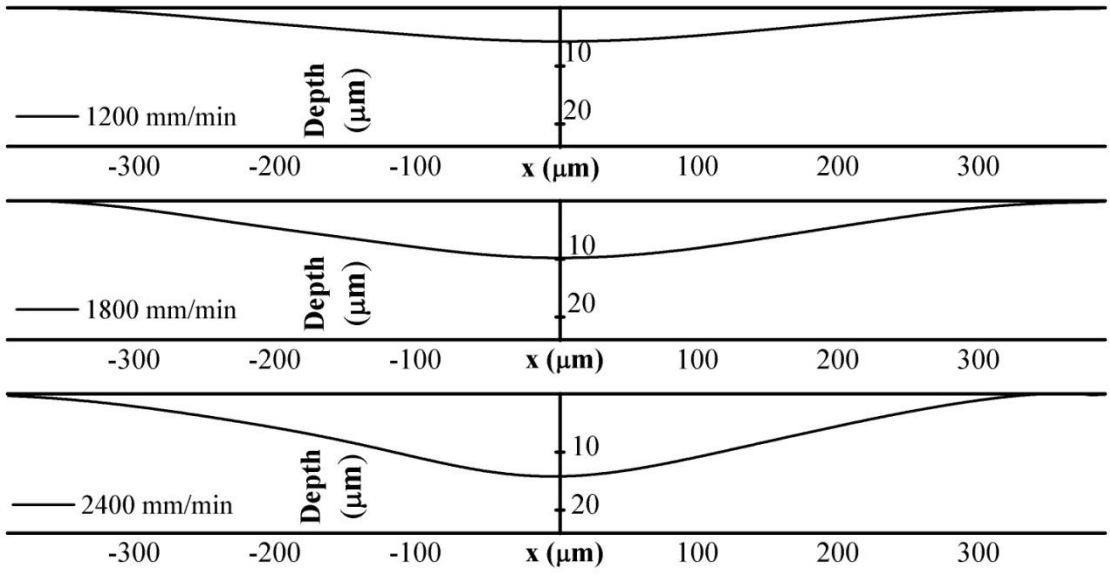

Figure 5.41: Depth profile of the wear track formed on copper-SiC coatings after sliding distance of 500 m

Figure 5.42 shows the wear rate of the composite coatings calculated using the depth profile described earlier. It was observed that copper-graphite and copper-SiC composite coatings had much lower wear rate compared to copper-110 alloy. On the other hand Copper-SS-316 showed the highest values of wear rate.

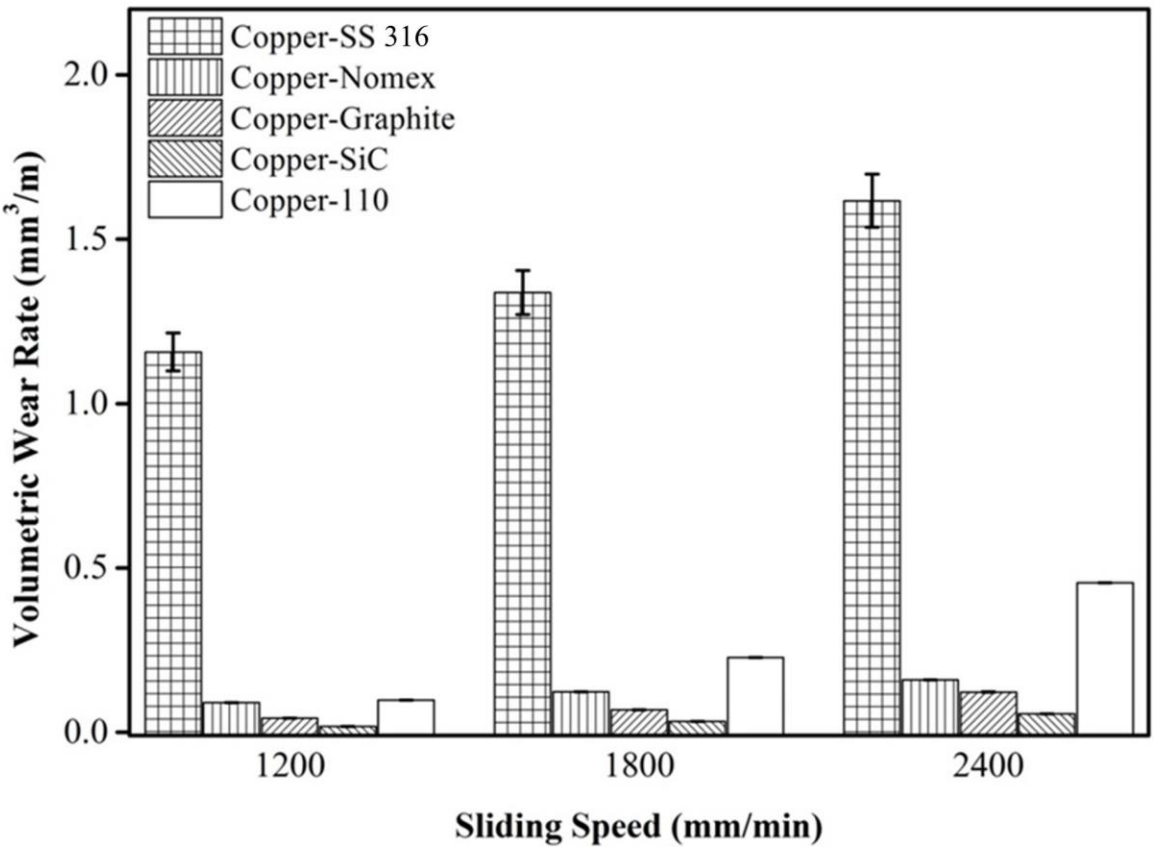

Figure 5.42: Wear rate of the various composite coatings after 500m of sliding distance

Chapter 6: Discussions[1]

6.1.1. Porosity and pore Size of the laser sintered parts

The pore volume fraction of the laser sintered parts increased as the burnout temperature and minimum layer thickness used during laser sintering of the parts. In general, graphite parts had showed slightly higher porosity compared to silicon carbide parts.

During binder burnout, the phenolic resin is pyrolysed which leads to breakdown of phenol formaldehyde and production of gaseous pyrolysis products. Pyrolysis of phenol formaldehyde occurs in three steps as shown in thermograms shown in figure 6.1 [92]. In the first step, phenol, cresol and water are evolved from 300^{o}C to 550°C. From figure 6.1 it can be observed that this region shows highest percentage weight loss in the phenol formaldehyde resin. In the second step, from 400^{o}C to 800^{o}C, hydrogen, methane, carbon monoxide, carbon dioxide and water are evolved. In the third step, hydrogen, carbon monoxide and water are evolved from 560^{o}C to 900^{o}C. Binder burnout at higher temperatures results in the reduction of the phenol formaldehyde to amorphous carbon [114, 115]. The increased weight loss at higher temperature removes larger amount of material and leads to an increase in the porosity of the final brown part. The pore size of the laser sintered parts was found to be of the order of the particle size of the powder particles used in the SLS process. It was found that due to smaller particle size and better packing of the silicon carbide powder the pore size diameter of the silicon carbide parts was smaller

[1] The work presented here has been published in International Journal of Precision Engineering and Manufacturing 14 (6), 881-889 and Materials Science and Technology, 2014. This work was supervised by David Bourell.

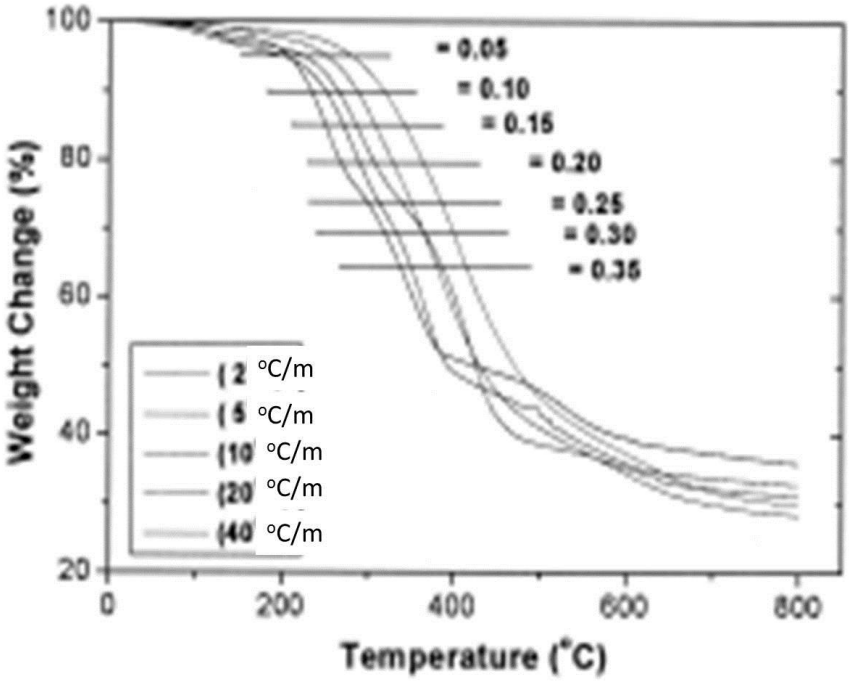

Figure 6.1: Thermograms of a novolac resin (F/P = 0.5) with the heating rate.[92]

6.1.2. Electrical conductivity

The electrical conductivity of the laser sintered parts increased as the binder burnout temperature was increased. Kaushik and Bourell published values of electrical conductivity of laser sintered graphite and its dependence on binder burnout temperatures [5]. These values are shown in figure 6.2 are in good agreement with this study. The carbon product of the phenolic burnout is amorphous in nature and contributes significantly to the increase in the electrical conductivity of the laser sintered parts. According to Bhatia [114], electrical conductivity shows an increase of the order of 10^2 when the temperature for binder burnout is increased from 800^{o}C to 1250^{o}C. As the binder burnout temperature is further increased, there is also a structural change in the glassy carbon which starts converting into graphite [116]. This improves the electrical conductivity of the laser sintered parts. Hence, the increase in the electrical conductivity may be due in part to

the conversion of amorphous carbon into a semicrystalline phase and also a reduction in porosity of the phenolic carbonization residue.

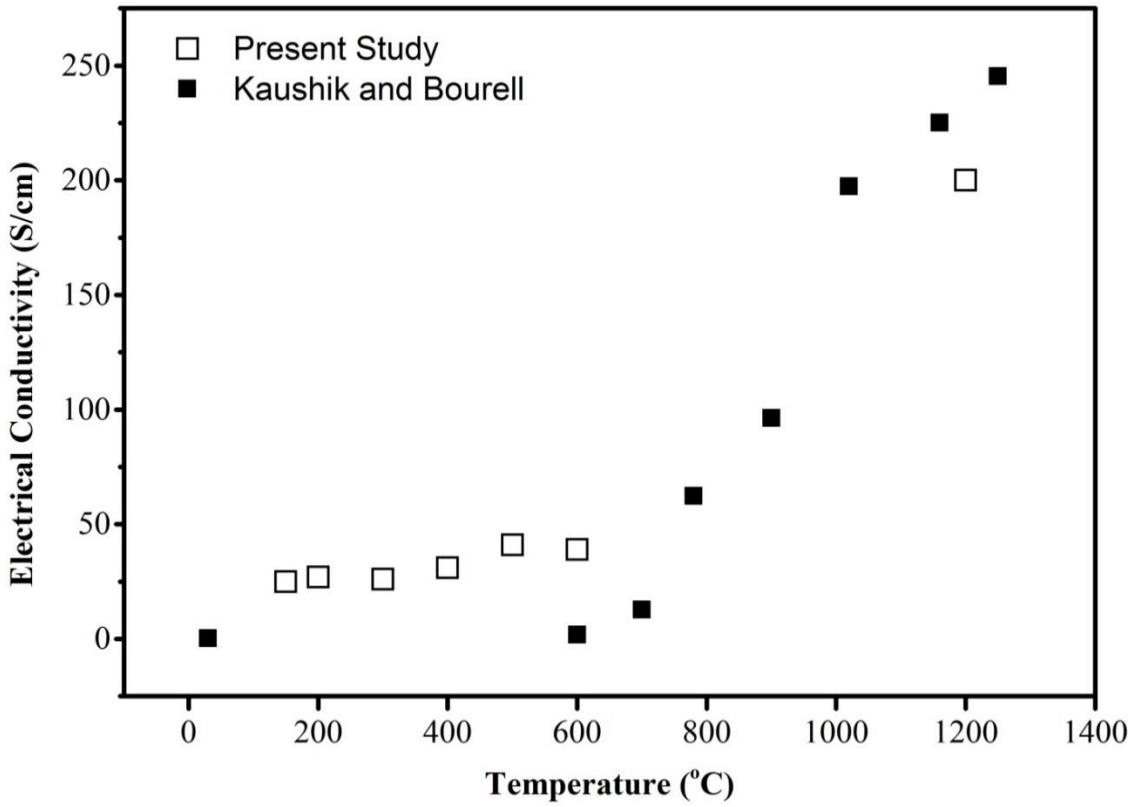

Figure 6.2: Electrical conductivity of laser sintered graphite as a function of binder burnout temperature.[93]

6.2. Electrolyte properties

6.2.1. Viscosity and contact angle

The viscosity the aqueous copper sulfate solutions increased with the increase in the concentration of copper sulfate as well as sulfuric acid.

Price and Davenport derived an empirical relationship to correlate the dynamic viscosity of aqueous copper sulfate solutions with concentration of $CuSO_4$ and H_2SO_4 [117]:

$$\mu = 10^{-6}(1592 + 0.0108[H_2SO_4]^2 + 2.373[H_2SO_4] + 29.93[Cu] + 76.4[Cu]^{1/2})\exp\frac{1890}{T} \quad (6.1)$$

where μ is the dynamic viscosity, T is the temperature; $[H_2SO_4]$ and [Cu] are the concentrations of H_2SO_4 and Cu in g/L in the aqueous solutions. It was observed that the experimental results obtained here showed good agreement with the values obtained using the empirical relationship in equation (1.2). The viscosity of the electrolytes increases with the concentration of copper sulfate and sulfuric acid. The viscosity of an electrolyte can be related to solvent by [118, 119]:

$$\frac{\mu_{solution}}{\mu_{solvent}} = 1 + A\sqrt{c} + Bc + Dc^2 \quad (6.2)$$

where A, B and D are constants and c is the concentration of the ions in the solution which depend on solute-solvent interaction. As the concentration of the solute increases, the viscosity of the electrolyte shows a non-linear increase. Due to the polar nature of water molecules, a hydration sphere is formed around the solute ions [120]. As the charge of the ions goes up, more than one hydration sphere is formed around the solute ions. The increase in the size of hydration sphere also contributes to an increase in the viscosity of the solution. Similarly, addition of a Triton X-100 also leads to an increase in the viscosity of the solution. The micellar structure of a surfactant in a solvent and formation of the hydration sphere due to polar nature of the surfactant molecules are the key reasons for increase in viscosity of solutions containing Triton X-100 [121-123]. It has also been observed that the presence of any ionic species in the solution causes a further increase in viscosity of the solution containing Triton x-100 [124].

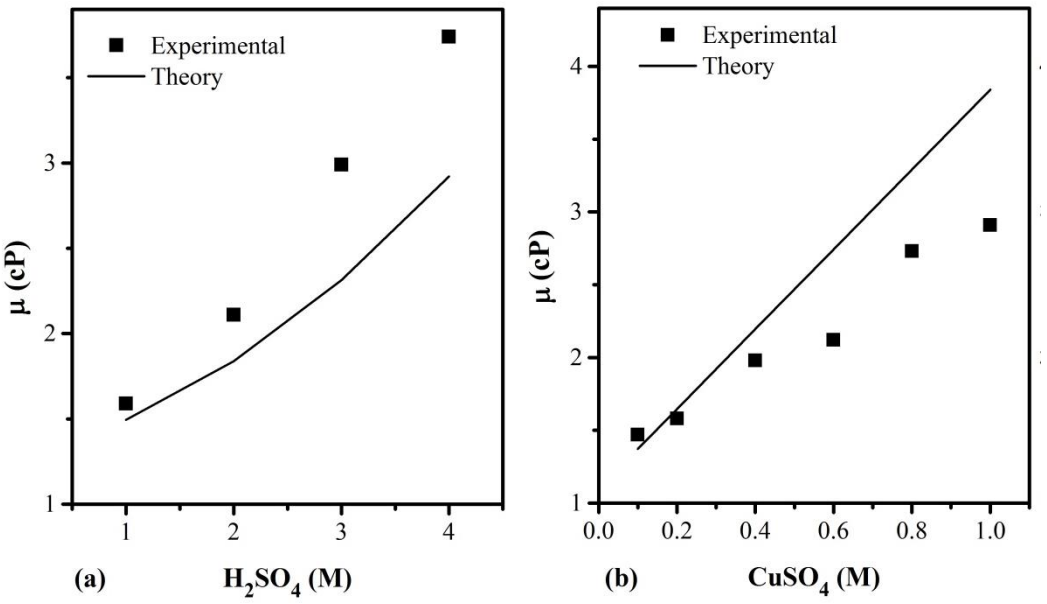

Figure 6.3: Comparison of viscosity of $CuSO_4/H_2SO_4$ solutions with equation (6.1).

Triton X-100 is a non-ionic surfactant that has been used as a dispersion agent for carbon nanotubes in aqueous and organic solvents [96, 125]. Non-ionic surfactants modify the liquid-vapor and liquid-surface interface in the droplet and lead to the formation of monolayers and bilayers of adsorbed surfactant molecules. These molecules modify the force field of the underlying surfactant molecules and improve wetting [125]. Traditionally, time to complete penetration of porous solids is approximated by the path of flow of liquid into a parallel bundle of smooth-walled capillaries [126, 127]. This can be done using Lucas-Washburn equation:

$$t = \frac{2H^2}{\gamma_L R\cos\theta}\mu \qquad (6.3)$$

Here, t is the time required for complete filling of the porous media, H is the thickness of the porous part, γ_L is the surface tension of the liquid, R is the average pore size, θ is the contact angle and μ is the dynamic viscosity of the liquid.

The Lucas-Washburn equation was used to approximate the time required for impregnation of the laser sintered parts with the electrolyte containing 0.1 M $CuSO_4$ and 4 M H_2SO_4 in water with varying concentration of Triton X-100. Following values were used, H = 2 mm, R = 70 µm and γ_L = 72 mN/mm^2. The values of viscosity and contact angles from chapter 5 (figure 5.4 and 5.5) were used for μ and θ respectively. The surfactant in the solution decreases the time required for complete impregnation of the laser sintered parts with the electrolyte. As the concentration of the surfactant was increased beyond 1 ml/l, the time required for the impregnation of the laser sintered parts showed a slight increase. Consequently, a concentration of 1 ml/l of surfactant was used in the electrolytes used for the infiltration experiments.

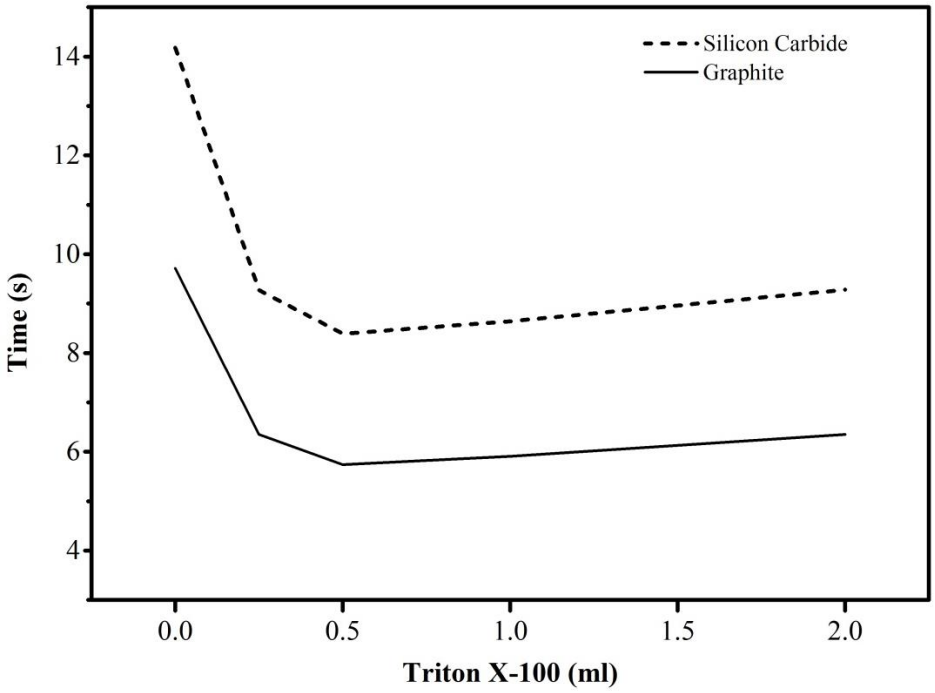

Figure 6.4: Approximate time required for complete impregnation of laser sintered parts by the electrolyte using equation (6.3).

6.2.2. Electrical conductivity of the electrolytes

The electrical conductivity of the electrolytes showed an increase with the increase in the concentration of H_2SO_4 in the electrolyte. It was observed that the increase in the concentration of $CuSO_4$ did not have the same impact on the electrical conductivity of these electrolytes. According to Kamelin and co-workers, this decrease is due to an increase in the viscosity of the electrolytes with the increase in the concentration of copper sulfate [128]. Since SO_4^{2-} is a product of dissociation of both $CuSO_4$ and H_2SO_4, the solubility of $CuSO_4$ is limited by the concentration of H_2SO_4 present in the solution due to common ion effect. Therefore, to get highly electrically conductive electrolytes, it is required to increase the concentration of H_2SO_4 and decrease the concentration of $CuSO_4$.

The electrical conductivity of $CuSO_4/H_2SO_4$ solutions can be represented by the following empirical relationship [117]:

$$\kappa = 0.134 - 0.00356[\mathrm{Cu}] + 0.00249[\mathrm{H_2SO_4}] + 0.00426(T - 273) \qquad (6.4)$$

where, κ is the electrical conductivity, [Cu] is the concentration of copper ions and [H_2SO_4] is the concentration of sulfuric acid in the solution and T is the temperature in Kelvin.

Figure 6.4 shows comparison of electrical conductivity of the electrolytes with the theoretical value obtained using the equation (6.4). The predicted values of electrical conductivity are much higher than the experimental values obtained in this study in figure 6.5(a). This is possibly due to increased viscosity of the electrolytes in the presence of the surfactant

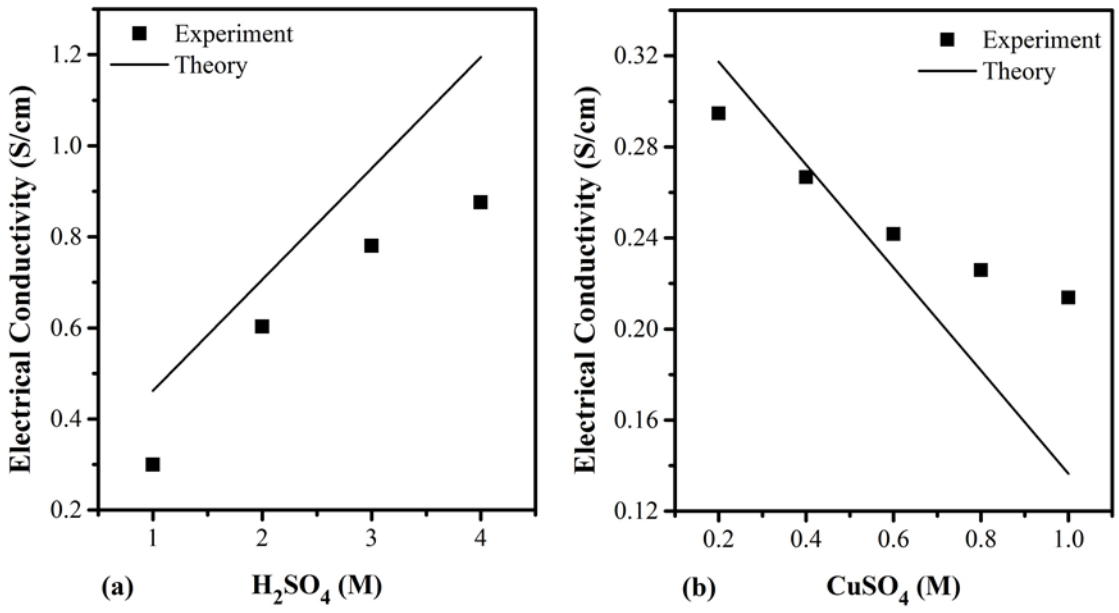

Figure 6.5: Comparison of the experimental values of electrical conductivity obtained in this study with that obtained using equation (6.4): (a) with H_2SO_4 concentration in 0.1 M $CuSO_4$ and (b) with $CuSO_4$ in 0.5 M H_2SO_4

6.3. Electrochemical characterization

6.3.1. Diffusion coefficient of copper ions

The linear potential scans carried out to determine the reduction potential of copper ions and hydrogen ions clearly showed that it was possible to reduce copper ions without the evolution of H_2 gas. The electrochemical infiltration experiments were carried out in the regions where Cu^{2+} was not mass transfer limited. The presence of ample amount of copper ions allowed for higher currents to be applied at lower voltages and also prevented evolution of hydrogen during the electrodeposition process.

Figure 6.6 shows a plot of $v^{1/2}$ versus peak current, where, v is the potential scan rate. The slope, m, of the linear fit is equal to $(2.99\times10^5)\alpha^{1/2}AC_0^*D_0^{1/2}$ [65]. Here, α is the charge transfer coefficient, A is the area of the electrode and is equal to 1 cm^2, C_0^* is the bulk concentration of the copper ions in the electrolyte. Thus the slope can be used to find the coefficient of diffusion D_0.

The diffusion coefficient was found to be equal to 1.3 × 10^{-6} cm^2/s with a standard deviation close to 10%. This value was used in the computations performed in chapter 3.

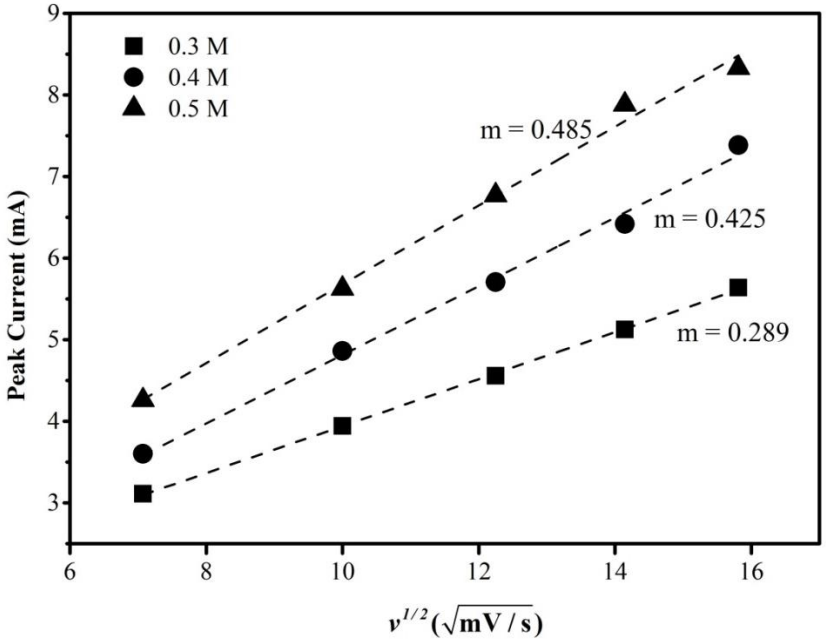

Figure 6.6: Plot of peak current vs square root of potential scan rate for solutions with different concentration of $CuSO_4$ in 0.5 M H_2SO_4

Published values of diffusion coefficient of copper ions in aqueous solutions are scattered over 3.1×10^{-6} cm^2/s to 8.6×10^{-6} cm^2/s [129, 130]. These values have been determined using various methods such as chronoamperometry, potential scans and cyclic voltammetry etc. [130]. The value of diffusion coefficient reported in this study is lower owing to the presence of a surfactant

in the solution. Surfactant molecules are able to form complexes with heavy metal ions [131]. These complexes are larger in size compared to copper ions and can lead to reduction in diffusion coefficient of the copper ions.

6.3.2. Rate of reaction and charge transfer coefficient

The reduction of copper ions is a two-step electrochemical process. The reaction occurs via the reduction of cupric ions to cuprous ions and the then reduction and lattice incorporation of the cuprous ions [132]:

$$Cu^{2+} + e^{-} \underset{\longleftarrow}{\overset{k_1(slow)}{\longrightarrow}} Cu^{+} \qquad (6.5)$$

$$Cu^{+} + e^{-} \underset{\longleftarrow}{\overset{k_2(fast)}{\longrightarrow}} Cu \qquad (6.6)$$

Here k_1 is the rate of reaction of reduction of cupric to cuprous ions and k_2 is the rate of reaction of reduction of cuprous ions to copper and its incorporation into the copper lattice. According to Brown and Thirsk, reduction of cupric ions to cuprous ions is slower than reduction and incorporation into copper lattice at applied potentials less than 10 mV [133]. Similar observations have been made in other studies found in literature [132, 134]. Hence, the reduction of cupric ions to cuprous ions can be assumed to be the rate determining step in copper electrodeposition. It should be noted that some studies have reported that the rate determining step changes throughout the electrodeposition process [68]. For a multistep electrochemical reaction where first step in the mechanism is the rate determining step [65]:

$$i_{0,rds} = FAk_{0,rds}C_0 e^{-\alpha f(E_{eq}-E^{0'}_{rds})} \quad (6.7)$$

$$i_0 = nFAk_0(C_{R'})_{eq} e^{-(\alpha-1) f(E_{eq}-E^{0'}_{rds})} \quad (6.8)$$

where, n is the number of electrons in the overall reaction, F is the Faraday's constant, A is the area of the electrode. $i_{0,rds}$ and i_0 are the exchange current of the rate determining electron transfer and overall reaction respectively. $k_{0,rds}$ and k_0 are the rate constants of the rate determining step and overall reaction respectively. C_0 and $C_{R'}$ are the initial concentration of cupric ions and concentration of the intermediate cuprous ions in equation (1.6). E_{eq} and $E^{0'}_{rds}$ are the equilibrium potential and formal potential of the electrolyte. The overall reaction in equations (6.5) and (6.6) involves two electrons and the 2 electrons are exchanged in the overall reaction. With the contribution of the post-reaction we can write overall exchange current in terms of C_R as:

$$i_0 = nFAk_{0,rds}C_R e^{-(\alpha-1) f(E_{eq}-E^{0'}_{rds})} e^{n' f(E_{eq}-E^{0'}_{post})} \quad (6.9)$$

where, C_R is the concentration of the final product of equation (1.7). $E^{0'}_{post}$ is the formal potential of the electrolyte consumed in equation (1.7) and n' is the number of electrons consumed in the second step. Multiplying by unity in the form $e^{(n'+\alpha-1) f(E^{0'}-E^{0'})}$ and rearranging, the following can be obtained:

$$i_0 = nFAk_{0,rds} e^{-(\alpha-1) f(E^{0'}_{rds}-E^{0'})} e^{n' f(E^{0'}_{post}-E^{0'})} C_R e^{-(n'+\alpha-1) f(E_{eq}-E^{0'})} \quad (6.10)$$

where $E^{0'}$ is the formal potential of the electrolyte for the overall reaction in equations (6.5) and (6.6). This reduces to:

$$i_0 = nFAk_{0,rds} e^{(\alpha-1) f(E^{0'}_{rds}-E^{0'})} e^{n' f(E^{0'}_{post}-E^{0'})} C_R e^{-(n'+\alpha-1) f(E_{eq}-E^{0'})} \quad (6.11)$$

The apparent rate constant can be given by:

$$k_{0,app} = k_{0,rds} e^{(\alpha-1) f (E^{0'}_{rds} - E^{0'})} e^{n' f (E^{0'}_{post} - E^{0'})} \quad (6.12)$$

The exchange current can be represented as [65]:

$$i_0 = nFAk_{0,app} C_0^{(1-(n'+\alpha-1)/n} C_R^{(n'+\alpha-1)/n} \quad (6.13)$$

Taking log of both sides:

$$\log i_0 = \log nFAk_{0,app} + ((1-(n'+\alpha-1)/n) \log C_0 + ((n'+\alpha-1)/n) \log C_R \quad (6.14)$$

In the present case, it reduces to:

$$\log i_0 = \log nFAk_{0,app} + ((1-(n'+\alpha-1)/n) \log C_0 \quad (6.15)$$

Figure 6.7 shows a plot of Log(I_0) vs. Log(C_0) and the equation of the line for the linear fit. The equation of this line was compared with equation (6.15 with n = 2 and n' = 1. The slope of the linear fit was used to arrive at a value of α of 0.54 for the cathodic part of the Tafel polarization curve and value of 1.40 was obtained for the anodic part of the curve. The y-intercept of the cathodic part was used to arrive at following equation for copper reduction:

$$10^{i_{0,\text{y-intercept}}} = nFAk_{0,app} \quad (6.16)$$

Using, n = 2 and F = 96485 C/mol, the equation was solved for $k_{0,app}$. A value of 5×10^{-6} m/s was obtained and was used for solving the mathematical model in chapter 3.

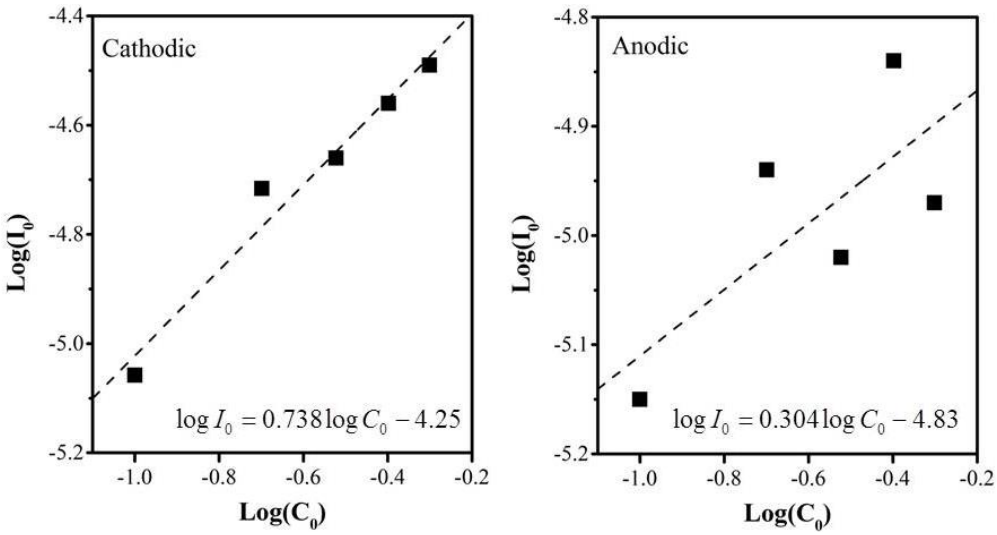

Figure 6.7: Plots of $Log(I_0)$ vs. $Log(C_0)$ for copper electrodeposition in anodic and cathodic regions of the Tafel polarization curve of copper sulfate solutions described in chapter 5.

According to Mattsson and Bockris, the value of transfer coefficient for copper reduction in cathodic and anodic parts of the copper redox couple is 0.5 and 1.5 which is very close to the the values obtained here. Although the transfer coefficient does not have a large impact on the electrodeposition process in this study, it allows us to confirm the value of reaction rate obtained here [132].

6.4. Flow-through electrodeposition

Flow-through electrodeposition was carried out under conditions of high electrolyte conductivity and low applied current. The goal of flow through electrolysis was to achieve complete filling of the pore network in each of the samples used to for electrochemical infiltration. According to the equations developed and solved in chapter 3, it was realized that a porous medium has a better chance of being filled electrochemically when the applied electrical current for electrodeposition

and electrical conductivity of the porous medium being infiltrated is low. Similarly, a high conductivity electrolyte is required to give a more favorable distribution of electrochemical reactions in a porous medium. According to Neman and Tobias, the sum of reciprocals of the electrical conductivity of both the electrolyte and the porous electrode is the most important factor for achieving uniform current distribution in the electrode [34].

A downside of low electrical conductivity of the porous media in the flow-through electrochemical infiltration is the inability to apply an electrical current at a reasonable potential. Due to the absence of a current collector, the electrons required for the electrochemical reduction of copper are solely supplied by the porous media itself. As the electrical conductivity of the electrode matrix is increased, the conductivity of the electrolyte is required to be increased according to the mathematical model in chapter 3 which requires addition of the supporting electrolyte. However, the supporting electrolyte, H_2SO_4, limits the solubility of the primary electrolyte, $CuSO_4$, due to common ion effect.

The maximum electrical current that can be applied in an electrochemical system is dependent on the concentration of the primary electrolyte or $CuSO_4$. The mathematical equation representing the mass transfer limited current is [65]:

$$i_{l,c} = nFAk_m C_0 \qquad (6.17)$$

Here $i_{l,c}$ is the limiting current, k_m is the mass transfer coefficient of copper ions inside the porous media and C_0 is the concentration of the copper ions in the solution. Since the concentration of $CuSO_4$ and consequently, Cu^{2+} ions is very low the current is applied during the electrochemical infiltration process. Therefore, a very small current of 10 mA can be applied during the electrolysis process. According to Faraday's law of electrolysis [65]:

$$m = \frac{I_{app} \cdot t \cdot M}{nF} \qquad (6.18)$$

For a 1 cm^3 porous part with 50% porosity, about 4.29g of copper is required to completely fill the pore network. From equation (6.18), the time required to completely densify such a part using electrodeposition is greater than 362 hours. Thus, a small applied current limits the usage of such a technique for densification purposes. However, there are other areas of application for such a process, especially in electrodeposition of protective coatings and catalysts into porous electrodes for battery applications [88].

6.5. Electrodeposition of copper to make composite coatings

Electrodeposition of copper into thin porous parts supported on a copper-110 alloy resulted in near complete densification of the porous parts. As the pore network occupied more than 60% of the volume in the laser sintered parts, filling of this network with copper lead to formation of copper matrix composite coatings. Since a current collector was used to support the porous media, it was possible to use porous media with low electrical conductivity, which allowed for electrodeposition current of the order of 50 mA- 200 mA. The experiments conducted on graphite felt showed incomplete filing of the pores, with almost 31% of the porosity occupied by the copper. This is due to high electrical conductivity of the graphite felt, which resulted in fast removal of copper ions from the solution in the direction of flow of the electrolyte.

6.5.1. Cu^{2+} cross-over through Nafion®

The absorption spectra show that the amount of copper diffused to the anodic section decreased as the flow rate of the electrolyte through the porous media was increased. It was also found that the surfactant, Triton X-100 lead to further decrease in the cross-over of the copper ions. Figure

6.8 shows the mass transfer coefficient of copper ions through the nafion membrane. The mass transfer coefficient of copper ions through the nafion membrane is about 70% lower when Triton X-100 is present in the solution. These results indicated that the presence of surfactant not only improves the wettability of a porous electrode, but also reduces the Cu^{2+} cross-over significantly.

The structure of Triton X-100 is shown in figure 6.9. Triton X-100 is a nonionic surfactant that has a hydrophilic polyethylene oxide chain (on average it has 9.5 ethylene oxide units) and an aromatic hydrocarbon lipophilic or hydrophobic group. The hydrocarbon group is a 4-(1,1,3,3-tetramethylbutyl)-phenyl group. The reduction in Cu^{2+} diffusion can be attributed to formation of metal ion complexes with the surfactant molecules. The complexation of metal ions such as Ni^{2+} and Co^{2+} in micellar media has been used in separation of heavy metal ions in a mixture. Hebrant and co-workers have reported an linear increase in the rate of complex formation between Cu^{2+} and Triton X-100 with an increase in the concentration of Cu^{2+} ions [135]. In their study, the metal ions were present in large excess over the surfactant. However no correlation was established between the number of ethylene oxide groups and metal ions. Paradies reported that the size of a Triton X-100 micelle could range from 20Å to 105Å using small angle X-ray scattering [122]. The pore size of Nafion-117 membrane can range from 30Å to 80Å [136]. Since the size of a micelle is comparable to the size of the membrane, cross-over of the Cu^{2+} ion through Nafion is limited. The increase in viscosity of the catholyte due to the addition of the surfactant can also be contributing factor in the decrease in the Cu^{2+} ion cross-over [137].

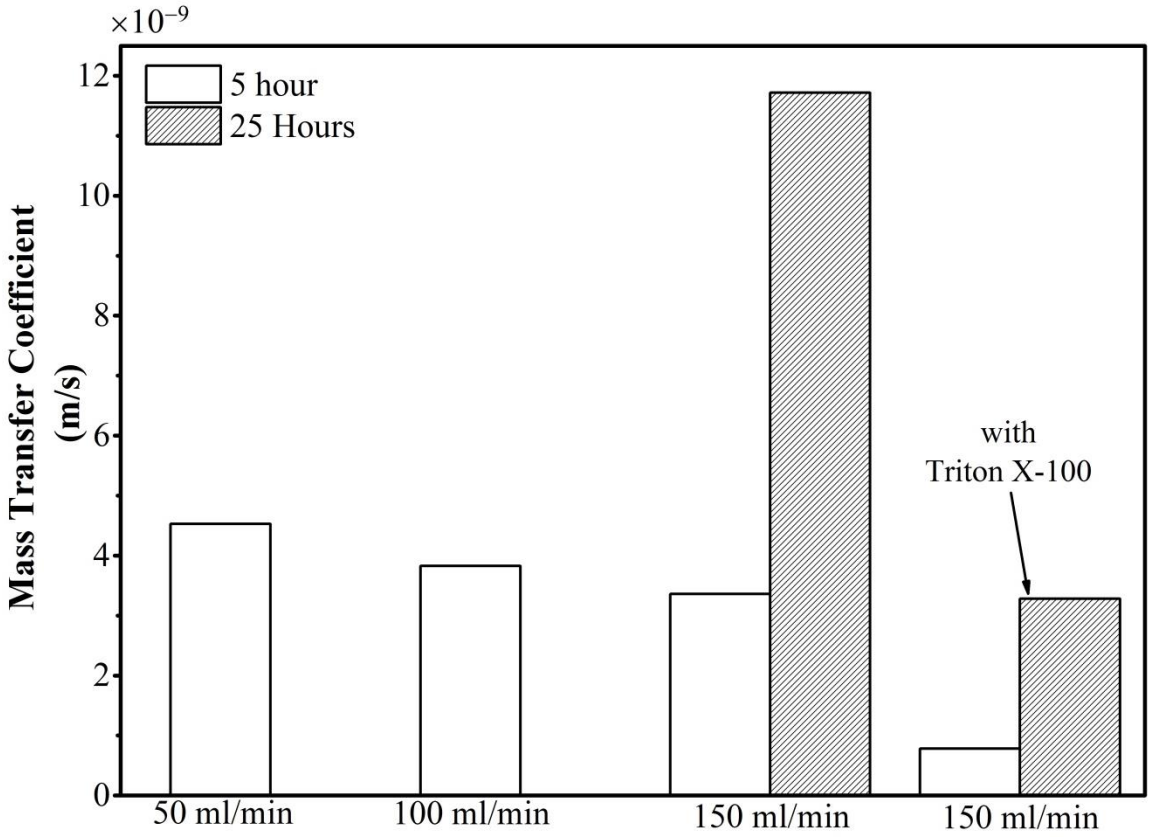

Figure 6.8: Mass transfer coefficient of copper ions through the Nafion membrane calculated over a period of 5 hours and 25 hours

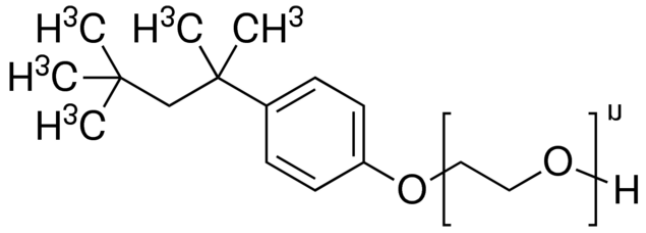

Figure 6.9: Structure of Triton X-100.

6.5.2. Microstructure and X-ray diffraction

The electrical conductivity of the porous media had a direct effect on the electrical potential required to obtain a particular electrodeposition current. As the electrical conductivity of the

porous media was increased, the potential required to obtain a particular current was lower. Direct comparison of applied current can be made in the case of laser sintered graphite and silicon carbide, since it can be assumed that the specific surface area is of the same order for both. The potential required to achieve same total current in the case where porous template is made of graphite is lower. This is because graphite is electrically conductive and the area of the electrode available to transfer electrons to the copper ions in the reduction reaction is higher. Although carbon fibers are present in laser sintered silicon carbide, the percolation threshold is not reached, and the porous template as a whole has poor electrical conductivity. Hence, more electrons per second are transferred to the Cu^{2+} ions for the same potential in laser sintered graphite compared to laser sintered silicon carbide.

The density of the composite coatings was also measured using "free standing" coatings. As expected, the density of the composite coatings showed a dependence on electrical conductivity of the porous media. Almost completely dense coatings were obtained when electrolytic infiltration was carried out inside Nomex felt. This is because the felt had negligible electrical conductivity and very high pore volume fraction. When laser sintered porous silicon carbide was used as the porous media for infiltration experiments, it was observed that up to 97% dense coatings could be prepared at lower applied currents (~50 mA). As the applied current was increased, there was drop in the density of the coatings obtained. For laser sintered graphite, it was observed that complete densification was not possible. However, 89% dense coatings could be obtained at an applied current of 50 mA.

According to mathematical model presented in chapter 3, lower electrical conductivity and high porosity in the porous media gives the most favorable distribution of reaction current. However, if the electrical conductivity of the porous media is really low and a current collector can be

placed in the electrodeposition chamber, the increase in applied current leads to an increase in te reaction current density close to the current collector [34]. This allows “bottom up” filling of the pore network for a porous media with poor electrical conductivity. The electrodeposition of copper takes place around the individual particles or fibers of the porous media until these are completely surrounded by a copper matrix. Copper-SiC and copper-Nomex composites have higher density because the porous media does not take part in the reduction reaction. Hence, the pores at the geometric surface are not closed, and a “bottom-up” fill can always be achieved. On the other hand, due to conductive nature of porous media such as stainless steel mesh and laser sintered graphite, the deposition of copper can lead to closure of pores and prevent the fresh electrolyte from accessing the internal pore network. This leads to a higher porosity in the composite coatings.

In the optical micrographs shown for copper-graphite and copper-SiC coatings, it was observed that the particles in the composites do not form an interconnected network. This is consistent with the micrographs reported by Wohlert for laser sintered parts infiltrated with magnesium using pressure-less infiltration methods [55]. During the mechanical grinding and polishing processes, it was realized that the particles embedded in the copper matrix tend to come out of the matrix. This is significant in the copper-SiC composites and is also seen in some spots in copper-graphite. The measurement of grain size of the copper grains in the composite coatings showed a decrease as the applied current was increased. The grain structure is similar to that of hot rolled copper. The microstructure of the electrodeposited coatings is expected to follow the microstructure of the substrate [138]. However, the grain size depends on the applied current density. As the applied current density is increased, the grain size decreases. This is because at higher current densities nucleation of new copper grains is much faster than the growth of the

copper grains [139, 140]. Since the applied current density in general should be higher for copper-SiC compared to copper-graphite, the grain size in general is larger. It was also observed that even though the electrical conductivity of the Nomex felt is lower than laser sintered silicon carbide, the grain size of electrodeposited copper was higher. This can be explained on the basis of total area available for electron transfer. Since Nomex felt has a higher porosity than laser sintered silicon carbide, more area of the current collector can be exposed to the electrolyte which provides a higher area for electron transfer.

6.5.3. Thermal properties

Thermal conductivity of copper matrix composite coatings was measured using "free standing coatings". It was observed that the thermal conductivity was affected highly by the density of coatings. In copper matrix composites formed by electrolytic infiltration of copper into electrical non-conducting porous media, thermal conductivity was higher.

Thermal conductivity of a composite material can be represented using Maxwell-Eucken equation [25]:

$$K_c = \frac{K_m V_m + K_f V_f \dfrac{3K_m}{2K_m + K_f}}{V_m + V_f \dfrac{3K_m}{2K_m + K_f}} \qquad (6.19)$$

where, K_c is the thermal conductivity of the composite, K_m and K_f are the thermal conductivities of the matrix and the filler respectively and V_m and V_f are the volume fraction of the matrix and filler respectively.

Figure 6.10 shows a comparison of thermal conductivity calculated using the Maxwell-Eucken equation and experimental values of thermal conductivity values obtained in this study for

composite coatings produced at 50 mA. It was observed that the thermal conductivity predicted by this equation had a higher value compared to the measured values except copper-SS316 coatings. This can be attributed to the presence of porosities in the samples and the nature of the filler.

There is a very small difference in the thermal conductivity of the samples obtained for the composite coating obtained under different applied currents. We attribute this difference to the difference in the density of these composites. Copper-Nomex coatings showed a thermal conductivity close to the thermal conductivity of copper. The thermal conductivity of copper is much higher than copper-graphite and copper-SiC. On the other hand copper-graphite has much lower thermal conductivity compared to copper-SiC due to a higher pore volume fraction in copper-graphite as well as a higher percentage of cross-linked phenolic resin.

Although the grain size of the electrodeposited copper changed with the potential at which electrodeposition was carried out, the grain size was still large compare to the phonon and electron mean free path. Studies conducted on scattering of electrons and phonons due to grain boundaries show that at high temperatures, electron mean free path is of the order of a few nanometers, which is very small compared to the grain size of the copper matrix in the coatings [141, 142]. Consequently, the thermal conductivity values obtained for these coatings should not show appreciable difference with the change in applied current and grain size of the copper matrix.

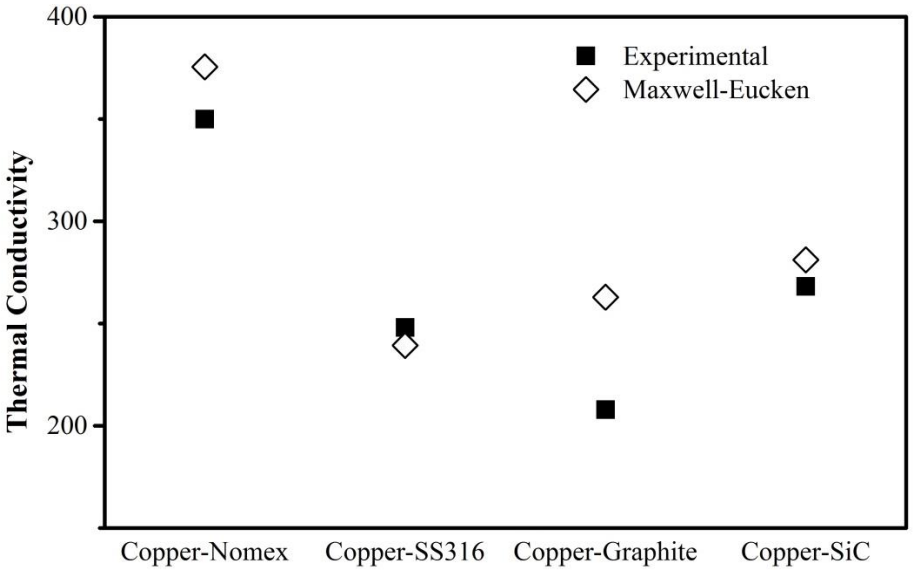

Figure 6.10: Comparison of experimentally measured values of thermal conductivity (at 50^{o}C) of composite coatings produced at applied current of 50 mA with Maxwell-Eucken equation.

6.5.4. Tribological properties

The dynamic coefficient of friction for all the composite coatings was lower than copper-110 alloy in figures 5.34-5.36 shown in chapter 5. This can be attributed to the increased hardness of the composite coatings due to the presence of reinforcements as well as due to the fine grain structure of the copper matrix formed during electrodeposition. In case of reinforcements such as nomex felt and laser sintered graphite, the self-lubricating effect of such reinforcements also affects the coefficient of friction. The SEM images of the wear tracks provide further explanation of the wear behavior of these composites.

Figures 6.11-6.15 shows SEM images of the wear tracks formed during the dry sliding wear of the coatings at different sliding speeds. From the wear tracks, it can be concluded that the wear in all the specimens occurs via an adhesive mechanism. Since the hardness of alumina is much

higher than the hardness of all the specimens tested in this study, it is reasonable to assume that material transfer would mainly occur from the coatings to the alumina ball. Any fragment of material that is transferred to the alumina ball is plastically deformed during the sliding action of the tribometer. This leads to the evolution of the transferred material into a plate-like morphology and ploughing in the wear tracks. Owing to the cyclic loading, this transferred layer is detached from the alumina ball and sticks to the wear track.

In the case of copper-110 alloy (figure 6.11), copper-Nomex (figure 6.12), copper-SS316 (Figure 6.13) and Cu–SiC composite (figure 6.15), the SEM images also show streaks parallel to the direction of motion of the tribometer arm. This reflects action of an abrasive wear mechanism in these coatings. During the sliding wear of copper-110 alloy, copper-Nomex and copper-SS316, the metal particles are detached from the surface and are work hardened during the sliding action of the pin and assist in wear. Similarly, the SiC particles in case of the copper–SiC coatings assist in wear as well.

SEM images of the wear tracks of copper–graphite coatings (figure 6.15) show some plate-like features. Any microstructural features formed during the wear of copper–graphite coatings were completely covered by graphite, which, due to its self-lubricating nature, inhibited further abrasive wear. Wear rate was lowest for the coatings with silicon carbide particles and carbon fibers and highest for copper-110 alloy. This is attributed to lower coefficient of friction and higher hardness of copper–SiC coatings. The electrodeposited copper–graphite coatings showed a lower wear rate than the copper-110 alloy, even though it had a lower hardness and density comparatively. Since graphite is a very effective lubricant, the presence of graphite in the composite coatings significantly improves the wear resistance.

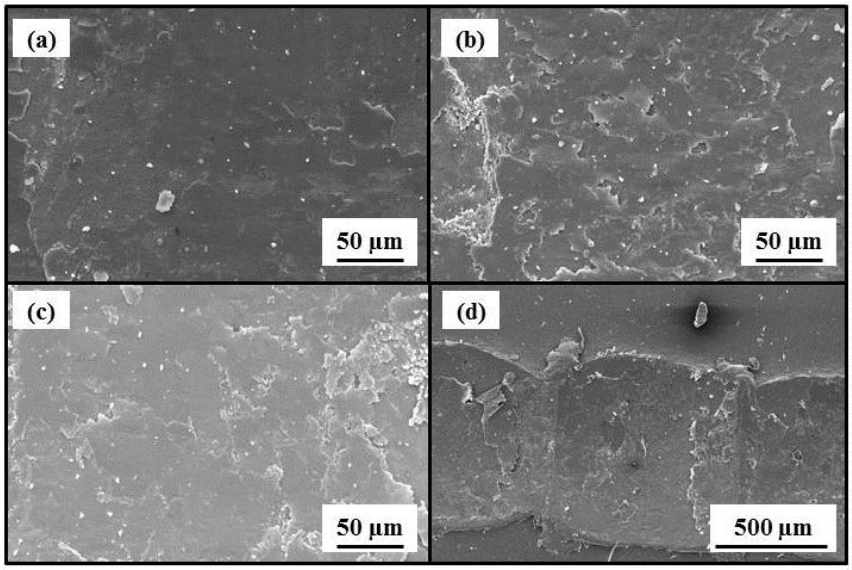

Figure 6.11: Wear tracks formed by dry sliding wear of copper-110 alloy (a) at 1200 mm/min, (b) 1800 mm/min, (c) 2400 mm/min and (d) ploughing wear at 2400 mm/min

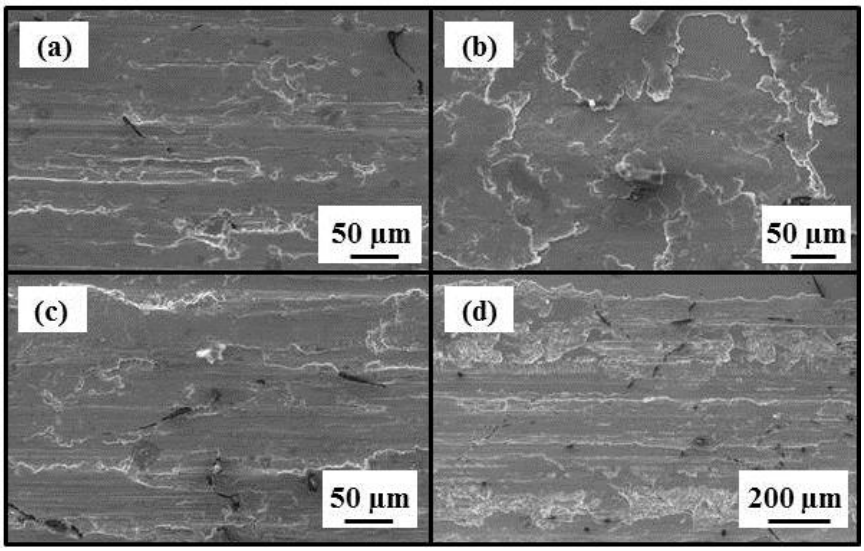

Figure 6.12: Wear tracks formed by dry sliding wear of copper-nomex coatings (a) at 1200 mm/min, (b) 1800 mm/min, (c) 2400 mm/min and (d) ploughing wear at 2400 mm/min

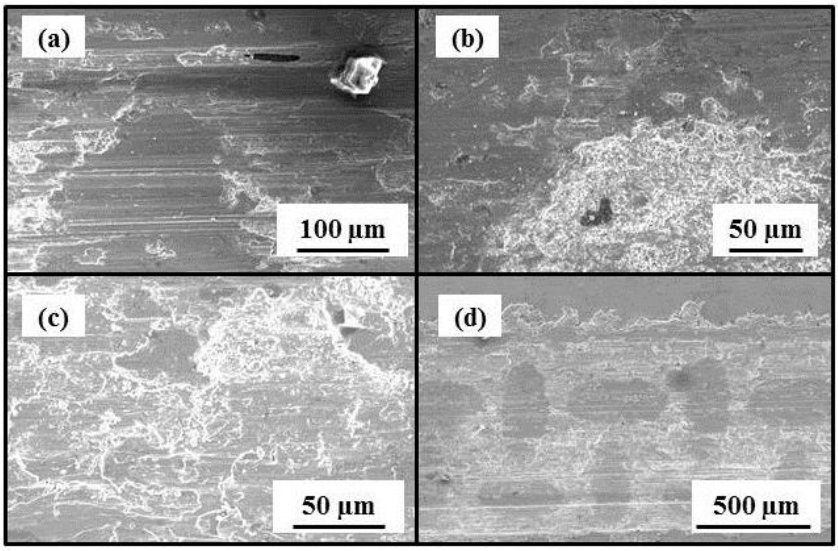

Figure 6.13: Wear tracks formed by dry sliding wear of copper-SS316 coatings (a) at 1200 mm/min, (b) 1800 mm/min, (c) 2400 mm/min and (d) ploughing wear at 2400 mm/min

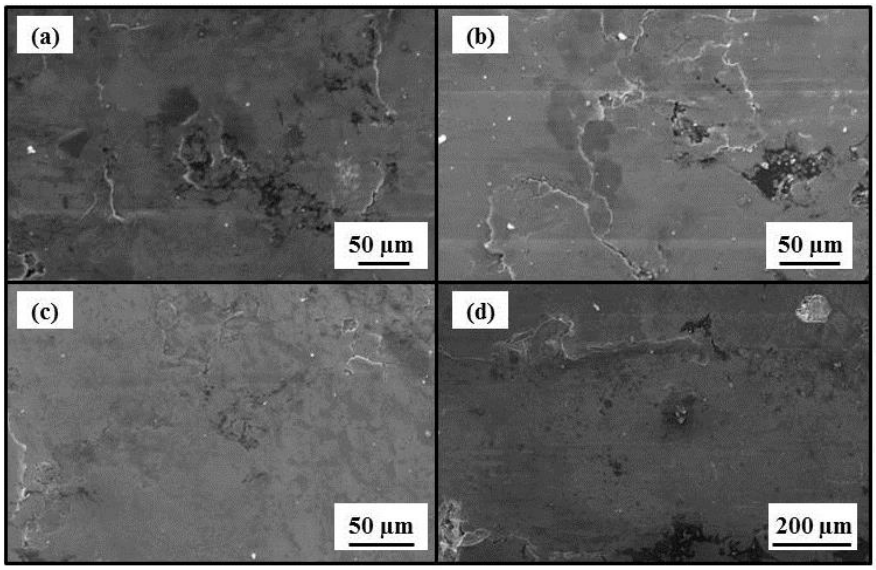

Figure 6.14: Wear tracks formed by dry sliding wear of copper-graphite coatings (a) at 1200 mm/min, (b) 1800 mm/min, (c) 2400 mm/min and (d) ploughing wear at 2400 mm/min

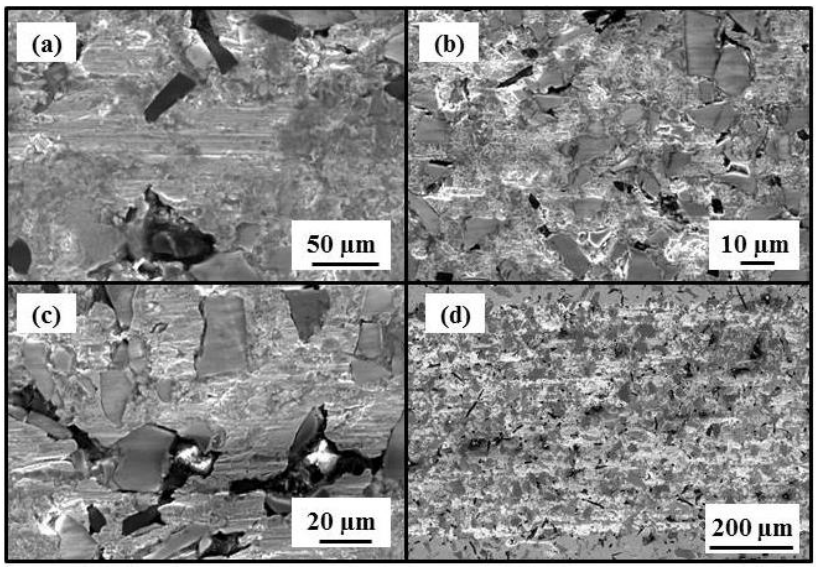

Figure 6.15: Wear tracks formed by dry sliding wear of copper-SiC coatings (a) at 1200 mm/min, (b) 1800 mm/min, (c) 2400 mm/min and (d) ploughing wear at 2400 mm/min

Since wear occurs between two surfaces sliding against each other, some wear was expected in the alumina balls. Unfortunately, the data for wear on alumina balls used for wear testing is not available. However, it was possible to characterize the wear tracks using EDS shown in figures 6.16-6.20. It was found that all the materials except copper-graphite coatings showed the presence of aluminum Kα peaks. This is consistent with the observation that excellent lubrication was achieved in the copper-graphite composite coatings. It can be safely assumed that the wear of copper-graphite composites occurred mainly through adhesive mechanism, wherein the graphite attaches with the alumina ball to form a layer of graphite on the alumina ball.

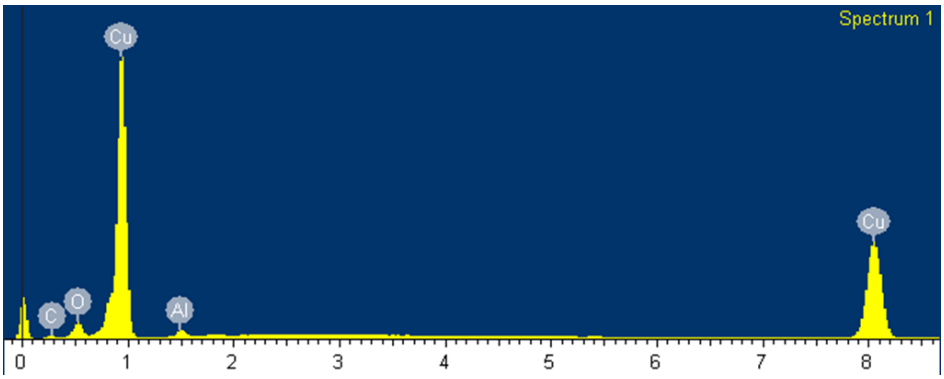

Figure 6.16: EDS plots of copper 110 wear track shown in figure 6.11(c)

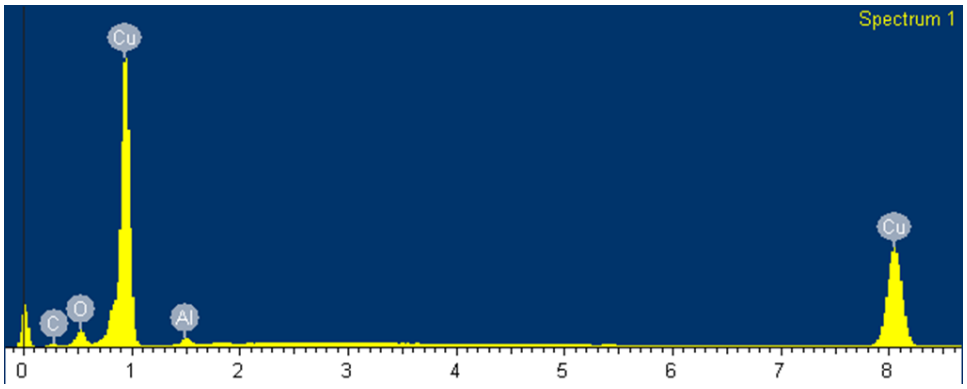

Figure 6.17: EDS plots of copper-nomex wear track shown in figure 6.12(c)

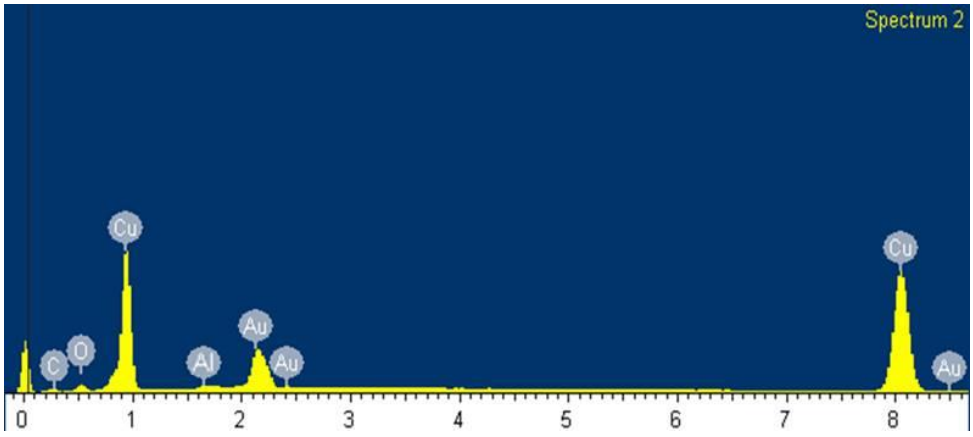

Figure 6.18: EDS plots of copper-SS316 wear track shown in figure 6.13(c). Au peaks are present due to sputtered gold coating on the specimen.

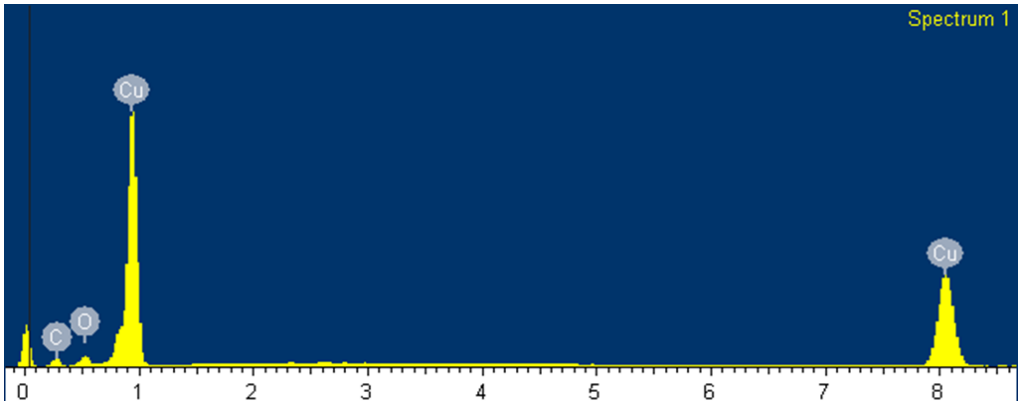

Figure 6.19: EDS plots of copper-graphite wear track shown in figure 6.14(c)

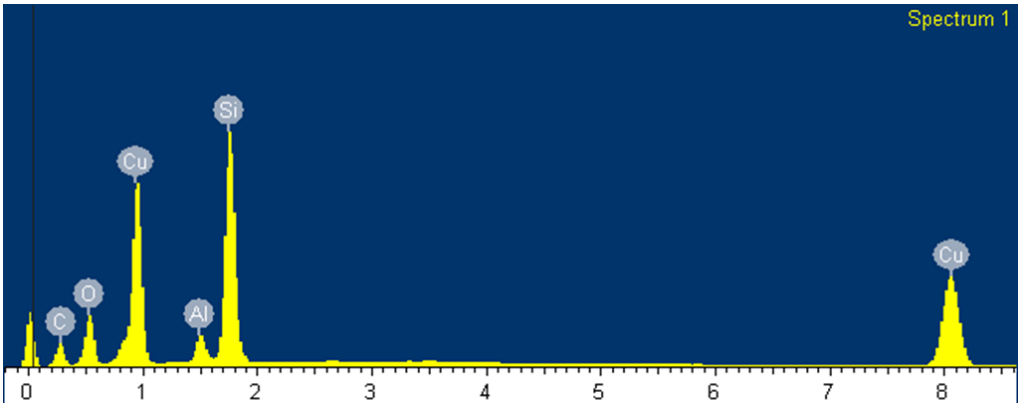

Figure 6.20: EDS plots of copper-SiC wear track shown in figure 6.15(c)

Chapter 7: Conclusions

7.1. Conclusions of the present work

This chapter summarizes the conclusions of the present work. The process of indirect laser sintering can be used to produce porous coatings on substrates, which can be electrochemically infiltrated with a metal to produce metal matrix composites. The route described in the present work is simple and requires control over processing parameters such as applied current and applied electrical potential. Based on the experimental results obtained in the research work, the following conclusions can be drawn:

1) A mathematical model was used to compute the current density distribution in porous media. The effect of electrode and electrolyte properties on current distribution was determined. It was found that the most favorable conditions for electrolytic infiltration are present when a highly conductive electrolyte is used along with a low conductivity porous electrode. It was also found that electrolytic infiltration was more conducive when the applied current for electrodeposition is small and thin porous preforms were used with a current collector.
2) An existing process for fabricating graphite and silicon carbide parts using a mixture of the corresponding powders with a phenolic resin as the binder was used to produce parts. These parts were used to determine the effect laser processing parameters and binder burnout temperature on pore volume fraction and electrical conductivity of the laser sintered parts. It was observed that increase in layer thickness and burnout temperature led to an increase in the pore volume fraction. It was also observed that an increase in the

burnout temperature led to an increase in the electrical conductivity of the laser sintered parts.

3) Various electrolyte properties such as electrical conductivity, viscosity and contact angle with graphite and silicon carbide were determined. It was found that the electrical conductivity of the aqueous $CuSO_4/H_2SO_4$ electrolytes increased with the increase in H_2SO_4 concentration and decrease in $CuSO_4$ concentration. The viscosity of the electrolytes increased with an increase in the concentration of both $CuSO_4$ and H_2SO_4. A non-ionic surfactant, Triton X-100 was added to the electrolytes to improve wettability of silicon carbide and graphite with the electrolytes. It was found that although addition of a surfactant improves the wettability, it also leads to an increase in the viscosity of the electrolytes. It was found that 1 ml/l of the electrolyte was the optimum quantity desired in the electrolyte required to fill the porous preforms.
4) Electrochemical methods of linear potential scans and Tafel polarization were used to determine the constants such as diffusivity of copper ions and rate constant for copper electrodeposition. It was observed that the coefficient of diffusion of copper in the electrolytes in this study was lower, possibly due to the presence of a surfactant. Slow potential scans at 10mV/s were carried out in a stirred solution to determine the difference in hydrogen evolution and copper reduction. This allowed determination of electrical potentials at which copper electrodeposition could be carried out with high current efficiency.
5) Electrodeposition of copper was carried out in free standing porous preforms as well as thin porous preforms supported on a copper-110 alloy plate. It was found that it was not possible to achieve complete density when free standing porous preforms were used.

However, highly dense composite coatings were achieved when thin porous preforms were electrochemically infiltrated with copper. It was found that it was easier to perform electrolytic infiltration into preforms with low electrical conductivity. It was also found that unlike the conventional methods of electrolytic codeposition of composites, it was possible to incorporate fibers into the composite coatings.

6) Some interesting observations were made on diffusion of copper ions though a Nafion membrane. It was found that increase in the flow rate of electrolyte during electrodeposition processing led to some decrease in the Nafion cross-over of copper ions. However, when a surfactant was added to the electrolyte, it was observed that the cross-over of copper-ions decreased by almost 70%.
7) It was found that the grain size of the electrodeposited copper matrix decreased as the applied current was increased. A survey of literature revealed that an increase in the applied current leads to a decrease in grain size because of a higher nucleation rate of new grains compared to growth.
8) Thermal conductivity of the composites showed dependence on the electrical current at which the copper was electrodeposited inside the porous preform. It was found that even though the grain size of the copper matrix decreased with an increase in applied current, a small enough grain size was never achieved that was comparable to the electron mean free path. Since copper is an electronic conductor of heat, thermal conductivity was unaffected by the grain size. However, a decrease in thermal conductivity of the composites was observed due to the decrease in density of the copper matrix at higher deposition currents.

9) It was found that the wear rate and coefficient of friction of copper matrix composites manufactured in this work were lower than values for the copper-110 alloy. It was found that addition of graphite led to a very low coefficient of friction while addition of silicon carbide led to a very low wear rate in the copper matrix composites.

7.2. Future work

The application of the route for producing metal matrix composite coatings to functional parts, especially electrical contacts, requires determination of a few properties. These are listed in the following:

1) As part of the present work, electrical conductivity of the composite coatings was determined using a four point probe method. The values obtained are shown in figure 7.1.

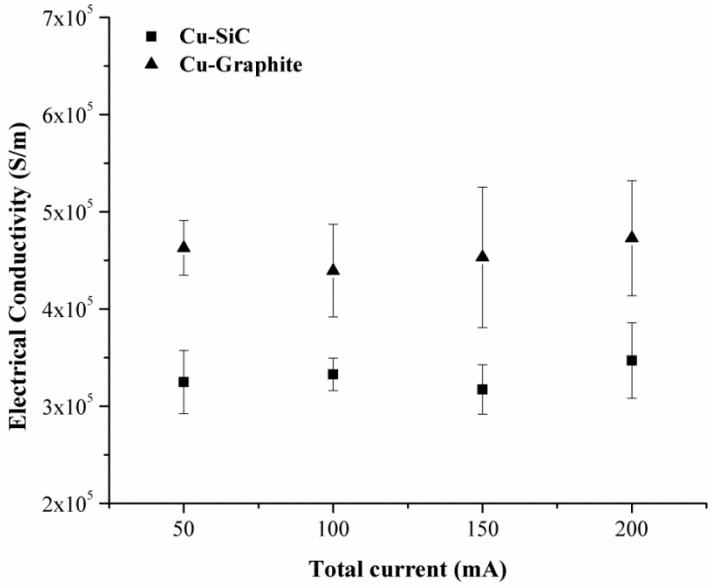

Figure 7.1: Electrical conductivity of copper-SiC and copper-graphite composites fabricated by electrolytic infiltration at different electrodeposition currents

It was observed that the measurements were not reliable enough to be held significant. This is mainly because the four probe method only measures bulk resistivity as a function

of the sheet resistivity of the coatings. However, since porosities are present in almost all of the coatings, the values obtained here are not representative of the actual bulk resistivity of the coatings. Better electrical conductivity measurement systems need to be used for measurement of such a composite.

It is also required to conduct wear testing using different sliding media at higher loads and speeds with the application of an electrical current.

2) The coating-substrate interface in the composite coatings consists of several phases such as the residue of the phenolic binder, reinforcement particles and porosities. The presence of these can be detrimental to the adhesion of the coatings with the substrate. Hence, it is required to quantify the effect of electrodeposition parameters on the coating integrity, toughness and strength of adhesion with the substrate.
3) It is required to extend the present work to develop coatings for more complex shapes such as machining tools.

References

1. Beaman, J.J., et al., *Solid freeform fabrication: a new direction in manufacturing.* Kluwer Academic Publishers, Norwell, MA, 1997. **2061**: p. 25-49.
2. Bourell, D.L., *Materials issues in rapid manufacturing.* Rapid manufacturing: An industrial revolution for the digital age, 2006: p. 81-102.
3. Deckard, C.R., *Part generation by layerwise selective sintering*. 1986.
4. Bourell, D.L., et al., *Computer-controlled laser*. 1990, Google Patents.
5. Alayavalli, K. and D.L. Bourell, *Fabrication of modified graphite bipolar plates by indirect selective laser sintering (SLS) for direct methanol fuel cells.* Rapid prototyping journal, 2010. **16**(4): p. 268-274.
6. Bhat, A. and D. Bourell, *Tribological properties of metal matrix composite coatings produced by electrodeposition of copper.* Materials Science and Technology, 2014.
7. Aghajanian, M., et al., *The fabrication of metal matrix composites by a pressureless infiltration technique.* Journal of Materials Science, 1991. **26**(2): p. 447-454.
8. Beffort, O., S. Vaucher, and F. Khalid, *On the thermal and chemical stability of diamond during processing of Al/diamond composites by liquid metal infiltration (squeeze casting).* Diamond and related materials, 2004. **13**(10): p. 1834-1843.
9. Besmann, T., et al., *Vapor-phase fabrication and properties of continuous-filament ceramic composites.* Science, 1991. **253**(5024): p. 1104-1109.
10. Bhat, A., et al., *Carbon nanotube reinforced Cu–10Sn alloy composites: Mechanical and thermal properties.* Materials Science and Engineering: A, 2011. **528**(22): p. 6727-6732.
11. Chedru, M., et al., *Aluminium-aluminium nitride composites fabricated by melt infiltration under pressure.* Journal of microscopy, 1999. **196**(2): p. 103-112.

12. Cook, A. and P. Werner, *Pressure infiltration casting of metal matrix composites.* Materials Science and Engineering: A, 1991. **144**(1): p. 189-206.

13. Cooper, G., *Forming processes for metalmatrix composites.* Composites, 1970. **1**(3): p. 153-159.

14. Demir, A. and N. Altinkok, *Effect of gas pressure infiltration on microstructure and bending strength of porous Al 2 O 3/SiC-reinforced aluminium matrix composites.* Composites science and technology, 2004. **64**(13): p. 2067-2074.

15. Etter, T., et al., *Physical properties of graphite/aluminium composites produced by gas pressure infiltration method.* Carbon, 2003. **41**(5): p. 1017-1024.

16. Evans, R.S., et al., *Rapid manufacturing of silicon carbide composites.* Rapid Prototyping Journal, 2005. **11**(1): p. 37-40.

17. Zahedi, A., et al., *The effect of processing conditions on the microstructure and impact behavior of melt infiltrated Al/SiCp composites.* Ceramics International, 2011. **37**(8): p. 3335-3341.

18. Balla, V.K., et al., *Laser processed TiN reinforced Ti6Al4V composite coatings.* Journal of the Mechanical Behavior of Biomedical Materials, 2012. **6**(0): p. 9-20.

19. Deuis, R., J. Yellup, and C. Subramanian, *Metal-matrix composite coatings by PTA surfacing.* Composites Science and Technology, 1998. **58**(2): p. 299-309.

20. Hovestad, A. and L.J. Janssen, *Electroplating of Metal Matrix Composites by Codeposition of Suspended Particles*, in *Modern Aspects of Electrochemistry*, B.E. Conway, et al., Editors. 2005, Springer US. p. 475-532.

21. Yang, S., M. Zhong, and W. Liu, *TiC particulate composite coating produced in situ by laser cladding.* Materials Science and Engineering: A, 2003. **343**(1): p. 57-62.

22. Zheng, X., M. Huang, and C. Ding, *Bond strength of plasma-sprayed hydroxyapatite/Ti composite coatings.* Biomaterials, 2000. **21**(8): p. 841-849.

23. Leyland, A., K. Fancey, and A. Matthews, *Plasma nitriding in a low pressure triode discharge to provide improvements in adhesion and load support for wear resistant coatings.* Surface Engineering, 1991. **7**(3): p. 207-215.

24. Wang, Q., et al., *The influence of ceramic particles on bond strength of cold spray composite coatings on AZ91 alloy substrate.* Surface and Coatings Technology, 2010. **205**(1): p. 50-56.

25. BHAT, A., *MWCNT REINFORCED METAL MATRIX COMPOSITES USING LENS TM: CASE STUDIES ON MWCNT-BRONZE AND MWCNT-Al-12% Si*. 2010, WASHINGTON STATE UNIVERSITY.

26. Low, C., R. Wills, and F. Walsh, *Electrodeposition of composite coatings containing nanoparticles in a metal deposit.* Surface and Coatings Technology, 2006. **201**(1): p. 371-383.

27. Hutchings, I., *Tribological properties of metal matrix composites.* Materials science and technology, 1994. **10**(6): p. 513-517.

28. Walsh, F. and C. Ponce de Leon, *A review of the electrodeposition of metal matrix composite coatings by inclusion of particles in a metal layer: an established and diversifying technology.* Transactions of the IMF, 2014. **92**(2): p. 83-98.

29. Bourell, D., et al., *Electrochemical deposition of metal ions in porous laser sintered inter-metallic and ceramic preforms.* Rapid Prototyping Journal, 2011. **17**(3): p. 181-186.

30. Kung, S., et al., *Photolithographically patterned silver nanowire electrodeposition.* Electrochimica Acta, 2010. **55**(27): p. 8074-8080.

31. Hassanin, H., A. Mohammadkhani, and K. Jiang. *Ceramic nanocomposite by electrodeposition of nickel into porous alumina matrix*. in *Nanotechnology (IEEE-NANO), 2012 12th IEEE Conference on*. 2012. IEEE.

32. Rumpf, K., et al., *Transition metals specifically electrodeposited into porous silicon.* physica status solidi (c), 2009. **6**(7): p. 1592-1595.

33. Trainham, J.A. and J. Newman, *A Flow-Through Porous Electrode Model: Application to Metal-Ion Removal from Dilute Streams.* Journal of The Electrochemical Society, 1977. **124**(10): p. 1528-1540.

34. Newman, J.S. and C.W. Tobias, *Theoretical Analysis of Current Distribution in Porous Electrodes.* 1962.

35. Maslii, A., N. Poddubnyi, and A.Z. Medvedev, *Dynamics of the filling of a porous cathode by the deposited metal: Modeling the process and analyzing the case of high cathode conductance and low solution depletion degree.* Russian Journal of Electrochemistry, 2005. **41**(3): p. 294-303.

36. Maslii, A., A.Z. Medvedev, and N. Poddubnyi, *Copper Electrodeposition Dynamics at a Porous Flow-through Electrode.* Russian Journal of Electrochemistry, 2005. **41**(11): p. 1191-1196.

37. Masliy, A., et al., *Modeling of the dynamics of metal deposition inside a flow-through porous electrode with low initial conductivity.* Journal of Electroanalytical Chemistry, 2007. **600**(1): p. 180-190.

38. Maslii, A.I., A.Z. Medvedev, and N.P. Poddubnyi, *Dynamics of metal deposition onto a porous electrode of poor initial conductivity, with the electrode operating in a direct-flow*

regime at high solution flow rates. Russian Journal of Electrochemistry, 2006. **42**(10): p. 1113-1120.

39. Shah, A., M. Watt-Smith, and F. Walsh, *A dynamic performance model for redox-flow batteries involving soluble species.* Electrochimica Acta, 2008. **53**(27): p. 8087-8100.

40. You, D., H. Zhang, and J. Chen, *A simple model for the vanadium redox battery.* Electrochimica Acta, 2009. **54**(27): p. 6827-6836.

41. Alkire, R. and P.K. Ng, *Studies on Flow-By Porous Electrodes Having Perpendicular Directions of Current and Electrolyte Flow*. Journal of the Electrochemical Society, 1977. **124**(8): p. 1220-1227.

42. Agarwala, M., et al., *Direct selective laser sintering of metals.* Rapid Prototyping Journal, 1995. **1**(1): p. 26-36.

43. Gibson, I. and D. Shi, *Material properties and fabrication parameters in selective laser sintering process.* Rapid Prototyping Journal, 1997. **3**(4): p. 129-136.

44. Bhat, A. and D. Bourell, *Electrochemical deposition of metal ions as a low energy alternative to conventional methods.* International Journal of Precision Engineering and Manufacturing, 2013. **14**(6): p. 881-889.

45. Kruth, J.P., et al., *Binding mechanisms in selective laser sintering and selective laser melting.* Rapid Prototyping Journal, 2005. **11**(1): p. 26-36.

46. Vallabhajosyula, P. and D.L. Bourell, *Modeling and production of fully ferrous components by indirect selective laser sintering.* Rapid Prototyping Journal, 2011. **17**(4): p. 262-268.

47. Subramanian, K., et al., *Selective laser sintering of alumina with polymer binders.* Rapid Prototyping Journal, 1995. **1**(2): p. 24-35.

48. Childs, T., C. Hauser, and M. Badrossamay, *Selective laser sintering (melting) of stainless and tool steel powders: experiments and modelling.* Proceedings of the Institution of Mechanical Engineers, Part B: Journal of Engineering Manufacture, 2005. **219**(4): p. 339-357.

49. Alayavalli, K. and D.L. Bourell. *Fabrication of electrically conductive, fluid impermeable direct methanol fuel cell (DMFC) graphite bipolar plates by indirect selective laser sintering (SLS).* in *Nineteenth International Solid Freeform Fabrication Symposium, Austin, Texas, University of Texas at Austin*. 2008.

50. Bourell, D., et al., *Graphite-based indirect laser sintered fuel cell bipolar plates containing carbon fiber additions.* CIRP Annals-Manufacturing Technology, 2011. **60**(1): p. 275-278.

51. Guo, N. and M.C. Leu, *Effect of different graphite materials on the electrical conductivity and flexural strength of bipolar plates fabricated using selective laser sintering.* international journal of hydrogen energy, 2012. **37**(4): p. 3558-3566.

52. Xu, S., et al., *Reaction forming of silicon carbide ceramic using phenolic resin derived porous carbon preform.* Journal of the European Ceramic Society, 2009. **29**(11): p. 2395-2402.

53. Toy, C. and W.D. Scott, *Ceramic-Metal Composite Produced by Melt Infiltration.* Journal of the American Ceramic Society, 1990. **73**(1): p. 97-101.

54. Hillig, W.B., *Making ceramic composites by melt infiltration.* American Ceramic Society Bulletin;(United States), 1994. **73**(4).

55. Wohlert, M. and D. Bourell. *Rapid prototyping of Mg/SiC composites by a combined SLS and pressureless infiltration process*. in *Proc. Solid Freeform Fabrication Symposium*. 1996. University of Texas.

56. Muscat, D., K. Shanker, and R.A. Drew, *Al/TiC composites produced by melt infiltration.* Materials science and technology, 1992. **8**(11): p. 971-976.

57. Vasic, S., et al., *Activation Mechanism and Infiltration Kinetic for Pressureless Melt Infiltration of Ti Activated Al2O3 Preforms by High Melting AlloyThe authors would like to thank Jean-Paul Bourqui (University of Fribourg) for the excellent preparation of the SEM samples and Christoph Neurrurer (University of Fribourg) for the fabrication of in situ activated alloys.* Advanced Engineering Materials, 2009. **11**(8): p. 659.

58. Carreno-Morelli, E., et al., *Processing and characterization of aluminium-based MMCs produced by gas pressure infiltration.* Materials Science and Engineering: A, 1998. **251**(1): p. 48-57.

59. Daoud, A., *Microstructure and tensile properties of 2014 Al alloy reinforced with continuous carbon fibers manufactured by gas pressure infiltration.* Materials Science and Engineering: A, 2005. **391**(1): p. 114-120.

60. Fukunaga, H. and K. Goda, *Fabrication of Fiber Reinforced Metal by Squeeze Casting: Pressurized Infiltration Process of Molten Aluminum to Continuous Glass Fiber Bundle.* Bulletin of JSME, 1984. **27**(228): p. 1245-1250.

61. Ghomashchi, M.R. and A. Vikhrov, *Squeeze casting: an overview.* Journal of Materials Processing Technology, 2000. **101**(1–3): p. 1-9.

62. Michaud, V. and A. Mortensen, *Infiltration processing of fibre reinforced composites: governing phenomena.* Composites Part A: applied science and manufacturing, 2001. **32**(8): p. 981-996.

63. Besmann, T.M., *Chemical Vapor Deposition in the Boron-Carbon-Nitrogen System.* Journal of the American Ceramic Society, 1990. **73**(8): p. 2498-2501.

64. Besmann, T.M. and R.A. Lowden, *Electrolytic production of aluminum*. 1990, Google Patents.

65. Bard, A.J. and L.R. Faulkner, *Electrochemical methods: fundamentals and applications*. Vol. 2. 1980: Wiley New York.

66. Kelly, J.J., C. Tian, and A.C. West, *Leveling and microstructural effects of additives for copper electrodeposition.* Journal of the Electrochemical Society, 1999. **146**(7): p. 2540-2545.

67. Moffat, T., et al., *Superconformal electrodeposition of copper in 500–90 nm features.* Journal of The Electrochemical Society, 2000. **147**(12): p. 4524-4535.

68. Moffat, T., et al., *Superconformal electrodeposition of copper*. Electrochemical and Solid-State Letters, 2001. **4**(4): p. C26-C29.

69. Beica, R., C. Sharbono, and T. Ritzdorf. *Through silicon via copper electrodeposition for 3D integration*. in *Electronic Components and Technology Conference, 2008. ECTC 2008. 58th*. 2008. IEEE.

70. Slade, P.G., *Electrical contacts: principles and applications*. 2013: CRC Press.

71. Silman, H., G. Isserlis, and A. Averill, *Protective and decorative coatings for metals: a wide ranging survey of inorganic and mechanical p rocesses, properties and applications*. 1978: Finishing Publications.

72. Davis, J.R., *Copper and copper alloys*. 2001: ASM international.

73. Stankovic, V.D. and M. Gojo, *Electrodeposited composite coatings of copper with inert, semiconductive and conductive particles.* Surface and Coatings Technology, 1996. **81**(2–3): p. 225-232.

74. Garcia, I., J. Fransaer, and J.P. Celis, *Electrodeposition and sliding wear resistance of nickel composite coatings containing micron and submicron SiC particles.* Surface and Coatings Technology, 2001. **148**(2–3): p. 171-178.

75. Whitten, P.G., G.M. Spinks, and G.G. Wallace, *Mechanical properties of carbon nanotube paper in ionic liquid and aqueous electrolytes.* Carbon, 2005. **43**(9): p. 1891-1896.

76. Hopfe, V., R. Jäckel, and K. Schönfeld, *Laser based coating and modification of carbon fibres: application of industrial lasers to manufacturing of composite materials.* Applied surface science, 1996. **106**: p. 60-66.

77. Kovalchenko, A., et al., *The effect of laser texturing of steel surfaces and speed-load parameters on the transition of lubrication regime from boundary to hydrodynamic.* Tribology Transactions, 2004. **47**(2): p. 299-307.

78. Gladman, T., *Precipitation hardening in metals.* Materials Science and Technology, 1999. **15**(1): p. 30-36.

79. Guerrero, M., et al., *3D hierarchically porous Cu–BiOCl nanocomposite films: one-step electrochemical synthesis, structural characterization and nanomechanical and photoluminescent properties.* Nanoscale, 2013. **5**(24): p. 12542-12550.

80. Miller, W. and F. Humphreys, *Strengthening mechanisms in particulate metal matrix composites.* Scripta metallurgica et materialia, 1991. **25**(1): p. 33-38.

81. Zhang, Z. and D. Chen, *Consideration of Orowan strengthening effect in particulate-reinforced metal matrix nanocomposites: a model for predicting their yield strength.* Scripta Materialia, 2006. **54**(7): p. 1321-1326.

82. .

83. Lancaster, J., *Lubrication by transferred films of solid lubricants.* ASLE transactions, 1965. **8**(2): p. 146-155.

84. Lancaster, J., *Transfer lubrication for high temperatures: a review.* Journal of tribology, 1985. **107**(4): p. 437-443.

85. Bozzini, B., G. Giovannelli, and P. Cavallotti, *An investigation into microstructure and particle distribution of Ni–P/diamond composite thin films.* Journal of Microscopy, 1997. **185**(2): p. 283-291.

86. Apachitei, I., *Synthesis and characterisation of autocatalytic nickel composite coatings on aluminium*. 2001: TU Delft, Delft University of Technology.

87. Hirata, Y., et al., *Synthesis of alumina/nickel composite by electrodeposition of nickel.* Journal of materials research, 1995. **10**(11): p. 2697-2699.

88. Jung, S., et al., *Electrodeposition of Cu into a Highly Porous Ni/ YSZ Cermet.* Journal of the Electrochemical Society, 2006. **153**(8): p. A1539-A1543.

89. Langlois, S. and F. Coeuret, *Flow-through and flow-by porous electrodes of nickel foam. I. Material characterization.* Journal of applied electrochemistry, 1989. **19**(1): p. 43-50.

90. Gardam, G., *The evaluation of throwing power in electrodeposition.* Trans. Faraday Soc., 1938. **34**: p. 698-711.

91. Bernards, R.F., G. Fischer, and W. Sonnenberg, *Electroplating composition and process*. 1991, Google Patents.

92. Burns, R. and E. Orrell, *A thermal analytical study of phenol formaldehyde resins.* Journal of Materials Science, 1967. **2**(1): p. 72-77.

93. Alayavalli, K.C., *Design, fabrication and testing of graphite bipolar plates for direct methanol fuel cells by indirect laser sintering.* 2011.

94. Ramachandran, V.S. and J.J. Beaudoin, *Handbook of analytical techniques in concrete science and technology: principles, techniques and applications*. 2000: Elsevier.

95. Smits, F., *Measurement of Sheet Resistivities with the Four-Point Probe.* Bell System Technical Journal, 1958. **37**(3): p. 711-718.

96. Kozbial, A., et al., *Understanding the intrinsic water wettability of graphite.* Carbon, 2014. **74**: p. 218-225.

97. Cassie, A. and S. Baxter, *Wettability of porous surfaces.* Transactions of the Faraday Society, 1944. **40**: p. 546-551.

98. Vittal, R., H. Gomathi, and K.-J. Kim, *Beneficial role of surfactants in electrochemistry and in the modification of electrodes.* Advances in colloid and interface science, 2006. **119**(1): p. 55-68.

99. Patankar, N.A., *On the modeling of hydrophobic contact angles on rough surfaces.* Langmuir, 2003. **19**(4): p. 1249-1253.

100. Milliken, W.J., et al., *The viscosity-volume fraction relation for suspensions of rod-like particles by falling-ball rheometry.* Journal of Fluid Mechanics, 1989. **202**: p. 217-232.

101. Jarjoura, G. and G. Kipouros, *Effect of nickel on copper anode passivation in a copper sulfate solution by electrochemical impedance spectroscopy.* Journal of applied electrochemistry, 2006. **36**(6): p. 691-701.

102. Plavšić, M., D. Krznarić, and B. Ćosović, *The electrochemical processes of copper in the presence of triton X-100.* Electroanalysis, 1994. **6**(5-6): p. 469-474.

103. Nikolić, N., et al., *Formation of dish-like holes and a channel structure in electrodeposition of copper under hydrogen co-deposition.* Electrochimica Acta, 2007. **52**(28): p. 8096-8104.

104. Alberti, G., R. Narducci, and M. Sganappa, *Effects of hydrothermal/thermal treatments on the water-uptake of Nafion membranes and relations with changes of conformation, counter-elastic force and tensile modulus of the matrix.* Journal of Power Sources, 2008. **178**(2): p. 575-583.

105. Okada, T., et al., *Ion and water transport characteristics of Nafion membranes as electrolytes.* Electrochimica Acta, 1998. **43**(24): p. 3741-3747.

106. Sing, D.C. and J.P. Meyers, *Direct Measurement of Vanadium Crossover in an Operating Vanadium Redox Flow Battery.* ECS Transactions, 2013. **50**(45): p. 61-72.

107. Parker, V.D., *Energetics of electrode reactions. II. The relationship between redox potentials, ionization potentials, electron affinities, and solvation energies of aromatic hydrocarbons.* Journal of the American Chemical Society, 1976. **98**(1): p. 98-103.

108. O'neill, M., *Measurement of Specific Heat Functions by Differential Scanning Calorimetry.* Analytical chemistry, 1966. **38**(10): p. 1331-1336.

109. Weisstein, E.W., *CRC concise encyclopedia of mathematics*. 2002: CRC press.

110. Chatterjee, A., et al., *An experimental design approach to selective laser sintering of low carbon steel.* Journal of Materials Processing Technology, 2003. **136**(1): p. 151-157.

111. Chen, W.-C., et al., *Identification of inductive behavior for polyaniline via electrochemical impedance spectroscopy.* Electrochimica acta, 2002. **47**(8): p. 1305-1315.

112. Nishi, Y. and R. Doering, *Handbook of semiconductor manufacturing technology*. 2000: CRC Press.

113. Powell, R.W.H.C.Y.L.P.E., *Thermal Conductivity of Selected Materials*, in *NSRDS-NBS 8*. 1966.

114. Bhatia, G., et al., *Conversion of phenol formaldehyde resin to glass-like carbon.* Journal of materials science, 1984. **19**(3): p. 1022-1028.

115. Simchi, A. and H. Pohl, *Effects of laser sintering processing parameters on the microstructure and densification of iron powder.* Materials Science and Engineering: A, 2003. **359**(1): p. 119-128.

116. Nakamizo, M., R. Kammereck, and P.L. Walker, *Laser Raman studies on carbons.* Carbon, 1974. **12**(3): p. 259-267.

117. Price, D.C. and W.G. Davenport, *Densities, electrical conductivities and viscosities of CuSO4/H2SO4 solutions in the range of modern electrorefining and electrowinning electrolytes.* Metallurgical Transactions B, 1980. **11**(1): p. 159-163.

118. Jiang, J. and S.I. Sandler, *A new model for the viscosity of electrolyte solutions.* Industrial & engineering chemistry research, 2003. **42**(25): p. 6267-6272.

119. Kaminsky, M., *Ion-solvent interaction and the viscosity of strong-electrolyte solutions.* Discuss. Faraday Soc., 1957. **24**: p. 171-179.

120. Impey, R., P. Madden, and I. McDonald, *Hydration and mobility of ions in solution.* The Journal of Physical Chemistry, 1983. **87**(25): p. 5071-5083.

121. Brown, W., et al., *Static and dynamic properties of nonionic amphiphile micelles: Triton X-100 in aqueous solution.* The Journal of Physical Chemistry, 1989. **93**(6): p. 2512-2519.

122. Paradies, H.H., *Shape and size of a nonionic surfactant micelle. Triton X-100 in aqueous solution.* The Journal of Physical Chemistry, 1980. **84**(6): p. 599-607.

123. Robson, R.J. and E.A. Dennis, *The size, shape, and hydration of nonionic surfactant micelles. Triton X-100.* The Journal of Physical Chemistry, 1977. **81**(11): p. 1075-1078.

124. Kushner, L.M. and W.D. Hubbard, *Viscometric and turbidimetric measurements of dilute aqueous solutions of a non-ionic detergent.* The Journal of Physical Chemistry, 1954. **58**(12): p. 1163-1167.

125. Li, W. and T. Gu, *Equilibrium contact angles as a function of the concentration of nonionic surfactants on quartz plate.* Colloid and Polymer Science, 1985. **263**(12): p. 1041-1043.

126. Fowkes, F.M., *Role of surface active agents in wetting.* The Journal of Physical Chemistry, 1953. **57**(1): p. 98-103.

127. Boncel, S., K.Z. Walczak, and K.K. Koziol, *Dynamics of capillary infiltration of liquids into a highly aligned multi-walled carbon nanotube film.* Beilstein journal of nanotechnology, 2011. **2**(1): p. 311-317.

128. Kamelin, V., et al., *Optimization of metal deposition on a support with polyurethane foam structure by a combined technique.* Russian journal of applied chemistry, 1998. **71**(2): p. 257-261.

129. Hinatsu, J.T. and F.R. Foulkes, *Diffusion Coefficients for Copper (II) in Aqueous Cupric Sulfate-Sulfuric Acid Solutions.* Journal of The Electrochemical Society, 1989. **136**(1): p. 125-132.

130. Quickenden, T. and X. Jiang, *The diffusion coefficient of copper sulphate in aqueous solution.* Electrochimica acta, 1984. **29**(6): p. 693-700.

131. Mulligan, C.N., *Environmental applications for biosurfactants.* Environmental pollution, 2005. **133**(2): p. 183-198.

132. Bockris, J.M. and M. Enyo, *Mechanism of electrodeposition and dissolution processes of copper in aqueous solutions.* Trans. Faraday Soc., 1962. **58**: p. 1187-1202.

133. Brown, O. and H. Thirsk, *The rate-determining step in the electro-deposition of copper on copper from aqueous cupric sulphate solutions.* Electrochimica Acta, 1965. **10**(4): p. 383-393.

134. Mattsson, E. and J.M. Bockris, *Galvanostatic studies of the kinetics of deposition and dissolution in the copper+ copper sulphate system.* Trans. Faraday Soc., 1959. **55**: p. 1586-1601.

135. Hebrant, M., et al., *Kinetics of metal ion complex formation in micellar media. A comparison between normal and polymerized micelles.* Colloid and Polymer Science, 1996. **274**(5): p. 453-460.

136. Mauritz, K.A. and R.B. Moore, *State of understanding of Nafion.* Chemical reviews, 2004. **104**(10): p. 4535-4586.

137. Lawton, J.S., A. Jones, and T. Zawodzinski, *Concentration Dependence of VO2+ Crossover of Nafion for Vanadium Redox Flow Batteries.* Journal of The Electrochemical Society, 2013. **160**(4): p. A697-A702.

138. Rasmussen, A.A., et al., *Microstructure in electrodeposited copper layers; the role of the substrate.* Electrochimica acta, 2001. **47**(1): p. 67-74.

139. Milchev, A. and T. Zapryanova, *Nucleation and growth of copper under combined charge transfer and diffusion limitations: Part I.* Electrochimica acta, 2006. **51**(14): p. 2926-2933.

140. Grujicic, D. and B. Pesic, *Electrodeposition of copper: the nucleation mechanisms.* Electrochimica Acta, 2002. **47**(18): p. 2901-2912.

141. Zhang, Q., et al., *Influence of grain boundary scattering on the electrical properties of platinum nanofilms.* Applied physics letters, 2006. **89**(11): p. 114102.

142. Kittel, C., P. McEuen, and P. McEuen, *Introduction to solid state physics*. Vol. 8. 1976: Wiley New York.